Mechanisms of ammonium-induced depolarization of astrocytes *in situ*

Inaugural-Dissertation

zur Erlangung des Doktorgrades

der Mathematisch-Naturwissenschaftlichen Fakultät

der Heinrich-Heine-Universität Düsseldorf

vorgelegt von

Jonathan Stephan

aus Lüdenscheid

Düsseldorf, März 2011

Aus dem Institut für Neurobiologie

der Heinrich-Heine Universität Düsseldorf

Gedruckt mit der Genehmigung der

Mathematisch-Naturwissenschaftlichen Fakultät der

Heinrich-Heine-Universität Düsseldorf

Referentin: Prof. Dr. Christine R. Rose

Koreferent: Prof. Dr. Dieter Willbold

Tag der mündlichen Prüfung: 14.04.2011

Introductory Remarks

Parts of this doctoral thesis contains results from experiments carried out with ion-sensitive microelectrodes for measuring the extracellular potassium concentration in brain tissue slices and resembles content of the following diploma theses:

1.: Haack, Nicole; February, 2010; “Influence of Ammonium on the Extracellular Potassium Homeostasis in the Hippocampus”.

2.: Koch, Daniel; February, 2011: “Mechanisms of Ammonia-induced Extracellular Potassium Changes in the Hippocampus of Mouse”.

Abstract

Hepatic encephalopathy (HE) is a serious neurological disorder, which is caused by acute or chronic liver failure. It is attributed to an increase of extracellular ammonium (NH_4^+) that causes a disturbance of ion distribution in both, neurons and astrocytes, as indicated by alterations in intracellular sodium concentration and pH (Kelly and Rose, 2010). Here, the role of astrocytes in mediating the effect of NH_4^+ on the extracellular potassium concentration ($[K^+]_o$) and the NH_4^+-induced changes of the electrophysiological properties of astrocytes in the CA1 region of acute mouse hippocampal slices was analyzed. Astrocytes were identified by labeling with Sulforhodamine 101 (SR101) and based on their electrophysiological properties.

Application of NH_4^+ caused a transient increase in baseline $[K^+]_o$ as determined by K^+-sensitive microelectrodes. $[K^+]_o$ then slowly declined to the baseline. After removal of NH_4^+, a temporary reduction of $[K^+]_o$ occurred. Whole-cell patch-clamp recordings revealed that astrocytes were reversibly depolarized during application of NH_4^+. Under voltage-clamp mode conditions, NH_4^+ induced an inward current as well as a reduction in the membrane resistance. During development, an increase of the NH_4^+-induced depolarization, current, and $[K^+]_o$ increase was observed. In the presence of Ba^{2+}, both the depolarization and the inward current were dramatically reduced, indicating an involvement of K^+ inward-rectifier (*KIR*) channels in the NH_4^+-induced changes of membrane potential and current. This was confirmed with astrocytes from Kir4.1 -/- mice, which exhibited virtually no NH_4^+-induced depolarization and inward current.

Altogether, our results show that the NH_4^+-induced depolarization of astrocytes as well as the $[K^+]_o$ increase reflect an impairment of K^+ homeostasis. This may cause an increased neuronal excitability and reduced glutamate uptake by astrocytes, which in turn is part of the pathology of HE.

Zusammenfassung

Hepatische Enzephalopathie (HE) ist eine schwerwiegende neurologische Erkrankung, die durch akute oder chronische Leberschädigung verursacht wird. Sie steht mit einer Erhöhung des extrazellulären Ammoniums (NH_4^+) in Verbindung, die sowohl in Neuronen als auch in Astrozyten zu einer Beeinträchtigung der Ionenverteilung, wie der intrazellulären Natrium-Konzentration und des pH-Wertes, führt (Kelly and Rose, 2010). In dieser Arbeit wurde die Rolle der Astrozyten hinsichtlich des Effekts von NH_4^+ auf die extrazelluläre Kalium-Konzentration ($[K^+]_o$) und die NH_4^+-induzierten Veränderungen der elektrophysiologischen Eigenschaften von Astrozyten in der CA1-Region des Hippokampus der Maus untersucht. Astrozyten wurden anhand ihrer Färbung mit Sulforhodamine 101 (SR101) und ihrer elektrophysiologischen Eigenschaften identifiziert.

Die Applikation von 5 mM NH_4^+ verursachte einen Anstieg der $[K^+]_o$, welcher mittels K^+-sensitiver Mikroelektroden gemessen wurde. Danach sank die $[K^+]_o$ wieder langsam auf ihren Ausgangswert. Das Auswaschen des NH_4^+ führte zu einer temporären Abnahme der $[K^+]_o$. Whole-cell patch-clamp-Messungen zeigten, dass Astrozyten während der Applikation von NH_4^+ reversibel depolarisierten. In Voltage-clamp führte NH_4^+ zu einem Einwärtsstrom sowie einer Verringerung des Membranwiderstandes. Während der Entwicklung nahmen die NH_4^+-induzierte Depolarisation, der Einwärtsstrom und die $[K^+]_o$-Erhöhung zu. In der Gegenwart von Ba^{2+} waren sowohl die Depolarisation als auch der Einwärtsstrom stark reduziert, was auf einen Beitrag von einwärtsgleichrichtenden K^+ (*KIR*)-Kanälen an der NH_4^+-induzierten Änderung des Membranpotentials und Membranstroms hindeutet. Dies wurde anhand von Astrozyten aus Kir4.1 -/- Mäusen bestätigt, die annähernd keine NH_4^+-induzierte Depolarisation und keinen Einwärtsstrom aufwiesen.

Zusammengenommen zeigen diese Ergebnisse, dass die NH_4^+-induzierte Depolarisation der Astrozyten als auch der Anstieg der $[K^+]_o$ eine Störung der K^+-Homöostase widerspiegeln. Dies könnte zu einer erhöhten neuronalen Erregbarkeit und einer verringerten Glutamat-Aufnahme durch Astrozyten führen, was wiederum ein Teil der Pathologie von HE ist.

Contents

Abbreviations

A	ampere (SI derived unit for electric current)
ACSF	artificial cerebrospinal fluid
ALF	acute liver failure
AMPA	α-Amino-3-hydroxy-5-methylisoxazole-4-propionic acid (AMPA/kainate receptor agonist)
Alexa	Alexa Fluor dye
(D-L-)AP5	D-L-2-Amino-5-methylisoxazole-4-propionic acid (selective NMDA receptor antagonist)
AGP4	aquaporine 4
(Mg-) ATP	(magnesium) adenosine triphosphate
Ba^{2+}	barium ion (inhibitor of inwardly rectifying potassium channels)
BSA	bovine serum albumine
Bum	bumetanide (inhibitor of sodium-potassium-2 chlorid-cotransporter)
C	coulomb (SI derived unit for electric charge)
°C	degrees centrigrade
CA1; CA3	cornu ammonis area 1; cornu ammonis area 3
Ca^{2+}	calcium ion
$CaCl_2$	calcium chloride
Cl^-	chloride
CLF	chronic liver failure
C_M	membrane capacitance
CNQX	6-Cyano-7-nitroquinoxaline-2,3-dione (competitive AMPA/kainate receptor antagonist)
CNS	central nervous system
CO_2	carbon dioxide
CsA	cyclosporine A
DAPI	4′,6-Diamidin-2-phenylindol
DON	6-diazo-5-oxo-L-norleucine
EAAT	excitatory amino acid transporter
EGFP	enhanced green fluorescent protein

EGTA	ethylene glycol-bis(2-aminoehtylether)-N,N,N',N'-tetraacetic acid (Ca^{2+} chelator)
E_M	membrane potential
E_x	equilibrium potential of 'x'
F	Faraday constant: 96485 C/mol
F	farad (SI derived unit for capacitance)
GD	*gyrus dentatus* (or DG = dentate gyrus)
GFP	green fluorescent protein
GLAST	glutamate-aspartate transporter (human homolog is EAAT1)
Gln	glutamine
GLT-1	glutamate transporter 1 (human homolog is EAAT2)
Glu	glutamate
GFAP	glial fibrillary acidic protein (intermediate filament in a subpopulation of astrocytes)
GS	glutamine synthetase
(Na_3-) GTP	(trisodium) guanosine triphosphate
H^+	hydrogen
HCO_3^-	bicarbonate (/hydrogen carbonate)
HE	hepatic encephalopathy
HEPES	N-(2-Hydroxyethyl)-piperazine-N′-2-ethanesulfonic acid (pH buffer)
Hi	*hilus*
I_{NH4+}	ammonium (NH_4^+)-induced current
J	joule (SI derived unit for energy)
K	kelvin (SI derived unit for absolute temperature)
K^+	potassium ion
K_{Ca}	calcium dependent potassium channel
KCl	potassium chloride
K_{DR}	delayed rectifier potassium channel (belongs to K_V)
K_{IR}	inwardly rectifying potassium channel
Kir4.1	4.1 subunit of inwardly rectifying potassium channel
K-$MeSO_3$	potassium methansulfonate
KO (-/-)	knock out

K_{2P}	2 pore domain potassium channel
K_V	voltage activated potassium channel
M	molar (SI derived unit for concentration)
m	meter (SI derived unit for length)
MSO	methioninesulfoximine
$MgCl_2$	magnesium chloride
mol	mole (SI derived unit for amount of substance)
MPT	mitochondria permeability transition
n	number of independent experiments
Na^+	sodium ion
$NaHCO_3$	sodium hydrogen carbonate
NaH_2PO_4	monosodium phosphate (/sodium dihydrogen phosphate)
NaCl	sodium chloride
Na^+, K^+-ATPase	sodium potassium pump
Na_V	voltage activated sodium channel
NG2	a 'chondriotin sulfate proteoglycan'
NGS	normal goat serum
NH_3/NH_4^+	ammonia/ammonium
NKCC	sodium-potassium-2 chlorid-cotransporter
NMDA-R	N-methyl-D-aspartate (agonist at NMDA-type glutamate receptors)
n.s.	not significant, $p \geq 0.05$
*	significant, $p < 0.05$
**	significant, $p < 0.01$
***	significant, $p < 0.001$
Ω	ohm (SI derived unit for electrical resistance)
p	probability value
PAG	phosphate-activated glutaminase
Pi	free phosphate
PBS	phosphate-buffered saline
PFA	paraformaldehyde
PO_4^{3-}	phosphate
P'x'	postnatal day 'x'
(n/)PG	(non-) passive glial cell

R	gas constant: 8,314472 $J/mol*K$
R_{In}	input resistance
R_M	membrane resistance
ROS	reactive oxygen species
R_S	series resistance
RT	room temperature (19 - 22 °C)
s	second (SI derived Unit for time)
s	slope
S	(para-, pre-) *subiculum*
SBFI (-AM)	sodium-binding benzofuran isophthalate (acetoximethylesther)
S.D.	standard deviation
S.E.M.	standard error of the mean
SG	*stratum granulosum*
SL	*stratum lucidum*
SLM	*stratum lacunosum moleculare*
SO	*stratum oriens*
SP	*stratum pyramidale*
SR	*stratum radiatum*
SR101	sulforhodamine 101 (fluorescent dye)
T	absolute temperature in K
τ	tau - time constant
TEA	tetraethylammonium (inhibitor of voltage activated potassium channels)
TTX	tetrodotoxin (inhibitor of voltage-activated sodium channels)
V	volt (SI derived unit for electromotive force)
WT (+/+; +/-)	wild type (phenotypic)
x_n	mean
$[x^z]_{i/a}$	intra-/extracellular ion concentration of ‘x’
z	valence

1 Introduction

1.1 Astrocytes and their neighbours

The brain together with the spinal cord, is part of the central nervous system (CNS). It is structured in different functional areas e.g. such as cortex, hippocampus and cerebellum that again are comprised of several different cell types, which can be generally divided into neurons and glia (also neuroglia). In 1856, Rudolf Virchow first described neuroglia being responsible for CNS cohesion, as the term glia, derived from the Greek word for glue, already suggests. With 100 billion (10^{11}) cells, these glia resemble the predominant cells, as they 10-fold overtop the number of neurons. Glia can be subdivided in macro- and microglia. Like neurons, macroglia originate from the neuroectodem and can be subdivided again into astrocytes and oligodendrocytes.

The term astrocyte was introduced around 1913 and was used by Santiago Ramón y Cajal to describe fibrous and protoplasmic shaped glia (Kimelberg, 2004). These cells are comprised of several functions (see next chapter). The main functions of oligodendrocytes are myelination and maintenance of axonal processes of neurons to enable fast signal propagation in vertebrates by electrical isolation of the fibers (Bunge, 1968; Baumann and Pham-Dinh, 2001). In contrast to macroglia, microglia arise from the mesoderm and reflect the immune system of the CNS, as they are immunocompetent (Dheen ST, 2002; Farber and Kettenmann, 2005) and the immune system of the body is not able to overcome the blood brain barrier.

1.2 One cell type - multiple functions

During the last one hundred years, the view of astrocyte function dramatically changed from being the glue that holds together CNS tissue to communication elements (Volterra and Meldolesi, 2005). Among others, astrocytes have important functions providing metabolites to neurons, as they bridge the gap between neurons and blood vessels by contacting both with their endfeet. Upon neuronal activity, astrocytes regulate blood vessels diameter to increase cerebral blood flow (vasomodulation) and ensure an on demand delivery of metabolites to neurons (Zonta et al., 2003; Mulligan and MacVicar, 2004; Metea and Newman, 2006; Takano et al., 2006).

Astrocyte endfeet are not equal, as they are specialized depending on the structure they cover. At the side of blood capillaries, astrocytic endfeet together with endothelial cells form the blood-brain-barrier including a selectivity filter that allows the transfer of nutrients e.g. glucose and amino acids and a repulsion of bacteria, viruses and most cytotoxic substances (Hawkins et al., 2006). Moreover, blood-brain-barrier properties of the endothelial cells are induced by astrocytes (Pekny et al., 1998; Kuchler-Bopp et al., 1999). At the neuronal side, astrocytes control synapse formation (Ullian et al., 2004). Afterwards, synapses are ensheathed by astrocytic endfeet that maintain and modulate synaptic communication between neurons (Kang et al., 1998; Araque et al., 1999; Haydon, 2001; Newman and Volterra, 2004; Haydon and Carmignoto, 2006; Perea and Araque, 2010). Modulation of synaptic transmission is provided by the degree of astrocytic neurotransmitter uptake and the release of gliotransmitters (Danbolt, 2001; Halassa et al., 2009; Eulenburg and Gomeza, 2010).

Another important feature of astrocytes for normal brain function is the uptake and redistribution of locally released K^+ by a process called 'spatial buffering' or 'K^+ siphoning' (Kofuji and Newman, 2004). Kir channels are the predominant channel type in astrocytes (Seifert et al., 2009). Beside the Na^+, K^+-ATPase, those channels are mainly responsible for the K^+ uptake, as their absence causes an impairment of K^+ buffering (Neusch et al., 2006; Seifert et al., 2006; Kucheryavykh et al., 2007). Next K^+ is redistributed within the astrocytic network (Holthoff and Witte, 2000; Wallraff et al., 2006) and is released at sides of lower extracellular potassium concentration.

1.3 Identification of astrocytes

Working on astrocytes requires a reliable identification. There are several techniques available to sufficiently identify astrocytes, although each of them is comprised of different advantages and disadvantages. Those techniques include 1) SR101-labeling, 2) electrophysiology, 3) immunohistochemistry or 4) transgenic approaches.

1.3.1 SR101-labeling

The *in vivo* suitable red fluorescent dye SR101 selectively labels mature and immature classical defined astrocytes in both, cortex and hippocampus (Fig. 1) (Nimmerjahn et al., 2004; Kafitz et al., 2008). During the first two weeks of postnatal development, the amount of SR101-labeled cells in the *stratum radiatum* increases as visualized by counter labeling with SBFI-AM, which is supposed not to increase in the amount and

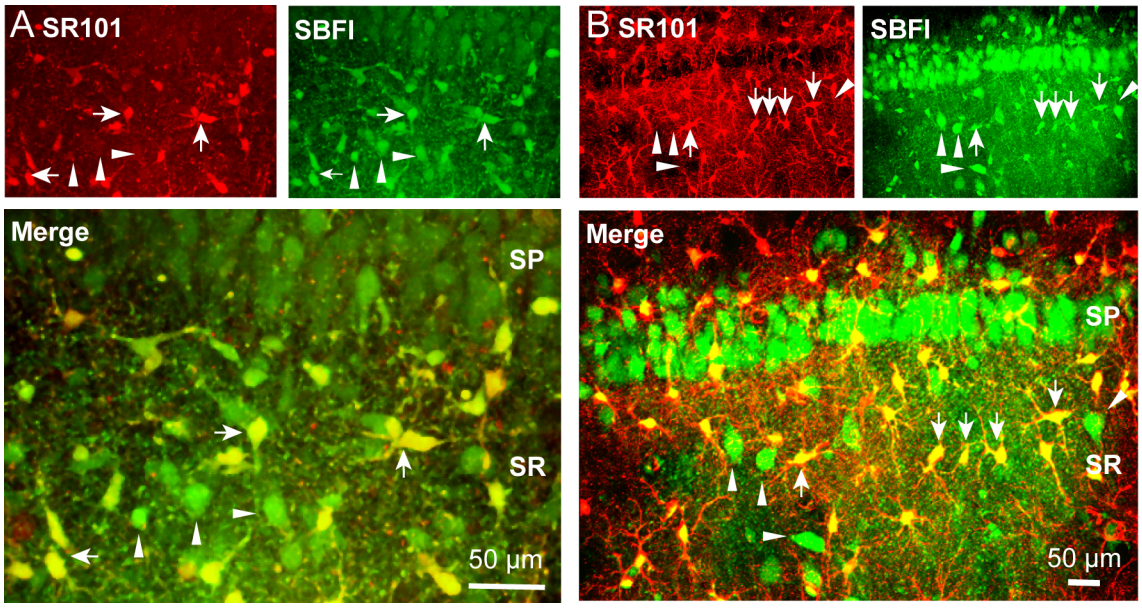

Fig. 1: Robust labeling pattern of SR101 vs. SBFI-AM in the hippocampal CA1 region during early postnatal development.
Fluorescence images of acute slices from P3 (A) and P15 (B) rats double-stained with SR101 (upper left panels) and SBFI-AM (upper right panels), taken at a custom build two-photon laser-scanning microscope. The lower, enlarged panels show the merged fluorescence images. SP: *stratum pyramidale*; SR: *stratum radiatum*. Arrows mark double-labeled cells located in the *stratum radiatum*; arrowheads point out cells which are exclusively stained by SBFI. Note that putative pyramidal neurons in the *stratum pyramidale* are also stained with SBFI, but not with SR101. (Kafitz, Meier, Stephan, Rose 2008)

specificity (Fig. 2). Neurons in the *stratum pyramidale* remain unlabeled. SR101-negative cells in the *stratum radiatum* show properties of NG2 or ORG (outward rectifying glia) called cells, that have a depolarized membrane potential compared to astrocytes, a high membrane resistance, and display currents through voltage activated sodium and potassium channels (Kafitz et al., 2008; Honsek et al., 2010).

The reliable identification of astrocytes *a priori* makes a confirmation via electrophysiological measurements or postrecording immunohistochemistry unnecessary. This is a big advantage for both, imaging experiments using ion-sensitive dyes such as Fura-2 or SBFI as well as patch-clamp experiments for unerringly targeting astrocytes. It is important to note that the electrophysiological properties of such labeled astrocytes do not differ from those reported earlier (Steinhauser et al., 1992; Wallraff et al., 2004; Zhou et al., 2006). It must be considered that SR101 is not fixable. Thus, another dye must be added to the intracellular solution in patch-clamp experiments (Fig. 5) or nano beats have to be placed to be able to identify the measured cell after fixation.

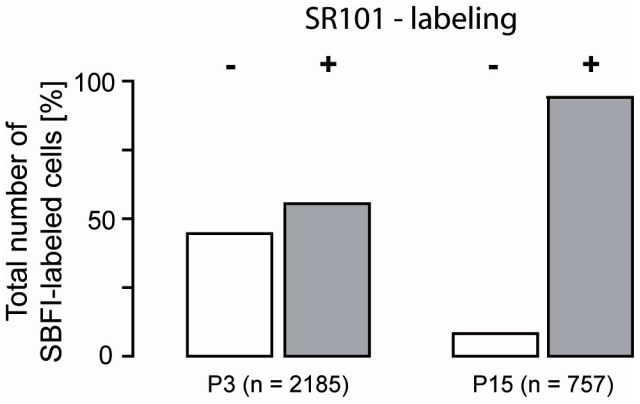

Fig. 2: Upregulation of SR101-positive cells compared to all SBFI-labeled cells. Quantification of the percentage of SR101-negative (white bars) and SR101-positive (grey bars) cells on the total number of small-sized SBFI-labeled cells located in the *stratum radiatum* in P3 (n = 22 slices; 2185 cells) and P15 rats (n = 11 slices; 757 cells). (Kafitz, Meier, Stephan, Rose 2008)

1.3.2 Electrophysiological properties of astrocytes

As mentioned above, astrocytes show distinct electrophysiological properties allowing to distinguish them from all surrounding cell types. Compared to neurons and NG2 cells, astrocytes display a low membrane potential and resistance and they are incapable to generate action potentials. Moreover, they undergo considerable changes in channel complement and passive membrane properties during early postnatal development

(Kressin et al., 1995; Bordey and Sontheimer, 1997; Zhou et al., 2006; Kafitz et al., 2008). During the first postnatal week, most astrocytes display currents through voltage-activated potassium channels resulting in a non-linear IV-relationship and can be termed 'non-passive' (Fig. 3*A*, *B*). At the beginning of the third postnatal week, astrocytes predominantly lack voltage-activated currents and show only ohm-like currents. Because of the resulting linear IV-relationship, these astrocytes can be termed 'passive' (Fig. 3*C*). During this maturation process, non-passive astrocytes become passive (Fig. 3D), while their membrane resistance decreases (Zhou et al., 2006; Kafitz et al., 2008).

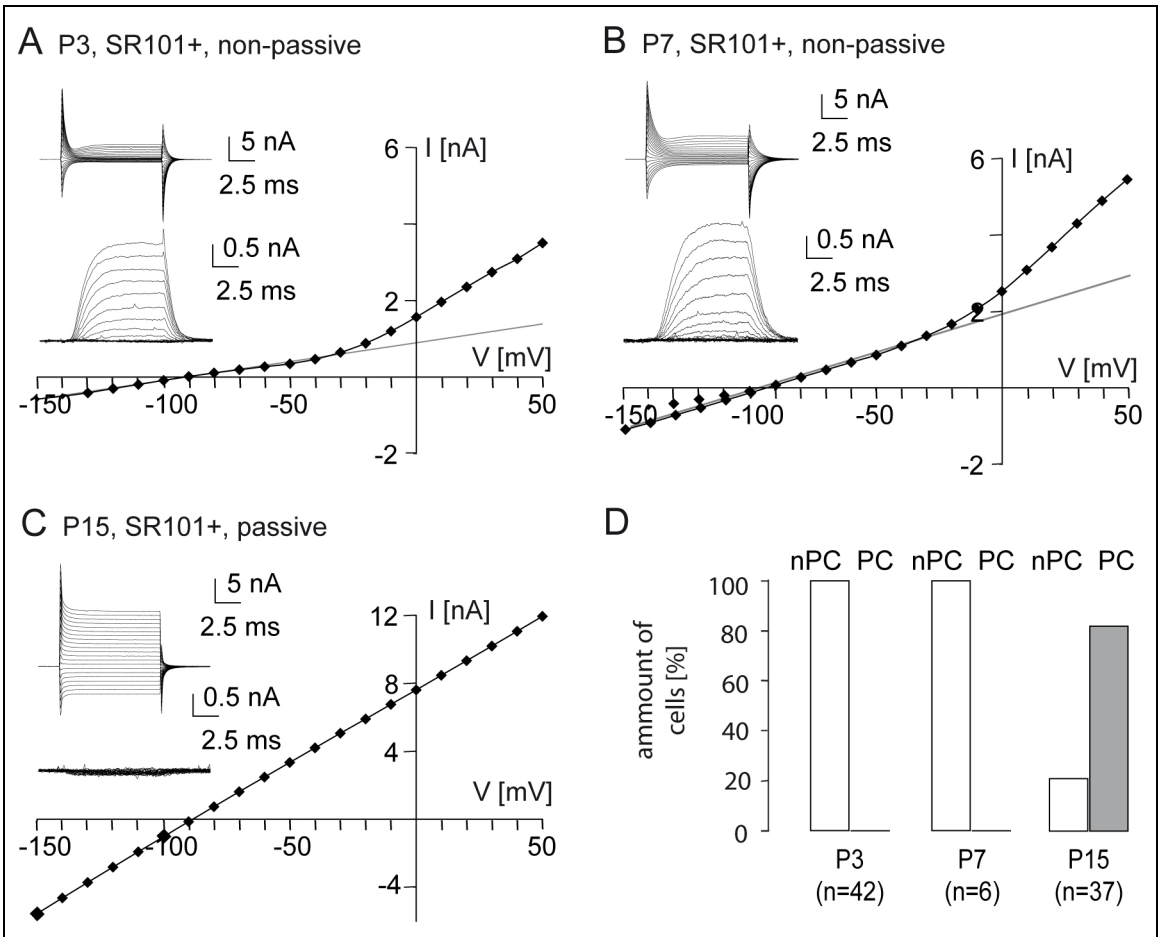

Fig. 3: IV-relationship of SR101-positive cells of P3 (A), P7 (B) and P15 (C) rats.
Cells were held at -85 mV and subjected to 10 ms voltage steps ranging from -150 to +50 mV at 10 mV increments. The insets on the left side show the resulting membrane current before (top) and after leak subtraction (bottom). The IV-plots depict the amplitudes of the resulting currents at 8 - 10 ms after the start of the voltage step of the same cell, the grey lines show the linear regression curves. Astrocytes at P3 (A) and P7 (B) exclusively showed non-linear IV-relationships. At P15 (C), mostly linear IV-curves were found. (D) Quantification of the amount of cells with non-linear (non-passive cells, nPC, white bars) or linear (passive cells, PC, grey bars) IV-curves on the total number of SR101-positive cells at P3, P7 and P15. (Kafitz, Meier, Stephan, Rose 2008)

According to this decrease of astrocytic membrane resistance, an issue regarding proper patch-clamp conditions arises. In astrocytes older than two weeks, the membrane resistance is in general lower than the achievable series resistance. It must be considered that clamping of astrocytes exhibiting a low membrane resistance might be insufficient (Zhou et al., 2009).

The low membrane resistance is based on two principles: At first, the high potassium conductance (Walz et al., 1984) that is enhanced during the early postnatal development, as the expression of potassium channels increases with age (Sontheimer and Waxman, 1993; Ransom and Sontheimer, 1995; Seifert et al., 2009). Second, astrocytes are extensively coupled via gap junctions forming a syncytium in which ions, nutrients, and currents are distributed (Fig. 4) (Wallraff et al., 2006; Giaume and Theis,

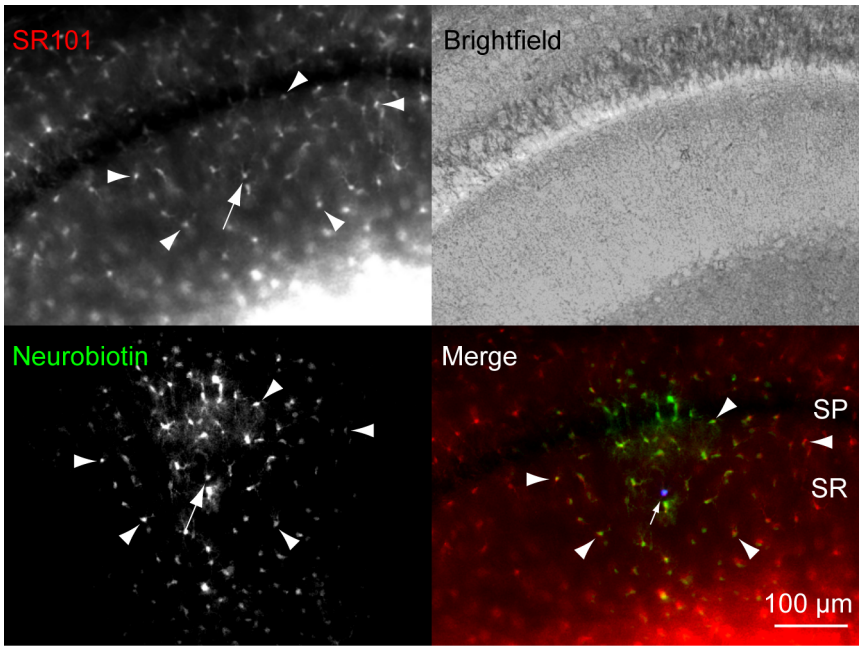

Fig. 4: Gap junctional coupling of astrocytes.
Based on the SR101-labeling, one astrocyte in the CA1 region of the *stratum radiatum* from a mouse at P16 was chosen (arrow) and characterized electrophysiologically (upper left). The intracellular solution contained the gap junction impermeable Alexa 594 to identify the patched cell after fixation and the gap junction permeable Neurobiotin (detected with Avidin Alexa 488) to visualize coupled cells (lower left). Superimposing the SR101-labeling pattern, Alexa 594 (red fluorescent dye; in the image converted into blue), and Avidin Alexa 488 revealed that all coupled cells were SR101 positive (lower right). The astrocytic network was not restricted to the *stratum radiatum*, but is rather capable of crossing laminar borders. Here, Neurobiotin reached cells in the *strata oriens* (in pictures above SP) and *lacunosum moleculare* (in pictures below SR). SP: *stratum pyramidale*; SR: *stratum radiatum*.

2010; Xu et al., 2010). While the astrocytic network in the hippocampus has no borders and crosses all lamina (Konietzko and Muller, 1994), in layer IV of the barrel cortex it is restricted to its barrel (Houades et al., 2008). During the early postnatal development the degree of coupling increases (Schools et al., 2006). To overcome the issue of the low input resistance and to gain voltage-clamp control, the astrocytic membrane resistance can be raised by decreasing leak conductances using potassium channel blockers and with pharmacological uncoupling agents or isolation of astrocytes (Anderson et al., 1995; Wallraff et al., 2006; Seifert et al., 2009).

Altogether, the electrophysiological identification of astrocytes is a fast and explicit method, which is straight forward in patch-clamp recordings, but can be difficult in combination with imaging experiments, because of the potential loss of the cell soma during withdrawel of the patch pipette.

1.3.3 Immunohistochemical properties of astrocytes

Beside the two methods described above, which identify astrocytes prior to actual experiments, astrocytic identity can be determined in fixed tissue by immunohistochemistry. In particular, the glial fibrillary acidic protein (GFAP) is a widely used marker for astrocytes. It is the predominant intermediate filament in mature astrocytes and belongs to the cytoskeletal protein family. GFAP is thought to be important in modulating astrocyte motility and shape by providing structural stability to astrocytic processes (Eng et al., 2000), although KO mice lacking GFAP develop normally without showing any anatomical, histological, or behavioral abnormalities (Pekny et al., 1995). Although GFAP is a suitable marker for astrocytes, it must be considered, that there are few GFAP-negative cells with electrophysiological properties of astrocytes. Therefore, GFAP only labels a subset of astroglial cells (Fig. 5) (Lee et al., 2006; Raponi et al., 2007; Kafitz et al., 2008). The utilization of other astrocyte specific intermediate filaments, like Vimentin or S100β, is even more restricted, as they are developmental dependent expressed in more immature or, respectively, mature astrocytes (Stichel et al., 1991; Raponi et al., 2007).

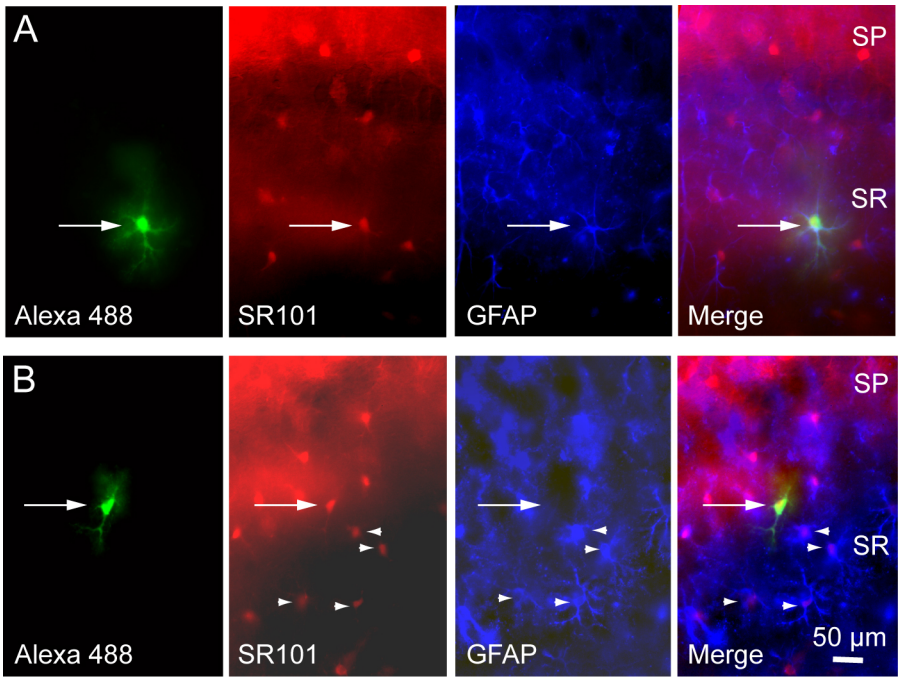

Fig. 5: Immunohistochemical characterization of SR101-positive cells at P15.
(A) From left to right: image of the staining pattern of SR101 in the *stratum radiatum*. Based on this staining, a SR101-positive cell was chosen (arrow) and characterized electrophysiologically while filling the cell with Alexa 488. In the subsequent immunohistochemical analysis, the same cell also showed immunoreactivity for GFAP. The merged picture of all three fluorescence images confirms the identity of the triple-labeled cell. (B) The same experimental design also identified the rare case of a cell, which was SR101-positive, electrophysiologically characterized as glial cell, but showed no immunoreactivity for GFAP (arrow). The arrowheads point to cells, which were double-labeled for SR101 and GFAP. SP: *stratum pyramidale*; SR: *stratum radiatum*. (Kafitz, Meier, Stephan, Rose 2008)

1.3.4 Transgenic mice

Another way to identify astrocytes *a priori* is to utilize transgenic mice, in which a reporter gene coding e.g. for GFP or EGFP is inserted into the genome and coupled to the astrocyte specific GFAP promoter (Zhuo et al., 1997; Nolte et al., 2001). The GFAP-EGFP transgene is not active in all astrocytes and differs between different brain regions. While there is in the cerebellum a complete overlap between EGFP expression and GFAP immunoreactivity, in the hippocampus the amount of cells, which express EGFP, is lower than the amount of GFAP immunopositive cells (Nolte et al., 2001). Furthermore, approximately 50 % of all SR101-labeled cells in the neocortex *in vivo* exhibit GFAP controlled EGFP expression (Nimmerjahn et al., 2004). In summary, in

transgenic mice astrocytes can be identified *a priori*, but it must be considered that these resemble only a part of the entire astrocyte population.

1.4 The hippocampus

In 1911 Santiago Ramón y Cajal showed his drawing of the hippocampus in the book *Histologie de Système Nerveux*. He already speculated about the direction of signal propagation: input to the dendrites and output through the axon. He additionally concluded that a single hippocampal neuron could influence a large number of target cells and areas (Andersen et al., 2007). The hippocampus is embedded in the medial temporal lobe of each hemisphere and shows a distinct circuitry (Fig. 6) that was already suggested by Cajal. The hippocampal formation comprises four regions: 1) hippocampus proper (subdivided in CA3 to CA1), 2) *gyrus dentatus*, 3) *subiculum*, and 4) entorhinal cortex.

The different cell types, mainly neurons and astrocytes, are organized in distinct layers. The neuronal cell bodies are located in the *strata pyramidale* and *granulosum* with their dendrites extending into neighboring lamia, while astrocytes are located in all layers beside those two. Neurons in the *gyrus dentatus* (granule cells) and in the *stratum pyrmidale* (pyramidal cells) receive excitatory input via the perforant path from the entorhinal cortex. Granule cells project their axons (mossy fibers) on CA3 pyramidal cells, which in turn send their axons (Schaffer collaterals) to CA1 pyramidal cells. Those project back onto neurons in the entorhinal cortex.

Early implications of hippocampal function were gained on the case of the patient H.M. in the mid fifties. H.M. suffered from massive epileptic seizures and at final consequence, the medial portion of his temporal lobe was resected bilaterally causing anterograde amnesia. Post surgery examination of H.M. showed that his short term memory of position, people or profiles (declarative/episodic memory) was not impaired. It became immediately clear that the hippocampus is not the place of memory storage but is necessary for memory consolidation. In contrast, learning of movement (non-declarative/implicit memory) was not affected. It became clear that the hippocampus is a well suitable structure to study, because of its function in memory and the conserved and well-arranged synaptic circuits providing research on basic cellular physiology and synaptic plasticity.

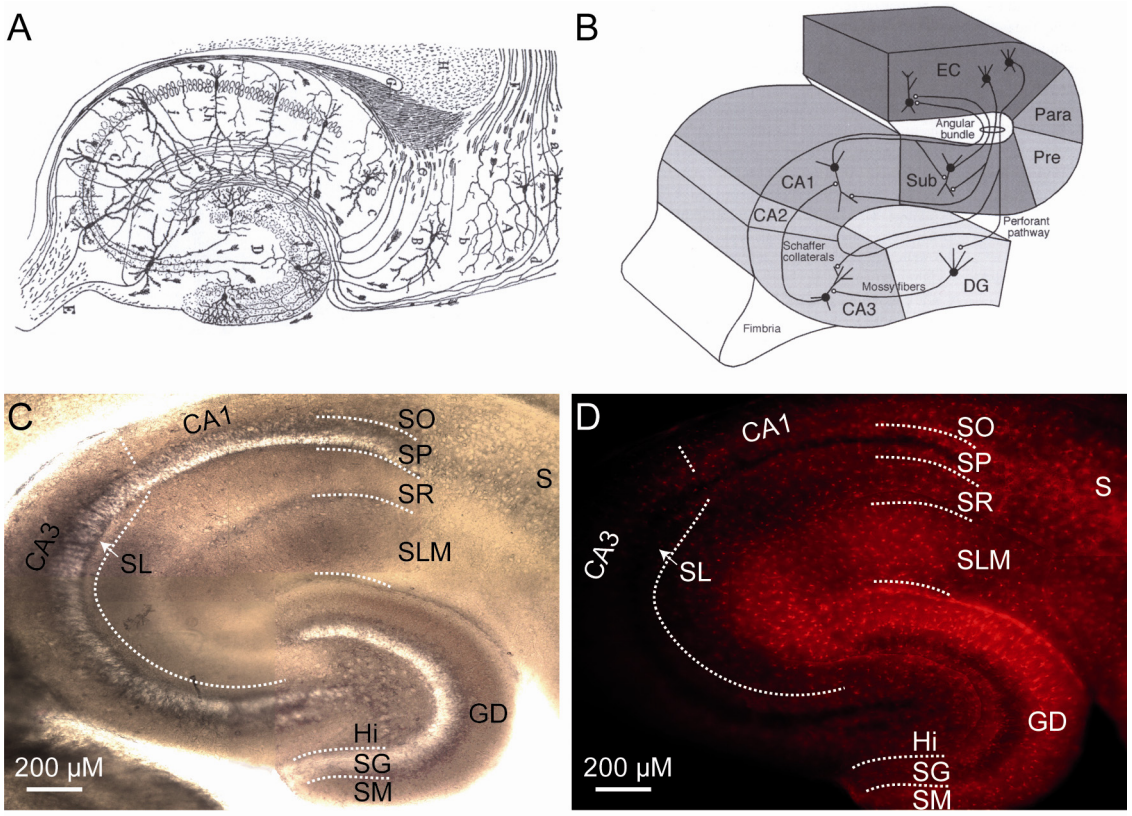

Fig. 6: The hippocampal formation.
(A) Cajals drawing of the hippocampus from his 1911 book *Histologie de Système Nerveux*. (B) Scheme of the hippocampal formation and its connectivity. (A+B from Andersen et al. 2007) (C) Reconstruction from 4 single VIS-DIC images of the mouse hippocampus at P20. (For abbreviations see page 3) (D) Reconstruction from 4 single fluorescence images of the same area as in C. The SR101-labeling pattern shows a similar lamination as seen with VIS-DIC. All lamina except for the pyramidal cell bodies containing *stratum pyramidale* displayed red fluorescent SR101-labeled astrocytes. It must be considered that the fluorescence intensity differs between the several cell layers.

1.5 Hepatic encephalopathy

1.5.1 The clinical perspective - acute and chronic liver failure

Hepatic encephalopathy (HE) is a serious neurological disorder caused by acute (ALF) or chronic (CLF) liver failure. The only way of full healing consists in a liver transplantation. ALF is accompanied by an [NH_4^+] increase in blood from 0.05 - 0.1 mM to 0.3 - 0.5 mM (Clemmesen et al., 1999). NH_4^+ is capable to cross the blood-brain-barrier (Ott and Larsen, 2004) and can rise to 1 - 5 mM in the brain (Swain et al., 1992a; Swain et al., 1992b). Patients show a rapid progression of symptoms - within hours or days - that can be subdivided into four grades (West Haven Criteria) (Ferenci et al., 2002):

- Grade I: Patients exhibit mild confusion and alteration in their sleep-wake rhythm.
- Grade II: Patients show psychomotoric deceleration and minimal disorientation for time and place.
- Grade III: Patients display strong confusion as they become spacy and loose more and more of their intellectual skills.
- Grade IV: Patients become unconscious and comatose.

Shortly after achieving grade IV, most patients die from increased intracranial pressure (Capocaccia and Angelico, 1991; Schiodt et al., 1999) caused by astrocyte swelling (Ganz et al., 1989; Blei et al., 1994).

The other form of HE, CLF, shows a slow progression. The [NH_4^+] in blood rises to 0.1 - 0.2 mM. Symptoms mainly attract attention after ingestion of NH_4^+ in form of amino acids or proteins in the nutrition. Hyperammonemic syndromes are generally treated with a reduction of protein intake. Ornithine administration is effectively used to lower ammonium levels by activating the urea cycle (see chapter 1.5.3) (Felipo and Butterworth, 2002).

1.5.2 NH_4^+ administration: A model for hepatic encephalopathy

To study the pathogenesis of HE, several different animal models are available, in which the liver is mechanically or chemically destroyed. These models show features of HE, for example brain edema and increased brain ammonia and glutamine content (Butterworth et al., 2009). In young primates ammonium infusion caused an increase of the blood ammonium concentration and a concomitant change in mental state, which can be correlated with symptoms observed in HE patients (Voorhies et al., 1983).

Beside this, acute brain tissue slices are widely used to directly investigate the effect of hyperammonemia on the cellular level. Those slices provide the advantage of a well-preserved cytoarchitecture combined with an easy handling. It must be considered that at least in CLF further toxins than ammonium accumulate (Felipo and Butterworth, 2002). Nonetheless, ammonium plays a key role in the pathogenesis of HE. It has been shown to induce different features of HE as brain edema, swelling of astrocytes, an overall decreased glutamate and increased glutamine content, and an increase of the basal extracellular glutamate concentration (Ganz et al., 1989; Swain et al., 1992a; Kosenko et al., 1993; Blei et al., 1994; de Knegt et al., 1994).

1.5.3 The origin of NH_4^+ accumulation

The origin of the NH_4^+ accumulation is related to deficits in the urea cycle. In general, the degradation of amino acids leads to a release of NH_4^+. Some of it is used for the synthesis of new nitrogen containing molecules. In a healthy organism the overage is then detoxified in the liver via the urea cycle (Fig. 7). Initially, the α-residue of most amino acids is temporarily transferred during transamination to α-ketoglutarate forming glutamate before NH_4^+ is separated by glutamate dehydrogenase (oxidative deamination). In mitochondria of hepatocytes, carbamoylphosphate is synthesized from NH_4^+, HCO_3^- and phosphate (P_i). Under

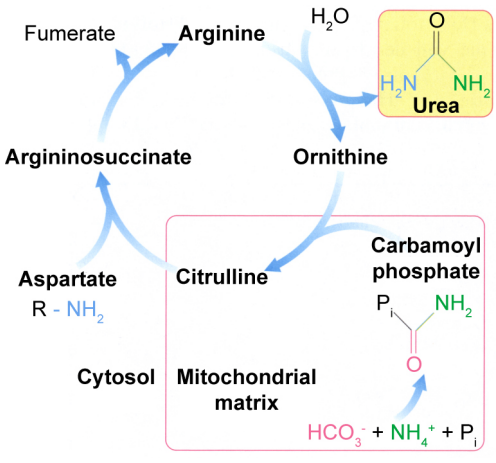

Fig. 7: The urea cycle.
Modified from Berg et al. 2002

removal of the phosphate and incorporation of ornithine, citrulline is build. After conversion to argininosuccinate and arginine in the cytosol, ornithine is retrieved under separation of urea.

The loss of function of one at the urea cycle participating enzymes causes an interruption of this cycle and finally results in an increased NH_4^+ content in the blood (hyperammonemia) and in CNS tissue. Untreated newborns suffer from seizures or coma. If they survive, most of them display mental retardation or cerebral paralysis. In adulthood, liver damage and secondly hyperammonemia are often caused by durable high levels of alcohol, viral infections (e.g. by hepatitis C) or autoimmune diseases.

1.5.4 NH_4^+ impairs ion homeostasis

As initially mentioned, hepatic encephalopathy (HE) is a serious neurological disorder caused by acute or chronic liver failure. A major factor for the pathology of HE is the increased ammonium (NH_4^+) concentration in the brain (Swain et al., 1992a; Swain et al., 1992b) that is accompanied by altered glutamate and energy metabolism (Rama Rao and Norenberg, 2001; Rose, 2002) as well as astrocytic swelling (Norenberg et al., 2007). At physiological conditions the balance between NH_3 and NH_4^+ is with 98 % on the side of NH_4^+ (Felipo and Butterworth, 2002). In contrast to the uncharged ammonia, ammonium itself is incapable to cross plasmamembranes. However, as the ion radius and charge of NH_4^+ correspond to those of K^+, it can effectively substitute for K^+ at ion channels (Hille, 1973; Latorre and Miller, 1983; Allert et al., 1998; Nagaraja and Brookes, 1998) and transporters (Yan et al., 2001; Bergeron et al., 2003; Titz et al., 2006; Kelly et al., 2009) although their affinity for NH_4^+ in comparison to K^+ is lower (Marcaggi and Coles, 2001).

In the central nervous system, NH_4^+ causes an impairment of ion distribution. Recent studies showed that the intracellular concentrations of Na^+ and H^+ are altered during hyperammonemia. In hippocampal slices, NH_4^+ causes an acidification in neurons that is mediated by the Na^+, K^+-ATPase. Astrocytes simultaneously exhibit an acidification mediated by the Na^+, K^+-ATPase and the Na^+, K^+, Cl^- cotransporter (NKCC) as well as a concomitant $[Na^+]_i$ increase that is exclusively mediated by NKCC (Kelly and Rose, 2010). As shown in primary astrocytic cultures, this $[Na^+]_i$ increase leads to a reduced glutamate uptake (Kelly et al., 2009). Furthermore, measurements of

K^+ in the extracellular space revealed a $[K^+]_o$ increase during NH_4^+ application (Alger and Nicoll, 1983). It is thought that the $[K^+]_o$ increase is due to a loss of cellular K^+, as the tissue content of K^+ is decreased during hyperammonemia (Benjamin et al., 1978).

Upon the application of NH_4^+, several different cell types exhibit a depolarization. In glial cells of bee retina, a depolarizing effect of NH_4^+ was observed that is insensitive to bumetanide and Ba^{2+} (Marcaggi et al., 2004). In the presence of NH_4^+, pyramidal neurons in the hippocampus depolarized in a concentration-dependent manner (Alger and Nicoll, 1983; Kelly and Church, 2005). The latter authors assumed an entry of NH_4^+ into the cell via K^+ channels being responsible for the NH_4^+-induced depolarization. In cultures of cortical astrocytes, it was shown that NH_4^+ causes a depolarization involving Ba^{2+}-sensitive K^+ inward rectifier (*KIR*) channels (Allert et al., 1998).

1.5.5 Disturbed distribution of glutamate and glutamine

Beside the impairment of intra- and extracellular ion homeostasis and an overall disturbance of membrane potential, the balance of glutamate and glutamine in the CNS is affected. The glutamate-glutamine-cycle is an important process, by which released glutamate is retrieved to the presynaptic terminals of neurons to refill the glutamate pool (Fig. 8) (Danbolt, 2001). It is placed in two compartiments, the presynaptic terminal and the astrocyte, which covers the synapse. Glutamate is released from the presynaptic terminal via exocytosis and is taken up again either by the presynaptic neuron or the astrocyte. The secondary active transport of glutamate is driven by the Na^+ gradient and causes an increase of the intracellular Na^+ concentration. Both, the activation of the Na^+, K^+-ATPase as well as the conversion of glutamate to glutamine by the astrocyte specific enzyme glutamine synthetase (GS) cause a consumption of ATP. This in turn causes an enforced utilization of glucose and finally results in an activity-dependent supply of neurons (Voutsinos-Porche et al., 2003). Glutamine is transported back from the astrocyte to the presynaptic terminal before it is cleaved into glutamate and NH_4^+ by the enzyme phosphate-activated glumatinase (PAG).

As already mentioned, ALF and CLF cause an $[NH_4^+]$ increase in the brain (Swain et al., 1992a; Swain et al., 1992b). The predominant way to lower the NH_4^+ content is the metabolization of glutamate into glutamine. But it must be considered that

there is no real detoxification of NH_4^+, as it is released again in neurons by the PAG. Additionally, since the GS is working at near maximal capacity under normal physiological conditions, hyperammonemia likely causes an exceeding of the capacity to synthetize glutamine, in turn leading to an increase of the NH_4^+ content (Cooper and Plum, 1987; Felipo and Butterworth, 2002).

However, HE and hyperammonemia cause a disturbance of the glutamate-glutamine-cycle and thus lead to a changed glutamate-glutamine ratio in brain tissue. Increased glutamine levels have been found in HE patients and hyperammonemic animals suffering from liver enzymopathy (Lavoie et al., 1987; Ratnakumari et al., 1994). In parallel, the glutamate content is decreased, thus resulting in a decreased

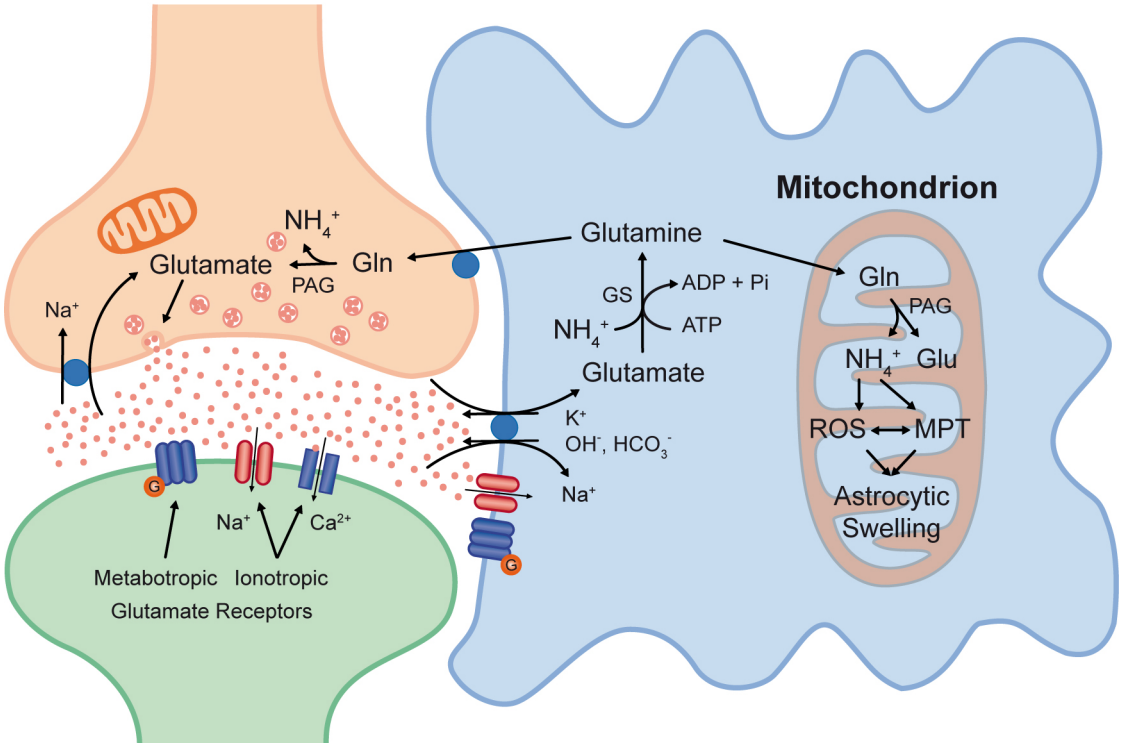

Fig. 8: Glutamate-glutamine-cycle and possible relevance for astrocyte swelling.
The glutamate-glutamine-cycle is an important process, by which released glutamate is transferred back to the presynaptic terminal to refill the glutamate pool. Glutamate is taken up into astrocytes by glutamate transporters and is converted under ATP consumption to glutamine by the incorporation of NH_4^+. After the transport of glutamine into the pre-synapse, glutamate is retrieved by the release of NH_4^+. Beside this, glutamine is transported into mitochondria for metabolization. The cleaved NH_4^+ is thought to cause an increased production of reactive oxygen species (ROS) and the mitochondria permeability transition (MPT) due to a collapse of the membrane potential of the inner mitochondrial membrane.

glutamate-glutamine ratio (Lavoie et al., 1987; Swain et al., 1992a; Kosenko et al., 1993; Blei et al., 1994). However, in the extracellular space and the cerebrospinal fluid, the glutamate content is increased (Watanabe et al., 1984; de Knegt et al., 1994; Michalak et al., 1996). The reason for the increased extracellular glutamate concentration can be either enhanced glutamate release from neurons and astrocytes or a reduced uptake into astrocytes or both (Rose, 2006).

1.5.6 NH_4^+-induced swelling of astrocytes

Beside the alteration of the glutamate-glutamine ratio, a swelling of astrocytes was observed during hyperammonemia (Ganz et al., 1989; Blei et al., 1994) that can be caused by several mechanisms. It was shown that the NKCC is activated during hyperammonemic conditions (Kelly et al., 2009; Kelly and Rose, 2010). It mediates an osmotic load by transporting four ions (1 Na^+, 1 K^+, 2 Cl^-) into the cell, thus causing swelling (Jayakumar et al., 2008). On the other hand, it was shown that inhibition of GS during hyperammonemic conditions with methioninsulfoximine (MSO) reduces three features of HE: 1) the accumulation of glutamine, 2) the formation of brain edema, and 3) swelling of astrocytes (Takahashi et al., 1991; Willard-Mack et al., 1996; Tanigami et al., 2005).

It was thought that glutamine itself causes cell swelling. But it was shown that the glutamine increase does not properly correlate with the cell swelling regarding the time course and concentration (Zwingmann et al., 2004; Jayakumar et al., 2006). Although the precise mechanism is still under investigation, it is thought that the production of reactive oxygen species (ROS) in mitochondria and a process termed "mitochondria permeability transition" (MPT) causes swelling of astrocytes (Fig. 8) (Norenberg et al., 2007). Evidence for this comes from experiments showing that inhibition of the enzyme PAG with 6-diazo-5-oxo-L-norleucine (DON) inhibits the formation of ROS, the MPT, and the NH_4^+-induced swelling (Jayakumar et al., 2004; Rama Rao et al., 2005; Jayakumar et al., 2006). Despite this, the mechanism how MPT and ROS formation cause astrocyte swelling during hyperammonemia is unknown.

1.6 Aim of this study

Astrocytes play an important role in the pathogenesis of HE, as they exhibit swelling leading to intracranial hypertension (Norenberg et al., 2007) and convert glutamate NH_4^+-enforced into glutamine causing a reduction in brain glutamate content (Blei et al., 1994). Furthermore, during hyperammonemic conditions, the ion distribution in astrocytes is impaired (Kelly and Rose, 2010). As in the presence of NH_4^+, astrocytes display a depolarized E_M (Allert et al., 1998) and $[K^+]_o$ is increased (Alger and Nicoll, 1983), K^+ homeostasis might be impaired.

Up to now, the depolarizing effect of NH_4^+ was studied only in primary cultures from cortical astrocytes (Allert et al., 1998) or in glial cells of bee retina (Marcaggi et al., 2004). The electrophysiological properties of astrocytes under hyperammonemic conditions in the context of the surrounding tissue remained unexplored. Such an investigation becomes even more relevant by the fact that NH_4^+ causes an increase of the $[K^+]_o$ in the hippocampus (Alger and Nicoll, 1983). However, this result was treated as a side product and the question regarding the amount and the mechanisms of the $[K^+]_o$ increase was not addressed.

In this study we addressed the question, whether these NH_4^+-induced alterations of the electrophysiological properties of astrocytes and $[K^+]_o$ are linked to a disturbed K^+ homeostasis that in turn might have implications for the pathology of HE.

To answer this question, we performed whole-cell patch-clamp recordings of identified SR101-labeled astrocytes and K^+-sensitive measurements in the *stratum radiatum* of acute mouse hippocampal slices to analyze the NH_4^+-induced changes in both, the electrophysiological properties of astrocytes and the $[K^+]_o$. Additionally, we took advantage of pharmacological as well as genetic approaches to indentify the underlying mechanisms.

2 Materials and methods

2.1 Tissue preparation and identification of astrocytes

The study and all experiments were carried out in accordance with the guidelines of the Heinrich-Heine-University (HHU) Düsseldorf and University of Bonn Medical Center as well as the European Communities Council Directive (86/609/EEC) and approved by the institutional animal care and use committee. Preparation of acute hippocampal slices (250 µm) from Balb/c mice (postnatal days 3 - 4 (P3), 7 - 10 (P7), 13 - 16 (P13), 18 - 21 (P18)) and C57BL6 Kir4.1 -/- mice (postnatal days 7 - 10 (P7)) (Kofuji et al., 2000) was performed using standard techniques (Meier et al., 2006; Kafitz et al., 2008).

Animals were decapitated and their brains were rapidly isolated. Animals older than P12 were anesthetized with CO_2 prior to decapitation. After sectioning, slices for $[K^+]_o$ measurement were kept at 34 °C for 30 min in artificial cerebrospinal fluid (ACSF). For whole-cell patch-clamp experiments, slices were kept at 34 °C for 20 min in ACSF with 0.5 - 1 µM sulforhodamine 101 (SR101) followed by a 10 min incubation in SR101-free ACSF at 34 °C. This procedure results in the specific staining of astrocytes (Kafitz et al., 2008). Afterwards, slices were kept in ACSF at room temperature (RT, 19 - 22 °C) until they were used for experiments, which were also performed at RT.

The ACSF contained (in mM): 125 NaCl, 2.5 KCl, 2 $CaCl_2$, 1 $MgCl_2$, 1.25 NaH_2PO_4, 26 $NaHCO_3$, and 20 glucose, bubbled with 95 % O_2 and 5 % CO_2 to result in a pH of 7.30. Solutions containing NH_4^+ or altered $[K^+]$ were prepared by equimolar substitution of Na^+. Solutions had a final osmolarity of 310 ± 5 mOsm/L. Pharmacological substances were applied via bath perfusion or by focal pneumatic ejection (PDES-DXH, NPI Electronic GmbH, Tamm, Germany). In the latter case, pipettes similar to those for patch-clamp recordings were used (see below) applying 8 psi for 2 s in patch-clamp experiments and 200 ms in $[K^+]_o$ measurements. Chemicals were purchased from Sigma, except for tetrodotoxin (Alomone Labs, Jerusalem, Israel or Biotrend Chemicals, Cologne, Germany).

2.2 Whole-cell patch-clamp

To investigate the effect of NH_4^+ on the electrophysiological properties of astrocytes, somatic whole-cell recordings were done. Cells were patched in a maximal depth of ~20 µm and were obtained at an upright microscope (Nikon Eclipse FN1, 60x water immersion objective, N.A. 1.00, Nikon Europe, Düsseldorf, Germany) using an EPC10 amplifier and "PatchMaster"-software (HEKA Elektronik, Lambrecht, Germany). The pipette solution contained (in mM): 120 K-$MeSO_3$, 24 KCl, 10 HEPES (N-(2-Hydroxyethyl)piperazine-N′-2-ethanesulfonic acid), 12 NaCl, 4 Mg-ATP, and 0.4 Na_3-GTP, pH 7.30. In experiments investigating the effect of Ca^{2+} and those done on Kir4.1 -/- animals, 4 mM EGTA (glycol-bis(2-aminoethylether)-N,N,N′,N′-tetraacetic acid) was added to the pipette solution. Patch pipettes (2.5 - 3.5 MΩ) were drawn from borosilicate glass capillaries (Hilgenberg, Waldkappel, Germany) using a vertical puller (PP-830, Narishige, Japan). For measurement of membrane currents, cells were clamped to a membrane potential of -85 mV (unless stated otherwise), liquid junction potential was corrected. Compensation of series resistance and slow capacitance was not performed, because of insufficient voltage control of mature astrocytes (Zhou et al., 2009). For determination of IV-relationships, a step-wise or ramp-like protocol ranging from -150 to +50 mV was used. The former one had 10 mV increments. To separate passive currents from voltage-gated currents in the step protocol, online leak subtraction (P/4) was performed. Signals were sampled at 50 kHz and filtered at 2.9 and 10 kHz. Beside this, all voltage- and current-clamp measurements were sampled at 50 Hz. Measurements were rejected, if the series resistance exceeded 10 MΩ. Data were processed and analyzed by employing "IGOR Pro"-Software (WaveMetrics, Inc., Lake Oswego, OR).

2.3 Measurement of extracellular potassium ($[K^+]_o$)

To analyze the effect of NH_4^+ on the $[K^+]_o$, we used double-barreled, K^+-sensitive microelectrodes placed ~50 µM deep in the *stratum radiatum* of the CA1 region. Briefly, two 7-cm-long glass capillaries with filament (Clark Electromedical Instruments, Harvard Apparatus Ltd., Kent, UK) were simultaneously pulled (Typ PE-2, Narishige, Japan). One barrel was silanized by exposure to the vapor of

hexamethyldisilazane (Fluka, Buchs, Switzerland) at 40 °C for 90 min, while the other one was prevented from being silanized by vapor pressure. The tip of the silanized barrel was filled with a liquid neutral K^+ carrier based on valinomycin (Ionophore I, Cocktail B, Fluka, Buchs, Switzerland) and backfilled with 100 mM KCl (Neumann et al., 2001). The reference barrel was filled with HEPES-ringer containing (in mM): 125 NaCl, 2.5 KCl, 1.25 NaH_2PO_4, 2 $CaCl_2$, 2 $MgCl_2$, and 25 HEPES. A chlorinated silver wire was inserted into each barrel, which was then sealed with dental wax. The resistance of the K^+-sensitive channel was 10 - 20 GΩ, that of the the reference channel 30 - 100 MΩ. The electrodes were calibrated in CO_2/HCO_3^--free saline with 152 mM Na^+, 25 mM HEPES and different $[K^+]$. The electrode slope (s) was given by the equation:

$$s = \frac{\Delta V_{K_o}}{\Delta pK_o} \qquad (1),$$

with ΔV_{Ko} representing the voltage shift upon a given $[K^+]$ change (ΔpK_o). Because NH_4^+ is detected by valinomycin, the artifact was determined exposing all solutions, used in the experiment, to the electrode withdrawn from the slice. The peak $[K^+]_o$ was calculated by the equation:

$$peak\left[K^+\right]_o = \left[K^+\right]_{ref} * \left(10^{\frac{\Delta V_{\max}}{s}} - 10^{\frac{\Delta V_{art}}{s}} + 1\right) \qquad (2),$$

with $[K^+]_{ref}$ resembling the initial $[K^+]_o$ (2.5 mM), ΔV_{max} being the sum of NH_4^+-induced artifact and $[K^+]_o$ increase, ΔV_{art} representing the NH_4^+-induced artifact, and *s* the slope of the electrode (Eq1) (Fig. 12*B*). The K^+ undershoot ($\min[K^+]_o$) upon removal of NH_4^+ was calculated by the equation:

$$\min\left[K^+\right]_o = \left[K^+\right]_{ref} * \left(-10^{\frac{\Delta V_{\min}}{s}} + 1\right) \qquad (3),$$

with ΔV_{min} resembling the $[K^+]_o$ decrease (Fig. 12*B*). Data were processed and analyzed by employing “Origin”-Software (Origin Lab Coorporation, Northampton, MA).

2.4 Identification of Kir4.1 -/- mice

In order to confirm the results from the Ba^{2+} experiments, we took advantage of using mice with a genetic inactivation of the K^+ inward rectifier (*KIR*) channel 4.1. Kir4.1 -/- mice were generated by a replacement of the coding region for the two transmembrane segments and a part of the C-terminus of the Kir4.1 subunit (amino acids 33 - 266) by a neomycin resistance gene causing a loss of function and a mislocation of the created protein (Kofuji et al., 2000). We verified the knock out status of designated Kir4.1 -/- mice by determination of the electrophysiological properties of patch-clamped astrocytes, immunohistochemical labeling against GFAP (glial fibrillary acidic protein) and Kir4.1 (K^+ inward rectifier channel 4.1), and genotyping.

One brain hemisphere from Kir4.1 -/- animals and their wild type littermates, which were prepared for acute experiments, was immediately fixed for 2 days at 4 °C in 4 % paraformaldehyde. Fixed tissue was cut with a Vibratome (HM650V, Microtom, Microm International GmbH, Walldorf, Germany) in 12 - 15 µM thick slices that were immunohistochemically processed for GFAP (Millipore, Chemicon AB5541, Schwalbach/Ts., Germany, dilution 1:250 or Sigma-Aldrich G3893; Taufkirchen, Germany, dilution 1:500) and Kir4.1 (Alomone Labs APC-035, Jerusalem, Israel, dilution 1:100). Secondary antibodies were fluorescence conjugated with Alexa Fluor 488/594 (Invitrogene, A11039/A11008, Darmstadt, Germany, dilution 1:100).

Fixed tissue was permeabilized with 0.25 % Triton X-100 and incubated with primary and secondary antibodies, each for 2 h. Non-specific binding of antibodies was reduced using 0.5 % BSA, 2 % NGS, and 3 % milk powder. At last nuclei were marked with DAPI (4′,6-Diamidin-2-phenylindol, Invitrogene, Molecular Probes D3571, 2.1 µM) for 15 min. All steps were performed at RT. Labeled slices were coverslipped and documented with confocal laser scanning microscope (Nikon C1) based on a Nikon Eclipse E600FN (60x water immersion objective, N.A. 1.00). Images of all test groups were equally processed for maximum projection and overlaid using “ImageJ”-software. Negative controls showed no background labeling excluding cross talk and bleeding over. The partially remaining weak labeling of somata was caused by the specificity of the utilized antibody detecting the amino acids 356 - 375 of the C-terminus.

For genotyping of Kir4.1 knockout mice, DNA was isolated from mouse tails using a DNA isolation Kit (Jena Analytik, Jena, Germany). About 100 ng of DNA was used for PCR amplification of Kir4.1 genomic DNA using the following oligonucleotides:

forward, 5'-CTTCAGCCAGCATGCCGTTGTG;

reverse, 5'-AGGCGTGAACTCGTAACCCCAGAG.

For the detection of the neomycin resistance gene the following oligonucleotides were used:

forward, 5'-ACATCGCATCGAGCGAGCAC;

reverse, 5'-AAGGCGATGCGCTGCGAATC.

35 PCR cycles were performed using the Hot Taq DNA polymerase (Peqlab, Erlangen, Germany). The lengths of the PCR products were 400 bp (Kir4.1) and 354 bp (neomycin resistance gene).

2.5 Statistics

Unless otherwise specified, data are presented as means ± s.e.m. and were statistically analyzed by one-tailed non-/paired Student´s *t*-test; *p* represents probability values, n.s. = not significant, * $p < 0.05$, ** $p < 0.01$, *** $p < 0.001$; *n* represents the number of independent experiments.

3 Results

3.1 Properties of SR101-labeled cells

To unerringly identify astrocytes prior to experiments, we used SR101-labeling (Fig. 9) and the electrophysiological characterization (Fig. 10) of patch-clamped cells. The labeling of acute hippocampal slices with SR101 resulted in a selective staining of astrocytes as reported earlier (Kafitz et al., 2008). Cells in layers containing pyramidal (CA3 to CA1) or granule cells (dentate gyrus) remained unstained. SR101-positive cells in the *stratum radiatum* showed properties of classical astrocytes (Steinhauser et al., 1992; Kressin et al., 1995; Bordey and Sontheimer, 1997; D'Ambrosio et al., 1998; Bordey and Sontheimer, 2000; Zhou et al., 2006; Kafitz et al., 2008), comprising a highly negative membrane potential (E_M) and a low and with development decreasing membrane resistance (R_M). During the early postnatal development the amount of cells, which exhibited currents through voltage activated potassium channels decreased continuously (Fig. 10; Fig. 11, Supplementary Table 1). Finally, positive current injection failed to elicit action potentials in any of the cells investigated ($n = 510$; data not shown). By doing that, we had got a reliable measure for astrocytic identity.

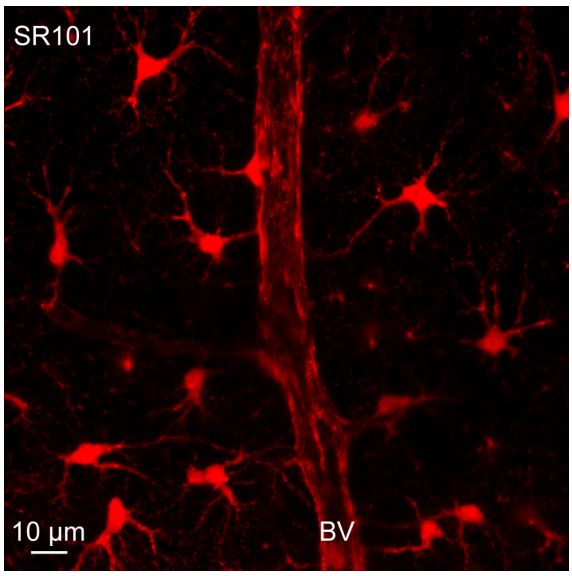

Fig. 9: SR101-labeled astrocytes in the mouse hippocampus
Maximum intensity projection of a confocal z-stack with 14 slices, each step 1 µm. Section of the *stratum lacunosum moleculare* in the CA1 region. Incubation of the hippocampal slice obtained from a mouse at P14 with the red fluorescent dye SR101 results in a specific labeling of astrocytes. Since astrocytic processes extensively ensheath blood vessels (BV), those can be identified by the SR101-labeling.

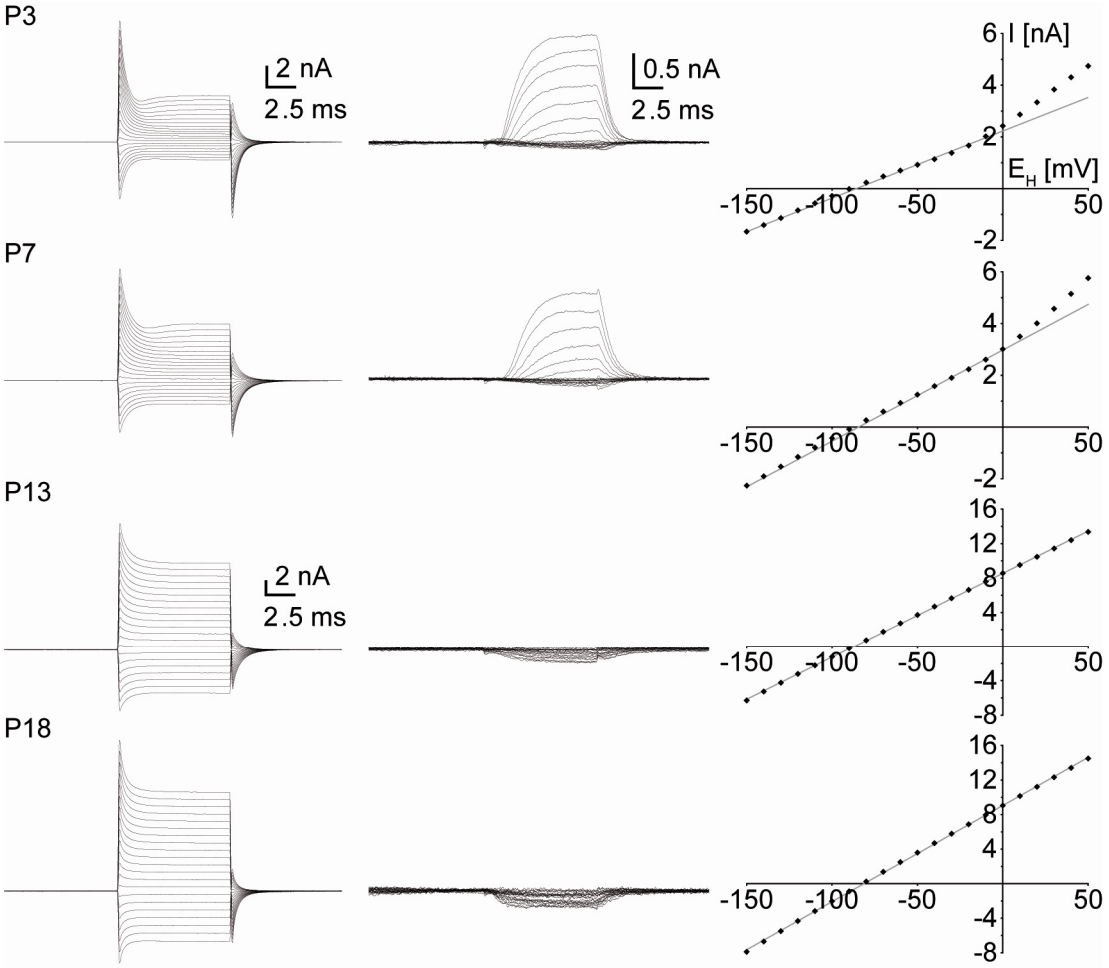

Fig. 10: IV-relationship of SR101-positive cells during early postnatal development.
Patched cells were held at −85 mV and subjected to 10 ms voltage steps ranging from −150 to +50 mV at 10 mV increments and the resulting membrane currents before (left) and after leak subtraction (middle) were recorded. The IV plots (right) depict the amplitudes of the resulting currents at 8 to 10 ms after the start of the voltage step of the respective cell, the grey lines show the linear regression curves. Astrocytes from animals at P3 and P7 predominantly showed non-linear IV-relationships. At P13 and P18 animals, mostly linear IV-curves were found.

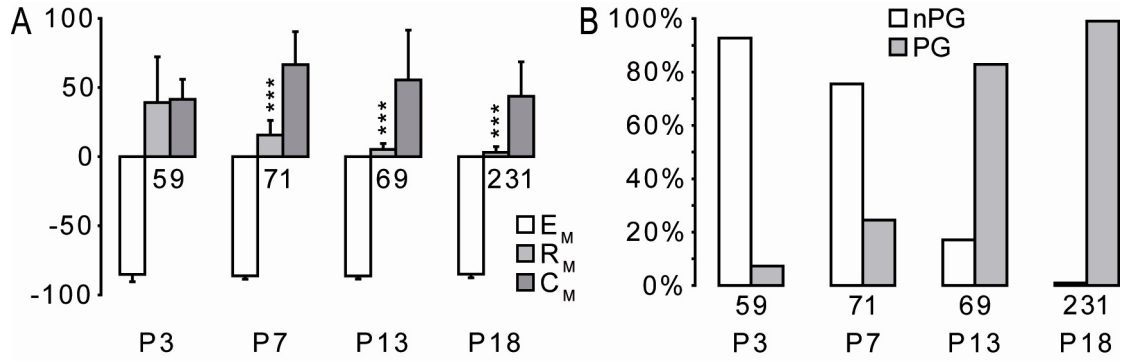

Fig. 11: Developmental changes of astrocytic membrane properties.
(A) During the early postnatal development, astrocytes displayed an unchanged highly negative E_M [mV] and a significant decreasing R_M [MΩ], while C_M [pF] was not significantly altered. (B) Quantification of the amount of astrocytes with non-linear (non-passive glial cells, nPGs) or linear (passive glial cells, PGs) IV-curves on the total number of SR101-positive cells at different developmental stages. Between P7 and P13 was a transition from nPGs to PGs. It must be considered that the developmental dependent decrease of RM likely caused at least an underestimation of the proportion of nPGs due to insufficient voltage control. All values are given as mean ± S.D. *n*-Values are contained under the bars. ***: $p < 0.001$.

3.2 NH_4^+-induced depolarization and $[K^+]_o$ increase

In order to determine the effect of NH_4^+ on astrocytes in acute hippocampal slices, 5 mM NH_4^+ was equimolar substituted for Na^+ in the ACSF. The application of NH_4^+ for 10 min caused a depolarization of ~8 mV, which was reduced at P3 and occurred age-independently with a half time of 52 ± 8 s ($n = 114$) (Fig. 12*A*, Supplementary Table 2). In approximately two third of the experiments the peak depolarization was followed by a slow repolarization of 1 - 2 mV, which turned to a plateau, as a prolongation of the NH_4^+ application up to 30 min did not result in further repolarization (data not shown). Upon removal of NH_4^+, the astrocytes temporarily hyperpolarized before E_M completely recovered to its initial value. The amplitude of the NH_4^+-induced depolarization increased during early postnatal development (Fig. 12*A*), while the time course remained essentially stable (data not shown).

To show early and late developmental NH_4^+-induced $[K^+]_o$ increase, hippocampal slices from P3 and P18 mice were taken. The application of 5 mM NH_4^+

caused a transient $[K^+]_o$ increase of ~0.4 mM at P3 and ~1 mM at P18, which reached its half maximum age-independently within 76 ± 3 s (n = 55). Subsequently, $[K^+]_o$ began to decrease and within 20 - 25 min $[K^+]_o$ returned to its basal level of 2.5 mM. Upon NH_4^+ removal, $[K^+]_o$ temporarily decreased below baseline, reached age dependently a half minimum after 76 ± 11 s at P3 (n = 5) and 115 ± 6 s at P18 (n = 42) and then recovered within ~20 min (Fig. 12*B*, Supplementary Table 3). This $[K^+]_o$ undershoot was independent of the duration of the NH_4^+ application, if the minimal time period was 10 min. A reduction of the application period shorter than 10 min led to a reduced $[K^+]_o$ increase.

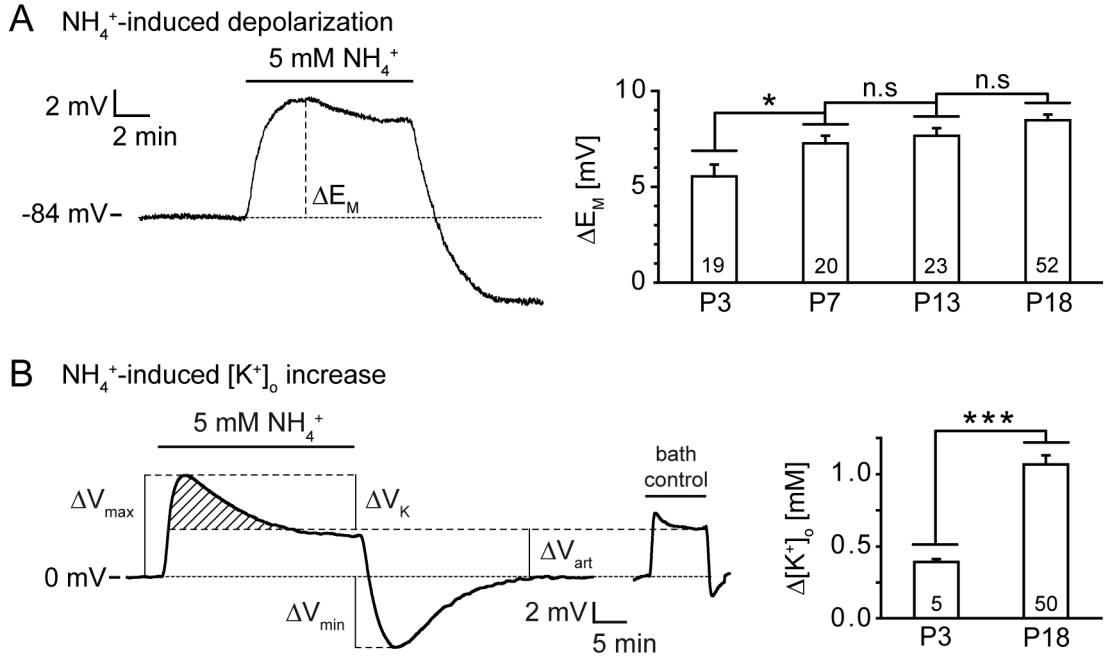

Fig. 12: NH_4^+-induced changes of astrocytic E_M and $[K^+]_o$ in acute hippocampal slices.
(A) Left: Effect of 5 mM NH_4^+ on E_M of an astrocyte at P18. Bath application of NH_4^+ caused a depolarization of about 8 mV, which was maximal after ~2 min; subsequently the cell repolarized by ~2 mV. After removal of NH_4^+, a hyperpolarization occurred before the cell recovered to initial E_M. Right: Age-dependence of the membrane depolarization (ΔE_M) of astrocytes induced by 5 mM NH_4^+. At P3, astrocytes exhibited significantly smaller depolarization compared to that from older animals. (B) Left: Effect of 5 mM NH_4^+ on $[K^+]_o$ in the *stratum radiatum* of a slice obtained from P18. Bath control: Effect of 5 mM NH_4^+ on the electrode potential after withdrawal of the electrode. Due to simultaneous detection of K^+ and NH_4^+ by the ionophore (ΔV_{max}), the NH_4^+-dependent component (ΔV_{art}) was estimated afterwards to calculate the $[K^+]_o$ increase (hatched area). Bath application of NH_4^+ caused a transient $[K^+]_o$ increase of about 1 mM that vanished within 20 - 30 min. Upon removal of NH_4^+, $[K^+]_o$ decreased temporarily below baseline (ΔV_{min}). Right: Changes in $[K^+]_o$ induced by 5 mM NH_4^+ in hippocampal slices from P3 and P18. During development, the $[K^+]_o$ increase was significantly gained. n-Values are contained within the bars.

Because of the high K^+ permeability of the cell membrane, astrocytic E_M strongly depends on $[K^+]_o$ and $[K^+]_i$ (Kimelberg et al., 1979; Walz et al., 1984; Anderson et al., 1995). In order to test, whether the NH_4^+-induced $[K^+]_o$ increase is sufficient to explain the NH_4^+-induced membrane depolarization, $[K^+]$ in the ACSF was raised age-dependently from 2.5 to 2.9 mM at P3 or, respectively, 3.5 mM at P18. The increase of $[K^+]_o$ caused a depolarization of astrocytes (ΔE_M: P3: 2.3 ± 0.1 mV, $n = 4$; P18: 5.2 ± 0.3 mV, $n = 10$), which was significantly smaller than the according NH_4^+-induced depolarization (P3 and P18: $p < 0.001$), and had a significantly reduced half time of 18 ± 4 s at P18 compared to the depolarization induced by NH_4^+ ($p < 0.001$) (data not shown). At P3, however, the half time was not significantly reduced (40 ± 3 s; $p = 0.293$). Altogether, the NH_4^+-induced depolarization is only partially due to NH_4^+-induced $[K^+]_o$ increase as the NH_4^+-induced depolarization exceeded the depolarization induced by the increase of $[K^+]_o$ and at least one further mechanism has to be considered.

3.3 Relative membrane permeability

In order to determine the concentration-dependence of the NH_4^+ effect on $[K^+]_o$ and E_M, we varied $[NH_4^+]$ in between 0.5 and 20 mM (Fig. 13*A*, *C*). $[NH_4^+] > 20$ mM caused an irreversible depolarization of the astrocytes and hence were not evaluated.

A $[K^+]_o$ increase was detected reliably at 1 mM NH_4^+; at higher $[NH_4^+]$, the $[K^+]_o$ increase became continuously larger, showing no sign of saturation (Fig. 13*A*, Supplementary Table 3). Therefore, E_M of astrocytes was expected to rise stronger with increasing $[NH_4^+]$.

We then patch-clamped astrocytes and altered $[K^+]$ in the ACSF in the range from 0.5 - 5 mM to determine the relationship between $[K^+]_o$ and E_M. A reduction of $[K^+]_o$ resulted in hyperpolarization and an increase in depolarization (Fig. 13*B*). The relationship between $[K^+]_o$ and E_M did not correlate with Nernst equation (Eq4), but could be well described with the Goldman-Hodgkin-Katz (GHK) equation (Eq5), adjusting the relative Na^+ permeability to 0.015.

We next applied increasing $[NH_4^+]$ and astrocytes depolarized accordingly (Fig. 13*C*, Supplementary Table 2). The measured E_M did not follow a relationship based on a Michaelis-Menten equation, but on a GHK equation (Eq6), which includes a relative

NH_4^+ permeability of 0.33, the relative Na^+ permeability from Eq5, and the measured $[NH_4^+]$-dependent peak $[K^+]_o$, respectively. The $[NH_4^+]_i$ was set to 0, as the intracellular solution diluted entering NH_4^+. (For details regarding Eq4 - 6 see supplementary data). Taken together, these results suggest that NH_4^+ substitutes for K^+ at respective channels, which however have a lower permeability for NH_4^+.

3.4 NH_4^+-induced inward current

We next investigated the effect of NH_4^+ on the membrane current of astrocytes. Bath application of 5 mM NH_4^+ caused an inward current (I_{NH4+}), which corresponded to the NH_4^+-induced changes in E_M, in showing a peak current that was followed by a small recovery (Fig. 14*A*, Supplementary Table 2). During the first two weeks of postnatal development, I_{NH4+} increased significantly and then remained stable.

The response to hyperpolarizing pulses (ΔE_H = -5 mV) was used to determine membrane resistance (R_M), input resistance (R_{In}) and series resistance (R_S). In the presence of NH_4^+, R_M decreased significantly (Fig. 14*B*, Supplementary Table 2). The reduction itself decreased with age of the experimental animals, because of the developmental decrease of astrocytic R_M (Supplementary Table 1).

The IV-relationship of the cell before and during NH_4^+ application was measured by linearly shifting E_H from -150 to +50 mV. At P7, NH_4^+ caused a parallel shift of the IV-curve of about 8 mV (Fig. 14*C*). This value is close to the average NH_4^+-induced depolarization measured in current-clamp mode (Fig. 12*A*). There was virtually no change in the rectification of the IV-relationship by reducing current amplitudes.

Taken together, astrocytes exhibited an NH_4^+-induced inward current suggesting either an influx of NH_4^+ into the cells or a competitive inhibition of K^+ channels preventing an efflux of K^+. The latter case is unlikely, because of the shifted but otherwise unaffected IV-relationship.

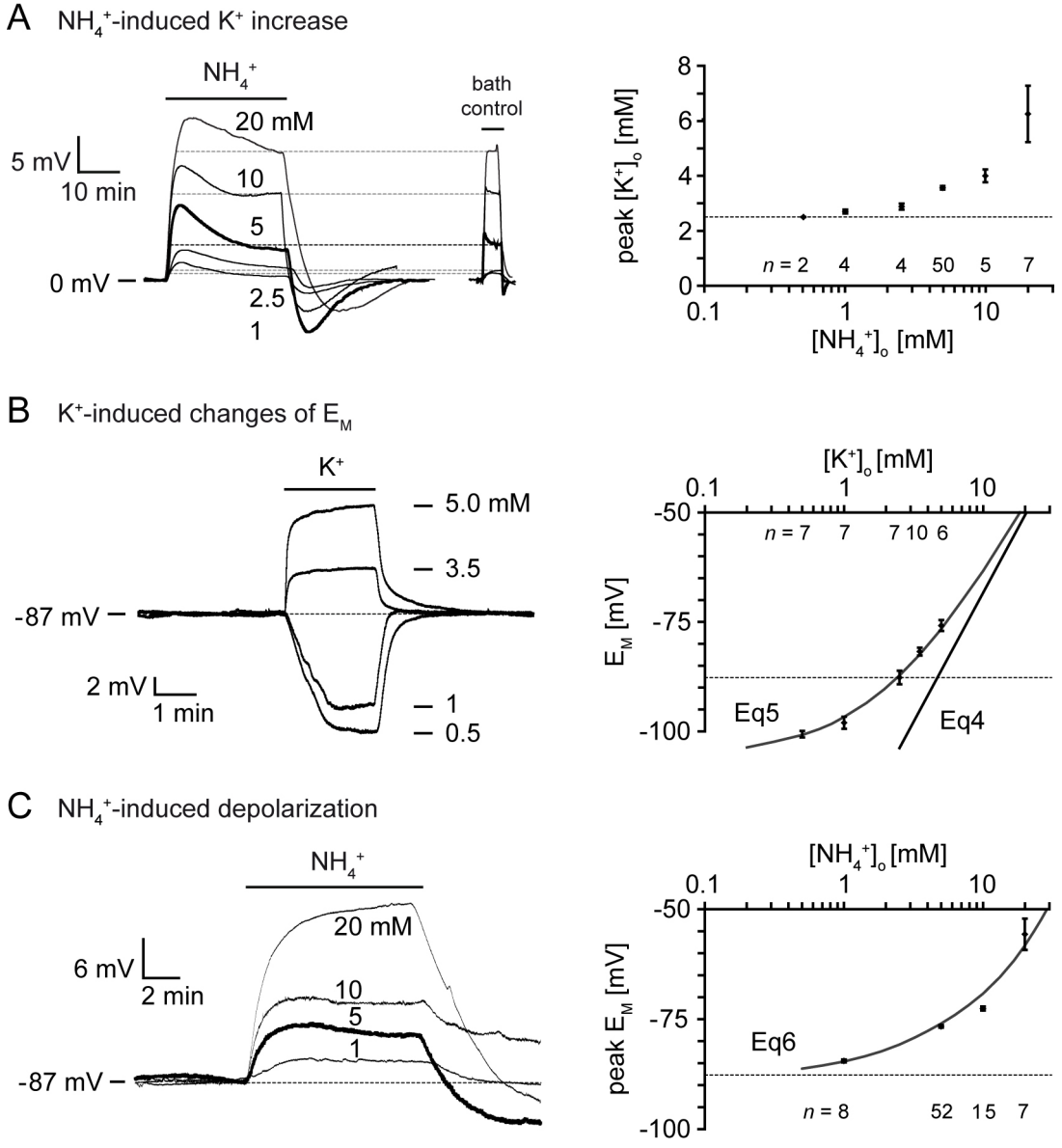

Fig. 13: Concentration-dependence of NH_4^+-induced $[K^+]_o$ increase and relative membrane permeability for K^+, Na^+ and NH_4^+.

(A) Left: Changes in $[K^+]_o$ induced by different $[NH_4^+]_o$ at P18; superimposing of single traces. Right: Dependence of maximal $[K^+]_o$ in the presence of NH_4^+ on the $[NH_4^+]_o$. With increasing $[NH_4^+]_o$ peak $[K^+]_o$ raised showing no sign of saturation. Dashed line indicates initial $[K^+]_o$. (B) Left: Effect of changing $[K^+]_o$ on E_M of an astrocyte at P18; superimposing of single traces. Right: Relation between E_M and $[K^+]_o$ at P18. The straight line labeled with Eq4 illustrates the Nernst potential of K^+ ($R^2 = 0.918$), whereas Eq5 shows the relationship between $[K^+]_o$ and E_M given by the GHK equation with a relative Na^+/K^+ permeability (P_{Na}/P_K) of 0.015 ($R^2 = 0.997$). (C) Left: Changes in E_M of astrocytes at P18 induced by different $[NH_4^+]_o$; superimposing of single traces. Right: The curve shows the calculated relationship between $[NH_4^+]_o$ and E_M based on the GHK equation (Eq6), assuming a relative NH_4^+/K^+ permeability (P_{NH4}/P_K) of 0.33 and correcting $[K^+]_o$ for the peak $[K^+]_o$, as determined at different $[NH_4^+]_o$ (see A; $R^2 = 0.981$). *n*-Values of respective mean values are located near x-axes.

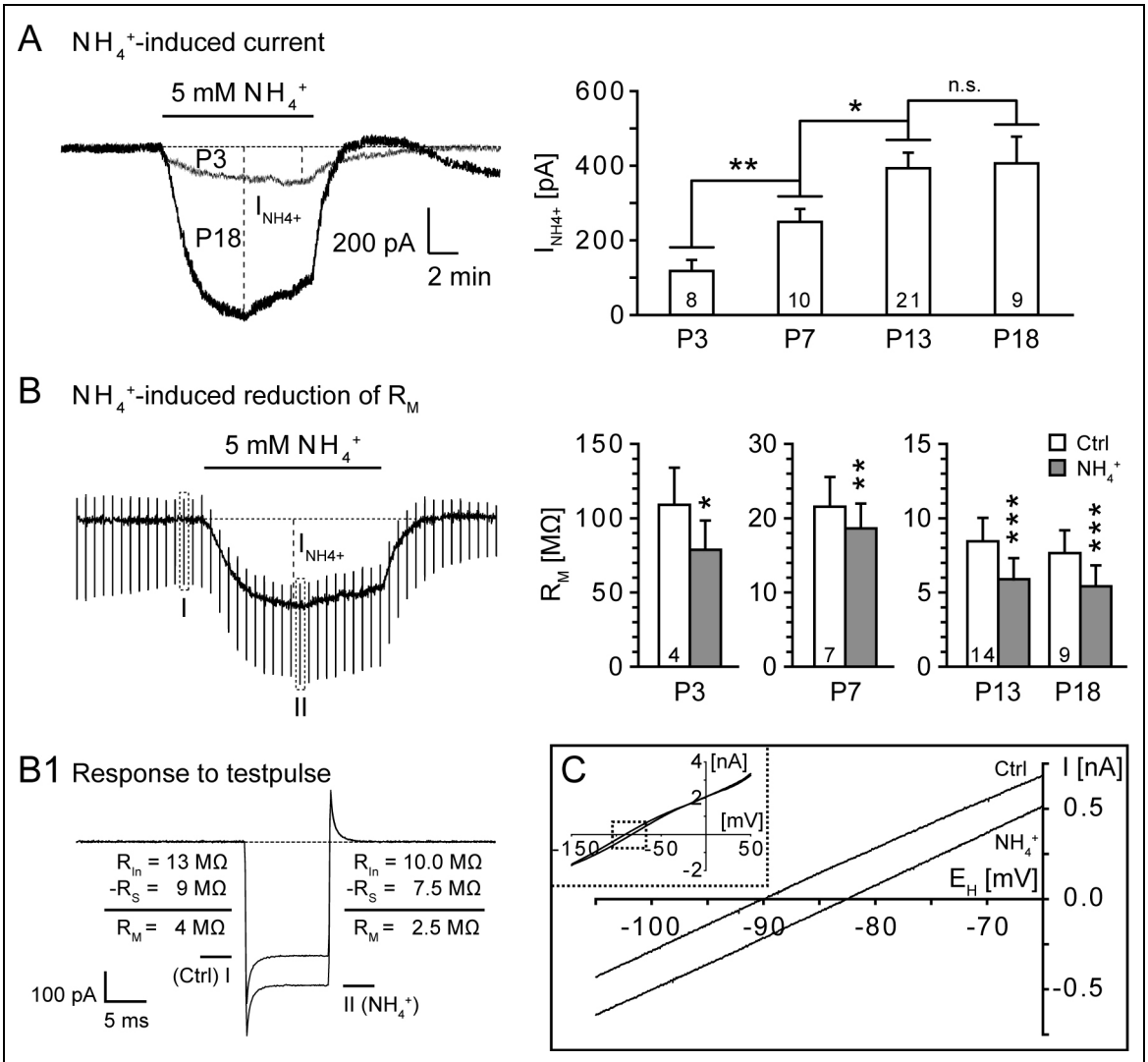

Fig. 14: NH_4^+-induced inward current (I_{NH4+}) and reduction of membrane resistance (R_M).
(A) Left: Measurements of I_{NH4+} at different developmental stages. Right: During the first two weeks of development, the amplitude of I_{NH4+} increased significantly. (B) Left: The response to hyperpolarizing pulses (-5 mV) every 30 s revealed a reduction in input resistance (R_{In}) and after subtraction of series resistance (R_S) a decrease in R_M (P18). Right: The NH_4^+-induced reduction of R_M was present at all developmental stages. (C) Left: IV-curves before (black line) and during (grey line) bath application of 5 mM NH_4^+. NH_4^+ caused a averaged parallel shift in the IV-relationship of about 8 mV that is comparable to the NH_4^+-induced depolarization (see Fig. 12*A*). Right: Magnification of the IV-curves shown left. *n*-Values are contained within the bars.

3.5 Pathway of NH_4^+-induced depolarization and $[K^+]_o$ increase

In order to highlight pathways for the NH_4^+-induced depolarization and $[K^+]_o$ increase, several inhibitors of different channels and transporters were tested at P18. Results were summarized (Supplementary Table 4), but not depicted. (For patch-clamp experiments including Ba^{2+} see next chapter).

TTX (500 nM) and bumetanide (100 µM) failed to affect the NH_4^+-induced depolarization and $[K^+]_o$ increase or to alter steady-state conditions, indicating its independence from neuronal action potentials and sodium-potassium-chloride co-transport (NKCC). Additionally, the depolarization of astrocytes was independent from TEA (5 mM) sensitive voltage activated K^+ channels (K_V), as well as Ca^{2+}-activated K^+ channels (K_{Ca}), because the Ca^{2+} chelator EGTA (4 mM) in the pipette solution had no altering effect. CNQX (10 µM) and D-L-AP5 (100 µM) were simultaneously used to exclude AMPA and NMDA receptor-mediated K^+ release from postsynaptic terminals as a source for the $[K^+]_o$ increase (χ^2 test). In addition, Ba^{2+} (100 µM) as a blocker of Kir channels failed to reduce $[K^+]_o$ increase (χ^2 test) and did not alter baseline $[K^+]_o$.

3.6 Reduction of the NH_4^+-induced depolarization and current by Ba^{2+}

While not affecting baseline $[K^+]_o$ and its NH_4^+-induced increase, Ba^{2+} effectively reduced the NH_4^+-induced depolarization by 50 - 67 % ($p < 0.001$) (Fig. 15*A*, Supplementary Table 4). It must be considered, that Ba^{2+} itself caused a depolarization (ΔE_M: P7: 19.5 ± 1.0 mV, $n = 9$; P18: 7.9 ± 0.5 mV, $n = 7$) that might reduce the NH_4^+-induced depolarization by decreasing the driving force for the NH_4^+ influx. Therefore, we repeated the experiments in voltage-clamp mode showing a significant reduction of I_{NH4+} by 62 - 77 % ($p < 0.001$) (Fig. 15*B*, Supplementary Table 4). Also in the presence of Ba^{2+}, NH_4^+ caused a reduction of R_M, which, however, increased by a factor of 2 - 3 than under control conditions (ΔR_M: P7: 10.1 ± 4.6 MΩ, $n = 3$; P13: 5.3 ± 1.1 MΩ, $n = 4$; data not shown). It must be considered, that Ba^{2+} itself led to an increase in R_M (ΔR_M: P7: 73 ± 17 MΩ, $n = 6$; P13: 6.9 ± 1.6 MΩ, $n = 4$).

In voltage-clamp mode, a ramp-like stimulation protocol was performed to determine the astrocytic IV-relationship during the measurement (Fig. 15*C*). Ba^{2+}

reduced current amplitudes at negative potentials, indicating a loss of Kir currents as revealed by subtraction from control IV-curve (P7, *n* = 5). Independent from that, NH_4^+ still caused a shift of the IV-relationship. Taken together, the Ba^{2+}-mediated reduction of both, the NH_4^+-induced depolarization as well as current suggest that NH_4^+ entered the astrocytes via Kir channels.

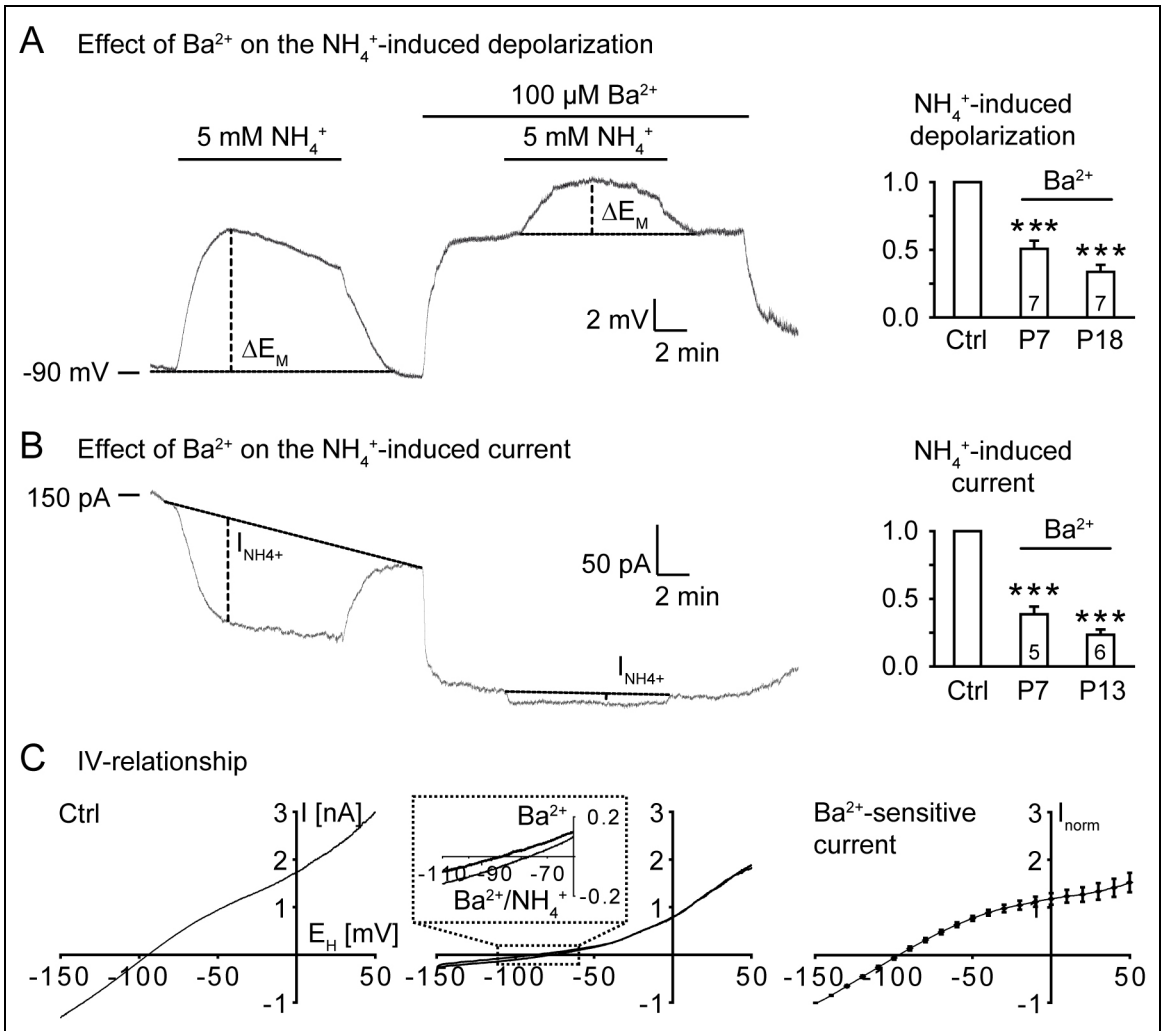

Fig. 15: Effect of Ba^{2+} on NH_4^+-induced depolarization and membrane current.
(A) Left: Measurement of astrocytic E_M at P18. In the presence of Ba^{2+}, the NH_4^+-induced depolarization was reduced from 8.5 to 3.4 mV. Right: The inhibiting effect of Ba^{2+} on the NH_4^+-induced depolarization increased with age. (B) Left: Measurement of I_{NH4+} at P7. In the presence of Ba^{2+}, I_{NH4+} was reduced from 134 to 9 pA. Right: The inhibiting effect of Ba^{2+} on the NH_4^+-induced current increased with age. *n*-Values are contained within the bars. (C) From left to right: IV-curves under control conditions, in Ba^{2+} (100 µM) with and without NH_4^+ (5 mM), and after subtraction of IV-curves in Ba^{2+} from control and normalization to the mean value at E_H = -150 mV (P7; n = 5). Adding Ba^{2+} to ACSF caused a reduction in the current amplitude at negative potentials turning the IV-relationship from linear to outward rectifying. Magnification shows a shift in the IV-relationship after addition of NH_4^+. The Ba^{2+}-sensitive current showed characteristic inward rectification, indicating a loss of Kir currents.

3.7 Astrocytes from Kir4.1 -/- lack sensitivity to NH_4^+

In order to confirm the conclusions from the Ba^{2+} experiments, we took advantage of using Kir4.1 -/- mice (Kofuji et al., 2000). Double labeling of astrocytes with antibodies against GFAP and Kir4.1 showed a loss of Kir4.1 immunoreactivity (Fig. 16*A*). Patch-clamped astrocytes from Kir4.1 -/- mice were significantly depolarized and for clamping to -85 mV, a huge holding current was necessary (Fig. 16*B*, Supplementary Table 1). The IV-relationship showed slightly reduced current amplitudes at negative holding potentials (E_H). The weaker outward rectification of astrocytes from Kir4.1 -/- mice compared to Ba^{2+}-treated astrocytes from wild type mice (Fig. 15*C*) is presumably due to gap junction coupling that contributes to the linear IV-relationship of passive astrocytes (Blomstrand et al., 2004).

We determined the effect of NH_4^+ on astrocytes from Kir4.1 -/- mice and wild type littermates by pressure application of 5 mM NH_4^+. Astrocytes from wild type mice exhibited a depolarization (ΔE_M: 5.8 ± 0.9 mV, $n = 15$) that lasted as long as the application period (Fig. 16*C*). In voltage-clamp mode, NH_4^+ caused an inward current (74 ± 16 pA, $n = 17$), which corresponded to the NH_4^+-induced depolarization. By contrast, in astrocytes from Kir4.1 -/- mice the NH_4^+-induced depolarization (ΔE_M: 0.5 ± 0.1 mV, $n = 4$) was reduced to 9 ± 4 % ($p < 0.001$). Because of the highly depolarized membrane potential, clamping those astrocytes to E_H = -85 mV required holding currents in the 'nA' range, which made proper measurements of small currents upon NH_4^+ application almost impossible. Despite this, clamping to -50 mV required considerable smaller holding currents of maximal up to 200 pA. Thus, NH_4^+ caused an inward current (5 ± 1 pA, $n = 4$, $p = 0.005$), which was reduced to 6 ± 1 % compared to wild type ($p < 0.001$). These results clearly show that Kir4.1 mediated the NH_4^+-induced depolarization and current.

As the Ba^{2+} experiments already suggested, the NH_4^+-induced $[K^+]_o$ increase in the *stratum radiatum* obtained from Kir4.1 -/- mice ($\Delta[K^+]_o$: 0.78 ± 0.12 mM, $n = 6$) was not significantly different from that in their wild type littermates ($\Delta[K^+]_o$: 0.71 ± 0.09 mM, $n = 6$; $p = 0.305$) (Fig. 16*D*). The $[K^+]_o$ undershoot upon removal of NH_4^+ was also unchanged ($\Delta[K^+]_o$: Kir -/-: 0.76 ± 0.24 mM, $n = 6$; wild type: 1.08 ± 0.12 mM, $n = 6$; $p = 0.128$). These results confirm that Kir channels were not the source for the $[K^+]_o$ increase.

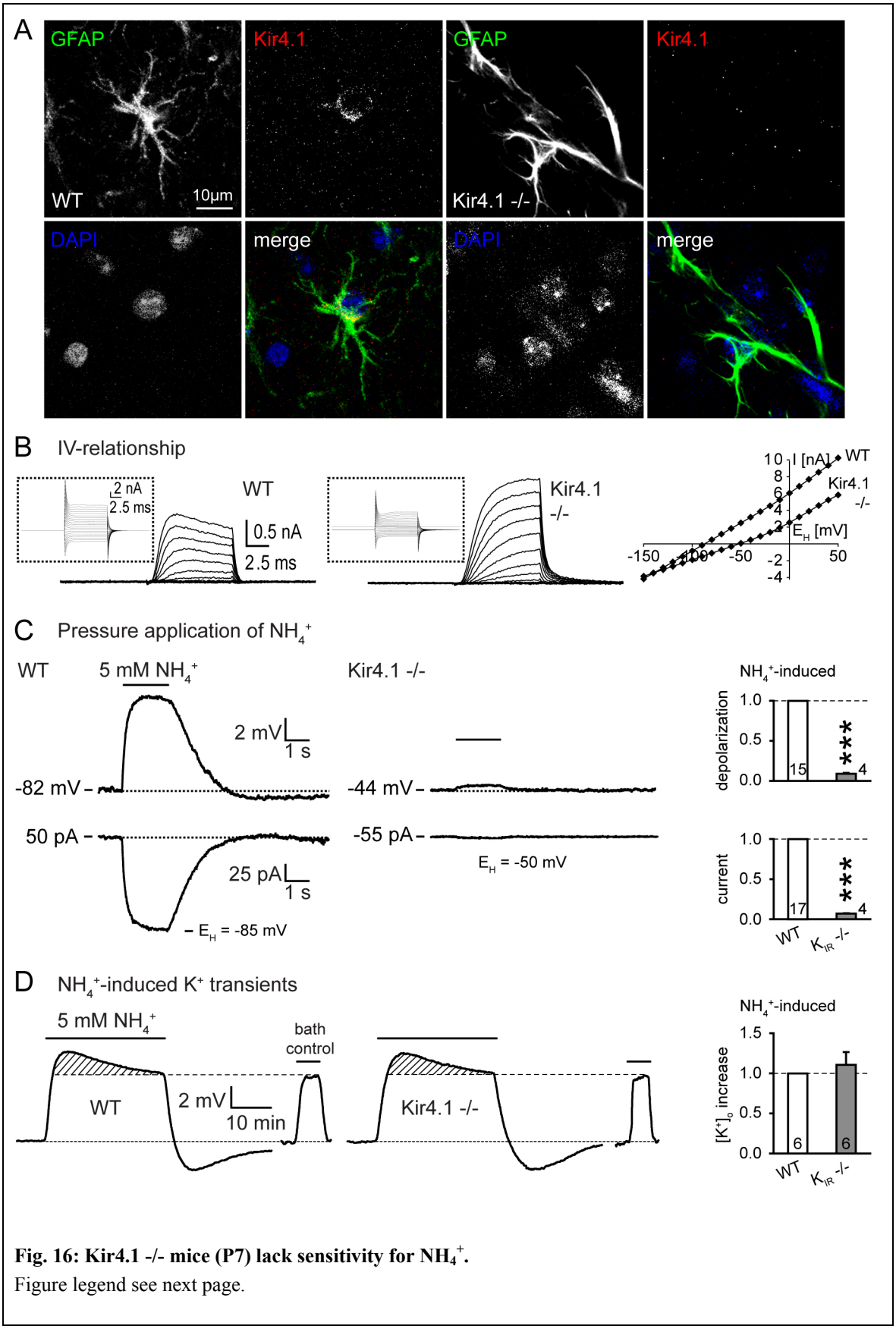

Fig. 16: Kir4.1 -/- mice (P7) lack sensitivity for NH_4^+.

Figure legend see next page.

Fig. 16: Kir4.1 -/- mice (P7) lack sensitivity for NH4+. Kir4.1 -/- mice (P7) lack sensitivity for NH_4^+. (A, B) Immunohistochemical and electrophysiological confirmation of genotype. (A) Co-labeling of GFAP and Kir4.1 showed a reduction in Kir4.1 immunoreactivity in GFAP-positive astrocytes of KO mice (right). (B) Astrocytes from KO mice were significantly depolarized and for clamping to -85 mV a huge holding current was necessary (middle; zero current indicated by the dashed line). Right: The IV-relationship of the respective astrocyte from KO mice showed slightly reduced current amplitudes at negative holding potentials (E_H) compared to that from WT. (C) Pressure application of NH_4^+ caused a depolarization (upper traces and diagram) and I_{NH4+} (lower traces and diagram) of astrocytes from wild type mice, but not in those from KO littermates. (D) The $[K^+]_o$ increase in the *stratum radiatum* from KO mice was unaffected compared to those from wild type mice. n-Values are contained within the bars.

3.8 K^+ uptake in astrocytes

The ability of astrocytes to take up elevated extracellular K^+ strongly depends on their highly negative E_M. The NH_4^+-induced depolarization of astrocytes, therefore likely impairs the K^+ uptake capability. To address this question, we consecutively clamped astrocytes to E_H = -85 and -75 mV to imitate the effect of NH_4^+ on the E_M and then pressure applied K^+. The shift of E_H to less negative values caused a significant reduction of the K^+-induced inward current by 16 ± 7 % (n = 5, p = 0.038) (Fig. 17*A*). This result supports the idea of an NH_4^+-induced impairment of K^+ uptake.

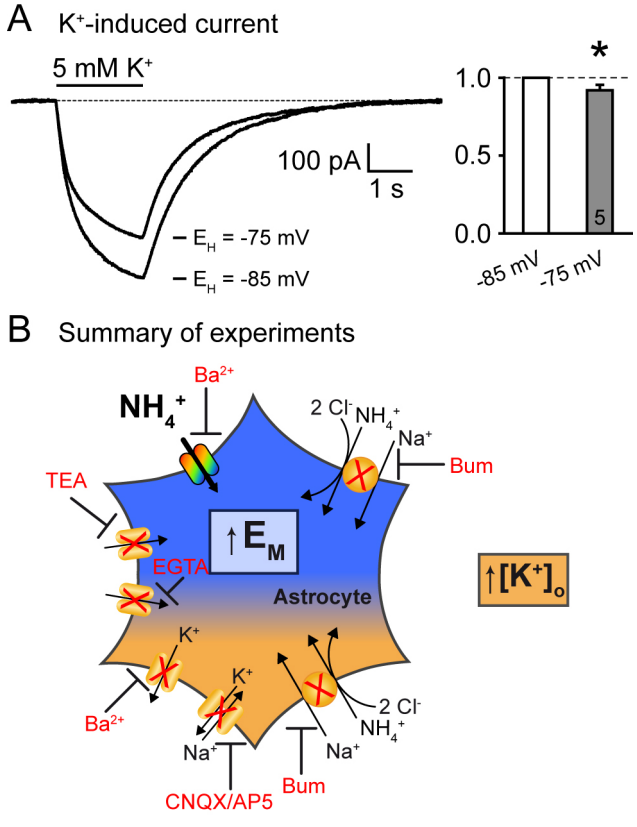

Fig. 17: K^+ uptake / Summary of results. (A) Left: Voltage-clamp measurement of an astrocyte at P18. Pressure application of K^+ caused an inward current that was reduced if E_H was shifted from -85 to -75 mV. Right: The normalized K^+-induced current was reduced by 16 %. *n*-Values are contained within the bars. (B) Scheme of an astrocyte showing pathways for I_{NH4+} entry (upper part) and $[K^+]_o$ increase (lower part). Crossed channels and transporters do not mediate the effects of NH_4^+. Kir channels mediate the NH_4^+-induced depolarization via an influx of NH_4^+. None of the investigated channels or transporters are involved in the $[K^+]_o$ increase.

Taken together, the results show that NH_4^+ causes a depolarization and inward current in hippocampal astrocytes as well as a $[K^+]_o$ increase. The data suggest that NH_4^+ can substitute for K^+ at respective channels. Additionally, the results show that the NH_4^+-induced depolarization of astrocytes depends on two mechanisms: First, influx of NH_4^+ through Kir4.1 channels, as experiments with Ba^{2+} and on Kir4.1 -/- mice revealed. Second, the NH_4^+-induced $[K^+]_o$ increase causing a further depolarization (Fig. 17*B*). The origin of the NH_4^+-induced $[K^+]_o$ increase remains unclear, as it was not affected by the utilized inhibitors.

4 Discussion

In this study we addressed the question, whether these NH_4^+-induced alterations of the electrophysiolgical properties of astrocytes and $[K^+]_o$ cause a disturbance of the K^+ homeostasis that in turn might have implications for the pathology of HE.

NH_4^+ causes a depolarization in a variety of cell types (Allert et al., 1998; Marcaggi et al., 2004; Kelly and Church, 2005). Whole-cell current-clamp recordings revealed that astrocytes depolarized in the presence of 5 mM NH_4^+ by about ~8 mV. $[K^+]_o$ measurements showed that $[K^+]_o$ increased by about 1 mM, which is in line with an earlier report (Marcaggi et al., 2004). The $[K^+]_o$ decrease in the presence of NH_4^+ and return to its basal level of 2.5 mM is presumably the reason for the initial NH_4^+-induced peak depolarization of astrocytes that is followed by a partial repolarization during ongoing perfusion with NH_4^+. The NH_4^+-induced depolarization of astrocytes exhibited a faster time course compared to the $[K^+]_o$ increase. Although the final $[NH_4^+]$ was achieved more slowly, the ultimate concentration deep in the tissue was the same as in the first cell layers (Benjamin et al., 1978). Therefore, the fact that the maximal depolarization is detected earlier than the peak $[K^+]_o$, is likely due to the penetration depth of the respective recording electrode.

4.1 Mechanism of the NH_4^+-induced depolarization of astrocytes

We addressed the question by which mechanism NH_4^+ causes the depolarization and inward current in astrocytes. The electroneutral NKCC, which transports K^+, Na^+ and 2 Cl^- into the cell, is also known to transport NH_4^+ instead of K^+ (Yan et al., 2001; Kelly et al., 2009; Kelly and Rose, 2010). It was speculated that the NH_4^+-induced depolarization could arise from a channel-mediated efflux of intracellularily accumulated Cl^- (Marcaggi et al., 1999). In our experiments, however, bumetanide had no effect on the NH_4^+-induced depolarization, thus excluding an involvement of the NKCC. Therefore, a different mechanism for the NH_4^+-induced depolarization had to be considered.

Astrocytes can be seen as a K^+ sensor. Regarding that NH_4^+ caused a $[K^+]_o$ increase, we determined the relationship between $[K^+]_o$ and astrocytic E_M. Depending on the experimental conditions it was found that cells in the CNS exhibit a relationship between $[K^+]_o$ and E_M that either showed Nernst behavior (Hodgkin and Horowicz, 1959; Orkand et al., 1966; Ransom and Goldring, 1973; Walz et al., 1984; Meeks and Mennerick, 2007) or GHK behavior (Kimelberg et al., 1979; Anderson et al., 1995). In this study, astrocytes from acute hippocampal slices exhibited a GHK behavior. As astrocytes predominantly show K^+ conductance (Walz et al., 1984) a close correlation between E_M and Eq5 was achieved, if the relative Na^+ permeability was adjusted at a low value of 0.015 (Fig. 13*B*).

In order to test, whether a $[K^+]_o$ increase of 1 mM is sufficient to cause a depolarization of about 8 mV in astrocytes at P18, we perfused the tissue with ACSF containing 3.5 mM K^+ instead of 2.5 mM. The half time of the K^+ induced depolarization was significantly shorter than that induced by NH_4^+. This is in line with a study on glial cells of the bee retina (Marcaggi et al., 2004). But it is likely that, at least in our experimental model, the process leading to an accumulation of K^+ in the extracellular space is slower than the wash-in of ACSF with increased $[K^+]$. Therefore, the shorter half time of the K^+-induced depolarization compared to that induced by NH_4^+ is only an initial hint that the $[K^+]_o$ increase is not the sole reason for the NH_4^+-induced depolarization of astrocytes. More pivotal is the fact that the K^+-induced depolarization was 39 % smaller than the NH_4^+-induced depolarization. Furthermore, while the NH_4^+-induced $[K^+]_o$ increase was abolished in less than 30 min, the astrocytes stayed depolarized in the presence of NH_4^+. Altogether, this clearly shows that the NH_4^+-induced depolarization is only partially due to the $[K^+]_o$ increase.

The question arises, whether the E_M of astrocytes under NH_4^+ conditions follows a distinct predictable mechanism. The depolarization induced by different $[NH_4^+]$ could not be fitted properly with a Michaelis-Menten equation, as it was described by others (Marcaggi et al., 2004), but with GHK equation assuming a relative NH_4^+ permeability of 0.33 and taking into account the measured $[NH_4^+]$ dependent $[K^+]_o$ increase (Fig. 13*C*). This supports the idea that NH_4^+ can penetrate the cell membrane, enters the cell via K^+ channels and hence contributes to the depolarization of the astrocytes.

4.2 Kir4.1 channels mediate the NH_4^+ influx

We next addressed the question regarding the molecular basis mediating the influx of NH_4^+ into the astrocytes. The NH_4^+-induced depolarization and inward current increased during the early postnatal development. This is likely due to an increased K^+ channel expression in astrocytes, as e.g. Kir4.1 channels are upregulated during the early postnatal development (Seifert et al., 2009). The Kir channel blocker Ba^{2+} reduced both the NH_4^+-induced depolarization as well as I_{NH4+} by 50 - 75 %, depending on the developmental stage. The remaining depolarization and membrane current were likely caused by the $[K^+]_o$ increase that was unaffected by Ba^{2+} or genetic inactivation of Kir4.1 and thus independent from Kir channels. In addition, pressure application of NH_4^+ led to a strongly reduced depolarization and change in membrane current of astrocytes from Kir4.1 -/- mice, clearly showing that Kir4.1 channels resemble the molecular basis. The remaining small NH_4^+-induced depolarization and inward current is likely due to entry of NH_4^+ into astrocytes through two pore domain channels (K_{2P}), which resemble a smaller fraction of K^+ channels in astrocytes (Seifert et al., 2009).

It is discussed, whether a NH_4^+ influx through Kir channels contributes to the NH_4^+-induced acidification (Nagaraja and Brookes, 1998; Titz et al., 2006; Kelly and Rose, 2010). It can be argued that the depolarizing effect of NH_4^+ is rather due to an inhibition of Kir channels mimicking Ba^{2+}. This seems to be unlikely, because both, NH_4^+ and Ba^{2+}, showed at different developmental stages a different degree of impact regarding the membrane depolarization. While the NH_4^+-induced depolarization at P7 and P18 was similar, the depolarizing effect of Ba^{2+} was about 2.5 fold augmented at P7. Furthermore, the effect of NH_4^+ and Ba^{2+} on R_M was contrary. While NH_4^+ caused even in the presence of Ba^{2+} a decrease of R_M, Ba^{2+} led to an increase by lowering Kir channel conductance. Finally, while Ba^{2+} caused an alteration of the IV-relationship by reducing current amplitude at negative potentials, NH_4^+ did not. Therefore, and because of the predictable contribution to astrocytic E_M following the GHK equation, it is more likely that NH_4^+ enters astrocytes through Kir channels.

4.3 Origin of the NH_4^+-induced $[K^+]_o$ increase

The NH_4^+-induced $[K^+]_o$ increase may either result from an enhanced K^+ release or a reduced K^+ uptake. As we excluded K^+ release during neuronal activity, synaptic transmission, or from Kir channels, a mechanism containing a reduced K^+ uptake capability becomes more likely. If NH_4^+ is competing with K^+ at channels, transporters, or pumps and by that causes an $[K^+]_o$ increase, specific inhibitors must cause an increase in baseline $[K^+]_o$ that is followed by no or reduced further K^+ accumulation upon application of NH_4^+. Experiments with bumetanide, Ba^{2+} or on Kir -/- mice, did not affect either baseline $[K^+]_o$ or the NH_4^+-induced $[K^+]_o$ increase, indicating its independence from NKCC and Kir channels. The Na^+, K^+-ATPase inhibitor ouabain itself caused a multi-phase $[K^+]_o$ elevation without achieving a steady-state in an appropriate time (data not shown), so that under those conditions measurements of NH_4^+-induced $[K^+]_o$ increase are difficult to evaluate. It was shown before, that NH_4^+ enters astrocytes via the Na^+, K^+-ATPase causing an acidic shift (Kelly and Rose, 2010). NH_4^+ probably replaces K^+ at the Na^+, K^+-ATPase and therefore causes less K^+ uptake resulting in a $[K^+]_o$ increase. Additionally, upon removal of NH_4^+ the $[K^+]_o$ decrease below baseline is likely due to an intensified Na^+, K^+-ATPase activity further indicating the relevance of the pump for the $[K^+]_o$ alterations during and after hyperammonemic conditions.

4.4 Impairment of K^+ homeostasis - Implications for the pathology of HE

The question arises, whether the NH_4^+-induced depolarization of astrocytes impairs their function and therefore might contribute to the pathology of HE. In fact, pressure application of K^+ showed that the K^+-induced inward current in astrocytes became smaller when the membrane potential was shifted into positive direction, suggesting a reduced K^+ uptake. This in turn would cause increased and prolonged elevations of extracellular K^+ due to K^+ efflux and hence lead to an increased neuronal excitability (Voskuyl and ter Keurs, 1981; Balestrino et al., 1986; Kreisman and Smith, 1993; Walz, 2000). This hypothesis is supported by the fact that NH_4^+ causes an increased spiking frequency of hippocampal pyramidal neurons (Kelly and Church, 2005).

Under hyperammonemic conditions, astrocytes exhibit an acidification and a bumetanide sensitive $[Na^+]_i$ increase that reduces the uptake of extracellular glutamate (Kelly et al., 2009). As the respective transporter is electrogen (Danbolt, 2001), glutamate uptake is additionally linked to the electrical gradient. Therefore, the NH_4^+-induced depolarization of astrocytes will further reduce the clearance of glutamate. Finally, the increased extracellular glutamate concentration can result in neurotoxicity by increasing NMDA receptor-mediated Ca^{2+} influx into neurons (Marcaida et al., 1992; Monfort et al., 2002; Rodrigo et al., 2009; Lau and Tymianski, 2010). In chronic HE the glutamate uptake is additionally reduced by the downregulation of corresponding transporters further enhancing the pathology of HE (Knecht et al., 1997; Chan and Butterworth, 1999; Chan et al., 2000).

Altogether, our results show that the NH_4^+-induced depolarization of astrocytes as well as the $[K^+]_o$ increase reflect an impairment of K^+ homeostasis. This may cause an increased neuronal excitability and reduced glutamate uptake by astrocytes, which in turn is part of the pathology of HE.

5 References

Alger BE, Nicoll RA (1983) Ammonia does not selectively block IPSPs in rat hippocampal pyramidal cells. J Neurophysiol 49:1381-1391.

Allert N, Koller H, Siebler M (1998) Ammonia-induced depolarization of cultured rat cortical astrocytes. Brain Res 782:261-270.

Andersen P, Morris R, Amaral DG, Bliss T, O'Keefe J (2007) The Hippocampus Book. Oxford University Press.

Anderson S, Brismar T, Hansson E (1995) Effect of external K+, Ca2+, and Ba2+ on membrane potential and ionic conductance in rat astrocytes. Cell Mol Neurobiol 15:439-450.

Araque A, Parpura V, Sanzgiri RP, Haydon PG (1999) Tripartite synapses: glia, the unacknowledged partner. Trends Neurosci 22:208-215.

Balestrino M, Aitken PG, Somjen GG (1986) The effects of moderate changes of extracellular K+ and Ca2+ on synaptic and neural function in the CA1 region of the hippocampal slice. Brain Res 377:229-239.

Baumann N, Pham-Dinh D (2001) Biology of oligodendrocyte and myelin in the mammalian central nervous system. Physiol Rev 81:871-927.

Benjamin AM, Okamoto K, Quastel JH (1978) Effects of ammonium ions on spontaneous action potentials and on contents of sodium, potassium, ammonium and chloride ions in brain in vitro. J Neurochem 30:131-143.

Bergeron MJ, Gagnon E, Wallendorff B, Lapointe JY, Isenring P (2003) Ammonium transport and pH regulation by K(+)-Cl(-) cotransporters. Am J Physiol Renal Physiol 285:F68-78.

Blei AT, Olafsson S, Therrien G, Butterworth RF (1994) Ammonia-induced brain edema and intracranial hypertension in rats after portacaval anastomosis. Hepatology 19:1437-1444.

Blomstrand F, Venance L, Siren AL, Ezan P, Hanse E, Glowinski J, Ehrenreich H, Giaume C (2004) Endothelins regulate astrocyte gap junctions in rat hippocampal slices. Eur J Neurosci 19:1005-1015.

Bordey A, Sontheimer H (1997) Postnatal development of ionic currents in rat hippocampal astrocytes in situ. J Neurophysiol 78:461-477.

Bordey A, Sontheimer H (2000) Ion channel expression by astrocytes in situ: comparison of different CNS regions. Glia 30:27-38.

Bunge RP (1968) Glial cells and the central myelin sheath. Physiol Rev 48:197-251.

Butterworth RF, Norenberg MD, Felipo V, Ferenci P, Albrecht J, Blei AT (2009) Experimental models of hepatic encephalopathy: ISHEN guidelines. Liver Int 29:783-788.

Capocaccia L, Angelico M (1991) Fulminant hepatic failure. Clinical features, etiology, epidemiology, and current management. Dig Dis Sci 36:775-779.

Chan H, Butterworth RF (1999) Evidence for an astrocytic glutamate transporter deficit in hepatic encephalopathy. Neurochem Res 24:1397-1401.

Chan H, Hazell AS, Desjardins P, Butterworth RF (2000) Effects of ammonia on glutamate transporter (GLAST) protein and mRNA in cultured rat cortical astrocytes. Neurochem Int 37:243-248.

Clemmesen JO, Larsen FS, Kondrup J, Hansen BA, Ott P (1999) Cerebral herniation in patients with acute liver failure is correlated with arterial ammonia concentration. Hepatology 29:648-653.

Cooper AJ, Plum F (1987) Biochemistry and physiology of brain ammonia. Physiol Rev 67:440-519.

D'Ambrosio R, Wenzel J, Schwartzkroin PA, McKhann GM, 2nd, Janigro D (1998) Functional specialization and topographic segregation of hippocampal astrocytes. J Neurosci 18:4425-4438.

Danbolt NC (2001) Glutamate uptake. Prog Neurobiol 65:1-105.

de Knegt RJ, Schalm SW, van der Rijt CC, Fekkes D, Dalm E, Hekking-Weyma I (1994) Extracellular brain glutamate during acute liver failure and during acute hyperammonemia simulating acute liver failure: an experimental study based on in vivo brain dialysis. J Hepatol 20:19-26.

Dheen ST AH, YK Ng and EA Ling (2002) Regulatory factors and functions of microglia during development. Neuroembryology 1 3:105-112.

Eng LF, Ghirnikar RS, Lee YL (2000) Glial fibrillary acidic protein: GFAP-thirty-one years (1969-2000). Neurochem Res 25:1439-1451.

Eulenburg V, Gomeza J (2010) Neurotransmitter transporters expressed in glial cells as regulators of synapse function. Brain Res Rev 63:103-112.

Farber K, Kettenmann H (2005) Physiology of microglial cells. Brain Res Brain Res Rev 48:133-143.

Felipo V, Butterworth RF (2002) Neurobiology of ammonia. Prog Neurobiol 67:259-279.

Ferenci P, Lockwood A, Mullen K, Tarter R, Weissenborn K, Blei AT (2002) Hepatic encephalopathy--definition, nomenclature, diagnosis, and quantification: final report of the working party at the 11th World Congresses of Gastroenterology, Vienna, 1998. Hepatology 35:716-721.

Ganz R, Swain M, Traber P, DalCanto M, Butterworth RF, Blei AT (1989) Ammonia-induced swelling of rat cerebral cortical slices: implications for the pathogenesis of brain edema in acute hepatic failure. Metab Brain Dis 4:213-223.

Giaume C, Theis M (2010) Pharmacological and genetic approaches to study connexin-mediated channels in glial cells of the central nervous system. Brain Res Rev 63:160-176.

Halassa MM, Fellin T, Haydon PG (2009) Tripartite synapses: roles for astrocytic purines in the control of synaptic physiology and behavior. Neuropharmacology 57:343-346.

Hawkins RA, O'Kane RL, Simpson IA, Vina JR (2006) Structure of the blood-brain barrier and its role in the transport of amino acids. J Nutr 136:218S-226S.

Haydon PG (2001) GLIA: listening and talking to the synapse. Nat Rev Neurosci 2:185-193.

Haydon PG, Carmignoto G (2006) Astrocyte control of synaptic transmission and neurovascular coupling. Physiol Rev 86:1009-1031.

Hille B (1973) Potassium channels in myelinated nerve. Selective permeability to small cations. J Gen Physiol 61:669-686.

Hodgkin AL, Horowicz P (1959) The influence of potassium and chloride ions on the membrane potential of single muscle fibres. J Physiol 148:127-160.

Holthoff K, Witte OW (2000) Directed spatial potassium redistribution in rat neocortex. Glia 29:288-292.

Honsek SD, Walz C, Kafitz KW, Rose CR (2010) Astrocyte calcium signals at Schaffer collateral to CA1 pyramidal cell synapses correlate with the number of activated synapses but not with synaptic strength. Hippocampus.

Houades V, Koulakoff A, Ezan P, Seif I, Giaume C (2008) Gap junction-mediated astrocytic networks in the mouse barrel cortex. J Neurosci 28:5207-5217.

Jayakumar AR, Rama Rao KV, Schousboe A, Norenberg MD (2004) Glutamine-induced free radical production in cultured astrocytes. Glia 46:296-301.

Jayakumar AR, Rao KV, Murthy Ch R, Norenberg MD (2006) Glutamine in the mechanism of ammonia-induced astrocyte swelling. Neurochem Int 48:623-628.

Jayakumar AR, Liu M, Moriyama M, Ramakrishnan R, Forbush B, 3rd, Reddy PV, Norenberg MD (2008) Na-K-Cl Cotransporter-1 in the mechanism of ammonia-induced astrocyte swelling. J Biol Chem 283:33874-33882.

Kafitz KW, Meier SD, Stephan J, Rose CR (2008) Developmental profile and properties of sulforhodamine 101--Labeled glial cells in acute brain slices of rat hippocampus. J Neurosci Methods 169:84-92.

Kang J, Jiang L, Goldman SA, Nedergaard M (1998) Astrocyte-mediated potentiation of inhibitory synaptic transmission. Nat Neurosci 1:683-692.

Kelly T, Church J (2005) The weak bases NH(3) and trimethylamine inhibit the medium and slow afterhyperpolarizations in rat CA1 pyramidal neurons. Pflugers Arch 451:418-427.

Kelly T, Rose CR (2010) Ammonium influx pathways into astrocytes and neurones of hippocampal slices. J Neurochem 115:1123-1136.

Kelly T, Kafitz KW, Roderigo C, Rose CR (2009) Ammonium-evoked alterations in intracellular sodium and pH reduce glial glutamate transport activity. Glia 57:921-934.

Kimelberg HK (2004) The problem of astrocyte identity. Neurochem Int 45:191-202.

Kimelberg HK, Bowman C, Biddlecome S, Bourke RS (1979) Cation transport and membrane potential properties of primary astroglial cultures from neonatal rat brains. Brain Res 177:533-550.

Knecht K, Michalak A, Rose C, Rothstein JD, Butterworth RF (1997) Decreased glutamate transporter (GLT-1) expression in frontal cortex of rats with acute liver failure. Neurosci Lett 229:201-203.

Kofuji P, Newman EA (2004) Potassium buffering in the central nervous system. Neuroscience 129:1045-1056.

Kofuji P, Ceelen P, Zahs KR, Surbeck LW, Lester HA, Newman EA (2000) Genetic inactivation of an inwardly rectifying potassium channel (Kir4.1 subunit) in mice: phenotypic impact in retina. J Neurosci 20:5733-5740.

Konietzko U, Muller CM (1994) Astrocytic dye coupling in rat hippocampus: topography, developmental onset, and modulation by protein kinase C. Hippocampus 4:297-306.

Kosenko E, Kaminsky YG, Felipo V, Minana MD, Grisolia S (1993) Chronic hyperammonemia prevents changes in brain energy and ammonia metabolites induced by acute ammonium intoxication. Biochim Biophys Acta 1180:321-326.

Kreisman NR, Smith ML (1993) Potassium-induced changes in excitability in the hippocampal CA1 region of immature and adult rats. Brain Res Dev Brain Res 76:67-73.

Kressin K, Kuprijanova E, Jabs R, Seifert G, Steinhauser C (1995) Developmental regulation of Na+ and K+ conductances in glial cells of mouse hippocampal brain slices. Glia 15:173-187.

Kucheryavykh YV, Kucheryavykh LY, Nichols CG, Maldonado HM, Baksi K, Reichenbach A, Skatchkov SN, Eaton MJ (2007) Downregulation of Kir4.1 inward rectifying potassium channel subunits by RNAi impairs potassium transfer and glutamate uptake by cultured cortical astrocytes. Glia 55:274-281.

Kuchler-Bopp S, Delaunoy JP, Artault JC, Zaepfel M, Dietrich JB (1999) Astrocytes induce several blood-brain barrier properties in non-neural endothelial cells. Neuroreport 10:1347-1353.

Latorre R, Miller C (1983) Conduction and selectivity in potassium channels. J Membr Biol 71:11-30.

Lau A, Tymianski M (2010) Glutamate receptors, neurotoxicity and neurodegeneration. Pflugers Arch 460:525-542.

Lavoie J, Giguere JF, Layrargues GP, Butterworth RF (1987) Amino acid changes in autopsied brain tissue from cirrhotic patients with hepatic encephalopathy. J Neurochem 49:692-697.

Lee Y, Su M, Messing A, Brenner M (2006) Astrocyte heterogeneity revealed by expression of a GFAP-LacZ transgene. Glia 53:677-687.

Marcaggi P, Coles JA (2001) Ammonium in nervous tissue: transport across cell membranes, fluxes from neurons to glial cells, and role in signalling. Prog Neurobiol 64:157-183.

Marcaggi P, Jeanne M, Coles JA (2004) Neuron-glial trafficking of NH4+ and K+: separate routes of uptake into glial cells of bee retina. Eur J Neurosci 19:966-976.

Marcaggi P, Thwaites DT, Deitmer JW, Coles JA (1999) Chloride-dependent transport of NH4+ into bee retinal glial cells. Eur J Neurosci 11:167-177.

Marcaida G, Felipo V, Hermenegildo C, Minana MD, Grisolia S (1992) Acute ammonia toxicity is mediated by the NMDA type of glutamate receptors. FEBS Lett 296:67-68.

Meeks JP, Mennerick S (2007) Astrocyte membrane responses and potassium accumulation during neuronal activity. Hippocampus 17:1100-1108.

Meier SD, Kovalchuk Y, Rose CR (2006) Properties of the new fluorescent Na+ indicator CoroNa Green: comparison with SBFI and confocal Na+ imaging. J Neurosci Methods 155:251-259.

Metea MR, Newman EA (2006) Glial cells dilate and constrict blood vessels: a mechanism of neurovascular coupling. J Neurosci 26:2862-2870.

Michalak A, Rose C, Butterworth J, Butterworth RF (1996) Neuroactive amino acids and glutamate (NMDA) receptors in frontal cortex of rats with experimental acute liver failure. Hepatology 24:908-913.

Monfort P, Kosenko E, Erceg S, Canales JJ, Felipo V (2002) Molecular mechanism of acute ammonia toxicity: role of NMDA receptors. Neurochem Int 41:95-102.

Mulligan SJ, MacVicar BA (2004) Calcium transients in astrocyte endfeet cause cerebrovascular constrictions. Nature 431:195-199.

Nagaraja TN, Brookes N (1998) Intracellular acidification induced by passive and active transport of ammonium ions in astrocytes. Am J Physiol 274:C883-891.

Neumann S, Dierkes PW, Schlue WR (2001) Potentiometric measurement of cell volume changes and intracellular ion concentrations in leech Retzius neurones. J Electrochim 47:309-317.

Neusch C, Papadopoulos N, Muller M, Maletzki I, Winter SM, Hirrlinger J, Handschuh M, Bahr M, Richter DW, Kirchhoff F, Hulsmann S (2006) Lack of the Kir4.1 channel subunit abolishes K+ buffering properties of astrocytes in the ventral respiratory group: impact on extracellular K+ regulation. J Neurophysiol 95:1843-1852.

Newman EA, Volterra A (2004) Glial control of synaptic function. Glia 47:207-208.

Nimmerjahn A, Kirchhoff F, Kerr JN, Helmchen F (2004) Sulforhodamine 101 as a specific marker of astroglia in the neocortex in vivo. Nat Methods 1:31-37.

Nolte C, Matyash M, Pivneva T, Schipke CG, Ohlemeyer C, Hanisch UK, Kirchhoff F, Kettenmann H (2001) GFAP promoter-controlled EGFP-expressing transgenic mice: a tool to visualize astrocytes and astrogliosis in living brain tissue. Glia 33:72-86.

Norenberg MD, Jayakumar AR, Rama Rao KV, Panickar KS (2007) New concepts in the mechanism of ammonia-induced astrocyte swelling. Metab Brain Dis 22:219-234.

Orkand RK, Nicholls JG, Kuffler SW (1966) Effect of nerve impulses on the membrane potential of glial cells in the central nervous system of amphibia. J Neurophysiol 29:788-806.

Ott P, Larsen FS (2004) Blood-brain barrier permeability to ammonia in liver failure: a critical reappraisal. Neurochem Int 44:185-198.

Pekny M, Stanness KA, Eliasson C, Betsholtz C, Janigro D (1998) Impaired induction of blood-brain barrier properties in aortic endothelial cells by astrocytes from GFAP-deficient mice. Glia 22:390-400.

Pekny M, Leveen P, Pekna M, Eliasson C, Berthold CH, Westermark B, Betsholtz C (1995) Mice lacking glial fibrillary acidic protein display astrocytes devoid of intermediate filaments but develop and reproduce normally. Embo J 14:1590-1598.

Perea G, Araque A (2010) GLIA modulates synaptic transmission. Brain Res Rev 63:93-102.

Rama Rao KV, Norenberg MD (2001) Cerebral energy metabolism in hepatic encephalopathy and hyperammonemia. Metab Brain Dis 16:67-78.

Rama Rao KV, Jayakumar AR, Norenberg MD (2005) Differential response of glutamine in cultured neurons and astrocytes. J Neurosci Res 79:193-199.

Ransom BR, Goldring S (1973) Slow depolarization in cells presumed to be glia in cerebral cortex of cat. J Neurophysiol 36:869-878.

Ransom CB, Sontheimer H (1995) Biophysical and pharmacological characterization of inwardly rectifying K+ currents in rat spinal cord astrocytes. J Neurophysiol 73:333-346.

Raponi E, Agenes F, Delphin C, Assard N, Baudier J, Legraverend C, Deloulme JC (2007) S100B expression defines a state in which GFAP-expressing cells lose their neural stem cell potential and acquire a more mature developmental stage. Glia 55:165-177.

Ratnakumari L, Qureshi IA, Butterworth RF (1994) Regional amino acid neurotransmitter changes in brains of spf/Y mice with congenital ornithine transcarbamylase deficiency. Metab Brain Dis 9:43-51.

Rodrigo R, Cauli O, Boix J, ElMlili N, Agusti A, Felipo V (2009) Role of NMDA receptors in acute liver failure and ammonia toxicity: therapeutical implications. Neurochem Int 55:113-118.

Rose C (2002) Increased extracellular brain glutamate in acute liver failure: decreased uptake or increased release? Metab Brain Dis 17:251-261.

Rose C (2006) Effect of ammonia on astrocytic glutamate uptake/release mechanisms. J Neurochem 97 Suppl 1:11-15.

Schiodt FV, Atillasoy E, Shakil AO, Schiff ER, Caldwell C, Kowdley KV, Stribling R, Crippin JS, Flamm S, Somberg KA, Rosen H, McCashland TM, Hay JE, Lee WM (1999) Etiology and outcome for 295 patients with acute liver failure in the United States. Liver Transpl Surg 5:29-34.

Schools GP, Zhou M, Kimelberg HK (2006) Development of gap junctions in hippocampal astrocytes: evidence that whole cell electrophysiological phenotype is an intrinsic property of the individual cell. J Neurophysiol 96:1383-1392.

Seifert G, Schilling K, Steinhauser C (2006) Astrocyte dysfunction in neurological disorders: a molecular perspective. Nat Rev Neurosci 7:194-206.

Seifert G, Huttmann K, Binder DK, Hartmann C, Wyczynski A, Neusch C, Steinhauser C (2009) Analysis of astroglial K+ channel expression in the developing hippocampus reveals a predominant role of the Kir4.1 subunit. J Neurosci 29:7474-7488.

Sontheimer H, Waxman SG (1993) Expression of voltage-activated ion channels by astrocytes and oligodendrocytes in the hippocampal slice. J Neurophysiol 70:1863-1873.

Steinhauser C, Berger T, Frotscher M, Kettenmann H (1992) Heterogeneity in the Membrane Current Pattern of Identified Glial Cells in the Hippocampal Slice. Eur J Neurosci 4:472-484.

Stichel CC, Muller CM, Zilles K (1991) Distribution of glial fibrillary acidic protein and vimentin immunoreactivity during rat visual cortex development. J Neurocytol 20:97-108.

Swain M, Butterworth RF, Blei AT (1992a) Ammonia and related amino acids in the pathogenesis of brain edema in acute ischemic liver failure in rats. Hepatology 15:449-453.

Swain MS, Bergeron M, Audet R, Blei AT, Butterworth RF (1992b) Monitoring of neurotransmitter amino acids by means of an indwelling cisterna magna catheter: a comparison of two rodent models of fulminant liver failure. Hepatology 16:1028-1035.

Takahashi H, Koehler RC, Brusilow SW, Traystman RJ (1991) Inhibition of brain glutamine accumulation prevents cerebral edema in hyperammonemic rats. Am J Physiol 261:H825-829.

Takano T, Tian GF, Peng W, Lou N, Libionka W, Han X, Nedergaard M (2006) Astrocyte-mediated control of cerebral blood flow. Nat Neurosci 9:260-267.

Tanigami H, Rebel A, Martin LJ, Chen TY, Brusilow SW, Traystman RJ, Koehler RC (2005) Effect of glutamine synthetase inhibition on astrocyte swelling and altered astroglial protein expression during hyperammonemia in rats. Neuroscience 131:437-449.

Titz S, Hormuzdi S, Lewen A, Monyer H, Misgeld U (2006) Intracellular acidification in neurons induced by ammonium depends on KCC2 function. Eur J Neurosci 23:454-464.

Ullian EM, Christopherson KS, Barres BA (2004) Role for glia in synaptogenesis. Glia 47:209-216.

Volterra A, Meldolesi J (2005) Astrocytes, from brain glue to communication elements: the revolution continues. Nat Rev Neurosci 6:626-640.

Voorhies TM, Ehrlich ME, Duffy TE, Petito CK, Plum F (1983) Acute hyperammonemia in the young primate: physiologic and neuropathologic correlates. Pediatr Res 17:970-975.

Voskuyl RA, ter Keurs HE (1981) Modification of neuronal activity in olfactory cortex slices by extracellular K+. Brain Res 230:372-377.

Voutsinos-Porche B, Bonvento G, Tanaka K, Steiner P, Welker E, Chatton JY, Magistretti PJ, Pellerin L (2003) Glial glutamate transporters mediate a functional metabolic crosstalk between neurons and astrocytes in the mouse developing cortex. Neuron 37:275-286.

Wallraff A, Odermatt B, Willecke K, Steinhauser C (2004) Distinct types of astroglial cells in the hippocampus differ in gap junction coupling. Glia 48:36-43.

Wallraff A, Kohling R, Heinemann U, Theis M, Willecke K, Steinhauser C (2006) The impact of astrocytic gap junctional coupling on potassium buffering in the hippocampus. J Neurosci 26:5438-5447.

Walz W (2000) Role of astrocytes in the clearance of excess extracellular potassium. Neurochem Int 36:291-300.

Walz W, Wuttke W, Hertz L (1984) Astrocytes in primary cultures: membrane potential characteristics reveal exclusive potassium conductance and potassium accumulator properties. Brain Res 292:367-374.

Watanabe A, Takei N, Higashi T, Shiota T, Nakatsukasa H, Fujiwara M, Sakata T, Nagashima H (1984) Glutamic acid and glutamine levels in serum and cerebrospinal fluid in hepatic encephalopathy. Biochem Med 32:225-231.

Willard-Mack CL, Koehler RC, Hirata T, Cork LC, Takahashi H, Traystman RJ, Brusilow SW (1996) Inhibition of glutamine synthetase reduces ammonia-induced astrocyte swelling in rat. Neuroscience 71:589-599.

Xu G, Wang W, Kimelberg HK, Zhou M (2010) Electrical coupling of astrocytes in rat hippocampal slices under physiological and simulated ischemic conditions. Glia 58:481-493.

Yan Y, Dempsey RJ, Sun D (2001) Expression of Na(+)-K(+)-Cl(-) cotransporter in rat brain during development and its localization in mature astrocytes. Brain Res 911:43-55.

Zhou M, Schools GP, Kimelberg HK (2006) Development of GLAST(+) astrocytes and NG2(+) glia in rat hippocampus CA1: mature astrocytes are electrophysiologically passive. J Neurophysiol 95:134-143.

Zhou M, Xu G, Xie M, Zhang X, Schools GP, Ma L, Kimelberg HK, Chen H (2009) TWIK-1 and TREK-1 are potassium channels contributing significantly to astrocyte passive conductance in rat hippocampal slices. J Neurosci 29:8551-8564.

Zhuo L, Sun B, Zhang CL, Fine A, Chiu SY, Messing A (1997) Live astrocytes visualized by green fluorescent protein in transgenic mice. Dev Biol 187:36-42.

Zonta M, Angulo MC, Gobbo S, Rosengarten B, Hossmann KA, Pozzan T, Carmignoto G (2003) Neuron-to-astrocyte signaling is central to the dynamic control of brain microcirculation. Nat Neurosci 6:43-50.

Zwingmann C, Chatauret N, Rose C, Leibfritz D, Butterworth RF (2004) Selective alterations of brain osmolytes in acute liver failure: protective effect of mild hypothermia. Brain Res 999:118-123.

Appendix

A Supplementary data

A.1 Basic electrophysiological properties of astrocytes

Mouse line	Genotype	Age [pnd]	Membrane potential [mV]	Membrane resistance [MΩ]	Membrane capacitance [pF]	nPG	PG	n
Balb/c		P3	-84.6 ± 0.7	49 ± 6[b]	42 ± 2	94%	6%	59
		P7	-85.8 ± 0.3	19 ± 2[b]	62 ± 3	80%	20%	71
		P13	-86.3 ± 0.3	5 ± 1[b]	56 ± 4	17%	83%	69
		P18	-84.9 ± 0.2	3 ± 0[b]	43 ± 2	1%	99%	231
C57Bl6	WT	P7	-84.3 ± 0.6	26 ± 3	61 ± 4	83%	17%	46
	Kir4.1 -/-	P7	-51.4 ± 1.1[a]	20 ± 3	58 ± 3	91%	9%	34

Supplementary Table 1: Membrane properties of SR101-positive cells during early postnatal development.

a: significantly increased compared to WT.

b: significantly decreased compared to younger group.

A.2 Relative membrane permeability

The relationship between $[K^+]_o$ and astrocytic E_M did not correlate with Nernst equation:

$$E_K = \frac{R*T}{F} * \ln\left(\frac{[K^+]_o}{[K^+]_i}\right) \quad (4),$$

but could be well described with the Goldman-Hodgkin-Katz (GHK) equation:

$$E_M = \frac{R*T}{F} * \ln\left(\frac{\alpha[Na^+]_o + [K^+]_o}{\alpha[Na^+]_i + [K^+]_i}\right) \quad (5),$$

adjusting the relative Na^+ permeability $\left(\alpha = P_{Na}/P_K\right)$ to 0.015. *R*, *T* and *F* represent the gas constant, the absolute temperature and the Faraday constant. 'o' and 'i' refer to ion concentrations in the ACSF and, respectively, intracellular solution. The Measured E_M did not follow a relationship based on a Michaelis-Menten equation, but on a GHK equation:

$$E_M = \frac{R*T}{F} * \ln\left(\frac{\alpha[Na^+]_o + [K^+]_o + \beta[NH_4^+]_o}{\alpha[Na^+]_i + [K^+]_i + \beta[NH_4^+]_i}\right) \quad (6),$$

which includes a relative NH_4^+ permeability $\left(\beta = P_{NH4}/P_K\right)$ of 0.33, α from Eq5, and the measured $[NH_4^+]$ dependent peak $[K^+]_o$, respectively. The $[NH_4^+]_i$ was set to 0, as the intracellular solution diluted entering NH_4^+.

A.3 NH_4^+-induced alterations of astrocytic E_M and $[K^+]_o$

Age [pnd]	$[NH_4^+]$	ΔE_M [mV]	n	ΔR_M [MΩ]	n	I_{NH4+} [pA]	n
P3	5	5.6 ± 0.6	19	30.3 ± 6.7	4	118 ± 32	8
P7	5	7.3 ± 0.4[a]	20	3.6 ± 0.8	7	242 ± 33[a]	10
P13	5	7.7 ± 0.4	23	2.5 ± 0.5	14	395 ± 42[a]	21
P18	1	2.4 ± 0.3	8				
	5	8.5 ± 0.3[b]	52	2.2 ± 0.4	9	408 ± 73	9
	10	13.9 ± 0.4[b]	15				
	20	31.8 ± 3.6[b]	7				

Supplementary Table 2: NH_4^+-induced changes in astrocytic membrane properties.

a: significantly increased compared to younger group.

b: significantly increased compared to lower concentration.

ΔR_M values were not tested for significance against each other, because of the developmental dependent decrease of resting R_M.

Age [pnd]	$[NH_4^+]$	$\Delta[K^+]_o\uparrow$ [mM]	$\Delta[K^+]_o\downarrow$ [mM]	n
P3	5	0.39 ± 0.02	0.56 ± 0.13	5
P18	0.5	0.00 ± 0.00[x]	0.00 ± 0.00[x]	2
	1	0.20 ± 0.07[b]	0.07 ± 0.03[x]	4
	2.5	0.38 ± 0.11[b]	0.34 ± 0.12[b]	4
	5	1.07 ± 0.06[ab]	0.75 ± 0.05[b]	50
	10	1.50 ± 0.23[b]	0.98 ± 0.19[b]	5
	20	3.75 ± 1.03[b]	1.23 ± 0.41[b]	7

Supplementary Table 3: NH_4^+-induced changes in $[K^+]_o$.

a: significantly increased compared to younger group.

b: significantly increased compared to lower concentration.

x: not significantly different from base line.

Inhibitor	Age [pnd]	ΔE_M [%]	n	I_{NH4+} [%]	n	$\Delta[K^+]_o\uparrow$ [%]	n
Ba^{2+}	P7	50 ± 6[a]	7	38 ± 9[a]	5		
	P13			23 ± 4[a]	6		
	P18	33 ± 5[a]	7			88 ± 5	8
Bum		106 ± 2	4			73 ± 14	4
TTX		96 ± 19	4			84 ± 11	3
TEA		114 ± 14	4				
CNQX/D-L-AP5						93 ± 3	4

Supplementary Table 4: Summary of pharmacology.

a: significant reduction of NH_4^+-induced changes in $E_M/I_{NH4+}/[K^+]_o\uparrow$.

B Lists of figures and tables

List of figures

List of tables

C Publications

Next I have attached reprints or prepared manuscripts I contributed to during my time in the Institute for Neurobiology (IFN).

C.1 Stephan et al., in Preparation

Mechanisms of Ammonium-induced Depolarization of Astrocytes *in situ*

Jonathan Stephan, Nicole Haack, Daniel Koch, Simone Durry, Karl W. Kafitz, Gerald Seifert, Peter Hochstrate, Christian Steinhäuser, and Christine R. Rose

My contributions:

- vast majority of the whole-cell patch-clamp recordings (main part of the experimental data illustrated in all tables and figures)
- data analysis of all electrophysiological recordings
- overall statistics
- initial documentation of immunohistochemical labeling, together with S.D.
- complete illustration
- writing the first draft

C.2 Langer et al., Submitted

Intracellular sodium propagation between hippocampal astrocytes *in situ*

Julia Langer, Jonathan Stephan, Martin Theis, and Christine R. Rose

My contributions:

- dye coupling studies (figure 5*A*)
- discussion of the manuscript

Intercellular sodium propagation between hippocampal astrocytes *in situ*

Julia Langer[1], Jonathan Stephan[1], Martin Theis[2] & Christine R. Rose[1]*

Running Title: Sodium propagation between astrocytes

Total word count: 8374
Abstract: 250, Introduction: 545, Materials and Methods: 1124, Results: 2155, Discussion: 1730, Legends: 1021, Bibliography: 1337, Acknowledgements: 52
Figures: 6

[1]: Institute of Neurobiology, Heinrich-Heine-University Duesseldorf, Universitätsstrasse 1, D-40225 Duesseldorf, Germany
[2]: Institute of Cellular Neurosciences, Medical Faculty, University of Bonn, Sigmund-Freud-Strasse 25, D-53105 Bonn, Germany. E-mail: Martin.Theis@ukb.uni-bonn.de

* To whom correspondence should be addressed:
Institute of Neurobiology, Heinrich-Heine-University Duesseldorf, Universitaetsstrasse 1, 26.02.00, D-40225 Duesseldorf, Germany.
Tel.: +49 (0)211 81-13416, Fax: +49 (0)211 81-13415.
E-mail: rose@uni-duesseldorf.de

KEY WORDS
SBFI, gap junction, connexin, gliotransmitter, glutamate, ATP, glia

ABSTRACT

Activation of glutamatergic synapses results in long-lasting sodium transients in astrocytes that are mainly mediated by sodium-dependent glutamate uptake. Sodium elevations activate Na^+/K^+-ATPase and glucose uptake by astrocytes, representing a key signal for coupling glial metabolism to neuronal activity. Here, we analysed the characteristics of sodium propagation in the astrocyte network *in situ*. Stimulation of a single astrocyte in a hippocampal slice preparation resulted in an immediate sodium elevation in the stimulated cell that propagated to neighbouring astrocytes within a distance of approximately 100 µm. Amplitude, slope and propagation speed of sodium elevations in downstream cells decayed monotonically with increasing distance. In contrast to sodium, calcium increases elicited by electrical stimulation were restricted to the stimulated cell and a few neighbouring astrocytes. Pharmacological inhibition of glutamate uptake, mGluR1 and 5, or gap junctions reduced sodium propagation, whereas inhibition of purinergic receptors had no effect. Propagation was also reduced in animals at P4 and virtually omitted in Cx30/Cx43 double-deficient mice. Our results indicate that glial calcium signalling and release of glutamate are supportive of, but are not prerequisites for, the propagation of sodium between hippocampal astrocytes *in situ*, whereas expression of Cx30 and Cx43 is essential. Cx30/Cx43-mediated sodium propagation could thus represent a signal indicating increased metabolic needs both in the presence and in the absence of concomitant calcium signalling. Sodium propagation in the astrocyte network might also serve a homeostatic function by supporting the re-establishment of a steep sodium gradient and by lowering the metabolic burden opposed onto single cells.

INTRODUCTION

Astrocytes, just as neurons, maintain a steep inwardly directed sodium gradient that provides the driving force for a multitude of transport processes across their plasma membrane including Na^+/Ca^{2+}-exchange and sodium-dependent glutamate uptake through GLAST and GLT-1 (Danbolt 2001; Rose and Ransom 1996a; Verkhratsky 2010). At synapses, uptake of glutamate by astrocytes shapes the properties of transmission (Marcaggi and Attwell 2004; Schousboe et al. 2004), and failure of these transport systems following breakdown of the glial sodium gradient promotes neuronal dysfunction and damage (Danbolt 2001; Kelly et al. 2009; Rossi et al. 2000). While the fine tuning of synaptic transmission is thus to a large extent dependent upon optimal function of sodium-dependent astrocytic transport processes, recent work has provided evidence that glutamatergic synaptic activity is accompanied by long-lasting intracellular sodium transients in astrocytes *in situ* that arise mainly through activation of glutamate uptake (Bennay et al. 2008; Kirischuk et al. 2007; Langer and Rose 2009). In Bergmann glial cells, short-burst synaptic stimulation induced sodium transients in the mM range, and it was estimated that this will exert a negative feedback onto glutamate uptake by reducing its driving force by 25% (Bennay et al. 2008).

In addition to their direct influence on the activity of sodium-dependent membrane transport, astrocyte sodium elevations have been suggested to represent a key signal for coupling glial metabolism to neuronal activity (Magistretti 2009; Pellerin and Magistretti 1994). In cultured astrocytes, sodium elevations following activation of glutamate transport stimulate Na^+/K^+-ATPase and cause increased ATP consumption, aerobic glycolysis, and glycogen breakdown (Chatton et al. 2000; Pellerin and Magistretti 1994). In accordance with this view, it has been shown that the stimulation of GLUT-1-mediated glucose uptake by glutamate requires the concurrence of both sodium and calcium signals in astrocytes (Loaiza et al. 2003; Porras et al. 2008).

Astrocytes not only communicate with each other via release of gliotransmitters, but are also organized as directly coupled networks through gap junctions that mediate the passage of ions and small signalling molecules (Giaume et al. 2010; Halassa and Haydon 2010; Nagy and Rash 2000; Volterra and Meldolesi 2005). An earlier work in culture demonstrated that gap junctions are also involved in astrocyte sodium homeostasis by equalizing intracellular sodium concentrations between cells (Rose and Ransom 1997). Furthermore, gap junctions support the propagation of calcium waves between astrocytes

(Scemes and Giaume 2006) and allow the trafficking of glucose and its metabolites in an activity-dependent manner (Rouach et al. 2008).

Work in cultured astrocytes has provided evidence that astrocyte sodium transients might not be restricted to the site of sodium entry and to individual, activated astrocytes, but reach neighbouring cells following generation of a calcium wave and release of gliotransmitters (Bernardinelli et al. 2004). In light of the functional significance of astrocyte sodium signalling, we studied the characteristics and mechanisms of propagation of sodium in the astrocyte network *in situ*. To this end, we performed quantitative widefield sodium imaging in astrocytes in the *stratum radiatum* of acute mouse hippocampal slices. To selectively induce a sodium elevation in an individual cell, we applied direct electrical stimulation and monitored the spread of sodium to neighbouring astrocytes. Our results show that sodium rapidly propagates in the astrocyte network *in situ* and demonstrate that this propagation is dependent on the expression of Cx30 and Cx43.

MATERIALS AND METHODS

The study and all experiments were carried out in accordance with the institutional guidelines of the Heinrich-Heine-University Düsseldorf as well as the European Communities Council Directive (86/609/EEC).

Tissue preparation and SR101-staining

Experiments were performed on acute tissue slices (250 µm) of mouse hippocampus (*mus musculus*, Balb/C; postnatal days (P) 4 or 16-21) in the *stratum radiatum* of the CA1 area. Animals were decapitated following anaesthesia with CO_2 and their brains were rapidly removed. Sectioning of transverse hippocampal slices was performed in standard saline at 4-6 °C. The standard saline was composed of (in mM): 125 NaCl, 2.5 KCl, 2 $CaCl_2$, 1 $MgCl_2$, 1.25 NaH_2PO_4, 26 $NaHCO_3$ and 20 glucose, bubbled with 95% O_2 and 5% CO_2, resulting in a pH of 7.4. After sectioning, slices were kept at 34°C for 20 minutes in standard saline that contained 0.5-1 µM sulforhodamine 101 (SR101), followed by a 10 min incubation in saline without SR101 at 34°C. This procedure results in the selective staining of astrocytes as described earlier (Kafitz et al. 2008; Nimmerjahn et al. 2004). Afterwards, slices were kept in standard saline at room temperature (19-22°C) until they were used for experiments, which were also performed at room temperature.

For some experiments, transgenic mice with genetically uncoupled astrocytes were used which display astrocyte-directed conditional deletion of connexin43, as well as additional, unrestricted deletion of connexin30 (Wallraff et al. 2006), also called DKO mice. Wild-type C56/BL6 mice (P 22-23) served as additional controls for these experiments.

Sodium and calcium imaging

Cells were dye-loaded by bolus injection of the membrane-permeable form of SBFI (SBFI-AM; sodium-binding benzofuran isophthalate-acetoxymethyl ester; Molecular Probes/Invitrogen, Karlsruhe, Germany) into the CA1 region of the hippocampus (Meier et al. 2006). For some experiments, individual, SR101-positive astrocytes in the *stratum radiatum* of the CA1 area were loaded with SBFI through a patch pipette during standard whole-cell patch clamp (Meier et al. 2006). The pipette solution contained (in mM): 120 $KMeSO_3$, 32 KCl, 10 N-(2-Hydroxyethyl)piperazine-N′-(2-ethanesulfonic acid (HEPES), 4 NaCl, 4 Mg-ATP and 0.4 Na_3-GTP, 0.5-1 SBFI (tetra-ammonium salt), the pH was

adjusted to pH 7.3. Voltage-clamp recordings were obtained with an EPC10 amplifier (HEKA Elektronik, Lambrecht, Germany); „PatchMaster"-software (HEKA Elektronik, Lambrecht, Germany) was used for data acquisition. Cells were held at a membrane potential of -85 mV (liquid junction potential not corrected) for at least 15 min to ensure sufficient diffusion of SBFI into distal branches, then the pipette was carefully withdrawn. Cells were allowed to reseal for at least 10 minutes after which sodium imaging was started.

Wide-field fluorescence imaging was performed as described earlier (Langer and Rose 2009) using a variable scan digital imaging system (TILL Photonics, Martinsried, Germany) attached to an upright microscope (Olympus BX51Wi, Olympus Europe, Hamburg, Germany; 40x/60x water immersion objective, N.A. 0.8/0.9, Nikon/Olympus) and a CCD camera as sensor (TILL Imago VGA, TILL Photonics, Martinsried, Germany). The isosbestic (sodium-insensitive) excitation wavelength of SBFI is slightly below 340 nm; at longer wavelengths, fluorescence emission of SBFI decreases with increasing sodium concentration (Langer and Rose 2009; Meier et al. 2006). Based on this, 340 nm and 380 nm were chosen as alternate excitation wavelengths. Fluorescence emission (>440 nm) was collected at 4 Hz from defined regions of interest (ROI) containing cellular structures. After background correction, the fluorescence ratio (F_{340}/F_{380}) was calculated for individual ROIs and analyzed off-line by employing OriginPro Software (OriginLab Corporation, Northhampton, MA).

Changes in fluorescence ratio were expressed as changes in sodium concentration based on *in situ* calibrations of intracellular SBFI fluorescence in SR101-positive astrocytes as described in detail before (Meier et al. 2006; Rose and Ransom 1996a). Briefly, following loading with SBFI-AM, slices were perfused with calibration solutions containing different sodium concentrations as well as ionophores (3 µM gramicidin, 10 µM monensin) to equilibrate extra- and intracellular sodium concentrations. Stepwise changes in the sodium concentration of the calibration saline then caused stepwise changes in the SFBI ratio, indicating stepwise changes in the intracellular sodium concentration (n = 28). As reported earlier (Langer and Rose 2009; Meier et al. 2006), the correlation between changes in SBFI fluorescence and intracellular sodium concentration was virtually linear for sodium concentrations between 10 and 40 mM (n = 28, not shown), with a change in fluorescence ratio by 10% corresponding to a change of the intracellular sodium concentration by 3.8 mM.

For measurement of intracellular calcium transients, Fura-2-AM was bolus-injected into the *stratum radiatum*. Imaging was performed as described above for SBFI; excitation wavelengths were 357 and 380 nm and the fluorescence ratio (F_{357}/F_{380}) was calculated. Calcium transients are expressed as changes in fluorescence ratio normalized to the baseline (% $\Delta F/F$).

Stimulation of astrocytes

Stimulation of SR101-positive astrocytes was performed by single-cell electroporation (e.g. (Bernardinelli et al. 2004; Nevian and Helmchen 2007). A fine-tipped borosilicate glass pipette (Hilgenberg, Waldkappel, Germany) was filled with standard saline (pipette resistance: 2-3 MΩ) and was positioned onto the cell body of a selected cell. Delivering a short, single square pulse (30-50V, 1 ms) via the pipette now elicited an immediate rise in the SBFI fluorescence ratio of the stimulated cell, indicating an increase in intracellular sodium concentration due to transient influx of sodium through the plasma membrane. Cells, in which we observed an immediate substantial decrease in fluorescence at the isosbestic wavelength, indicative of cell damage and loss of membrane integrity, were discarded. Stimulation was only performed once for each cell and within each group of cells.

Dye-coupling studies

To study dye-coupling, astrocytes in the *stratum radiatum* of the CA1 area were subjected to whole cell patch-clamp as described above. Pipette solution contained no SBFI; instead 1 % neurobiotin, which easily diffuses through gap junctions, and 100 µM Alexa Fluor 594 (MW 759; for labelling of the patch-clamped cell) were added. Cells were held at -85 mV in the voltage-clamp mode for 45 min, after which the pipette was carefully withdrawn. Slices were then immediately fixed over night in 4 % PFA at +4 °C. Further processing was performed at room temperature (19-22°C). After fixation, slices were washed in phosphate buffered saline, permeabilized for 30 min in 0.25 % Triton X-100, and washed again. Next, the neurobiotin was labeled with 5 µg/ml Avidin-Alexa Fluor 488 for 2 h. Slices were finally washed and coversliped. Stainings were documented at an upright microscope (Nikon Eclipse FN1, 10x water immersion objective, N.A. 0.30, Nikon Europe, Düsseldorf, Germany). Images of Alexa 488 and Alexa 594 fluorescence were merged employing “Adobe Photoshop”-software.

All substances were applied with the bath perfusion system. Chemicals were purchased from Sigma, except for tetrodotoxin (Alomone Labs, Jerusalem, Israel or Biotrend Chemicals, Cologne, Germany).

Unless otherwise specified, data are presented as means ± S.E.M. If not stated otherwise, n represents the number of analysed cells. Each set of experiments was performed on at least 3 different slice preparations.

RESULTS

Propagation of sodium between astrocytes

SR101-positive astrocytes, located in the *stratum radiatum* of hippocampal slices from postnatal day (P) 16-21, had a somatic baseline intracellular sodium concentration of 12.4 ± 0.5 mM (n = 143), which is in agreement with values reported earlier (Kelly and Rose 2010; Langer and Rose 2009). To induce a sodium increase in an individual astrocyte, a fine pipette (tip diameter ~1µm) was positioned onto its cell body and a single current pulse (1 ms, 30-50 V) was applied. The electrical shock induced an immediate rise in the sodium concentration in the stimulated cell (see (Bernardinelli et al. 2004; Nevian and Helmchen 2007). The peak amplitude of the sodium increase in the directly stimulated cell was 14.5 ± 0.8 mM (range: 4-26 mM, 53 experiments), its slope (10-90%) was 0.3-6.9 mM/s (Fig. 1A: cell a1). Sodium signals in directly stimulated astrocytes, were not visibly different in the presence of tetrodotoxin (TTX; 0.5 µM) to block voltage-gated sodium channels, indicating that they were not dependent on action potential generation in neurons (4 experiments; not shown). Moreover, a single electrical shock to the tissue without visible contact of the pipette to a cell body or a primary astrocyte process did not result in somatic sodium signals in astrocytes in the field of view (4 experiments; not shown). The necessity of direct contact of the stimulation pipette with the cell soma for induction of an intracellular sodium increase indicates that it was caused by transient influx of sodium through the plasma membrane due to electroporation (Nevian and Helmchen 2007).

The electrical shock did not only induce a sodium signal in the stimulated cell, but also in neighbouring SR101-positive astrocytes (4-12 somata in the field of view within ± 5 µm of the focal plane in 53 experiments; Fig. 1A: cells a2 – a5). A 2-D plot showed that the normalized signal amplitudes in neighbouring astrocytes dropped with increasing distance from the stimulated cell (n = 108 cells from 18 experiments; Fig. 1B), generating a nearly circular expansion profile for propagation of sodium. Cells located within a radius of 40-50 µm exhibited amplitudes that reached about 30% of that of the stimulated cell; at 70-110 µm, average amplitudes had dropped to less than 10%. In the presence of TTX, the propagation of sodium signals was not different from control (4 experiments; not shown).

Because the expansion of sodium propagation in the astrocyte network was radial, data from cells located within the same distance were pooled for steps of 10 µm from the stimulated cell. Plotting the normalized amplitudes of sodium signals of surrounding

astrocytes against distance from the stimulated cell (n = 100 cells from 18 experiments; Fig. 1C) revealed that the decay over distance followed a monoexponential function (R^2=0.983). The same was true for the decay of the normalized slopes of sodium signals plotted against distance (R^2=0.994; Fig. 1C). Intracellular propagation speed as determined from the cell body of the stimulated cell to the cell bodies of its direct neighbours was ≥60 µm/s (based on a temporal resolution of 4 Hz) and dropped in a monotonic fashion to less than 10 µm/s at distances greater than 60 µm (n = 36; Fig. 1C).

Taken together, our results presented so far show that direct, single shock stimulation of an individual hippocampal astrocyte evokes an immediate increase in intracellular sodium in the stimulated cell that propagates to neighbouring astrocytes in all directions encompassing a total area of about 38000 µm^2. Amplitude, slope and propagation speed of sodium transients in downstream cells decay monoexponentially/monotonically with increasing distance from the stimulated cell.

Propagation of sodium along processes

To reveal the propagation of sodium signals between astrocytes and along astrocyte processes in greater detail, two neighbouring SR101-positive cells were loaded individually with SBFI through a patch pipette. To this end, cells were successively held in the whole-cell patch-clamp mode for about 15 minutes, after which the patch pipette was carefully withdrawn and the cells were allowed to reseal. After this loading procedure, SBFI fluorescence could be detected with low background from both astrocytes including their primary processes, fine processes arising from them and endfeet on blood vessels (Fig. 2A, B: a2, a3). Subsequently, a stimulation pipette was positioned onto the cell body of a third SR101-positive astrocyte in the immediate neighbourhood (Fig. 2A: a1) and this cell was stimulated electrically.

As described before (cf. Fig. 1A), the stimulation resulted in a sodium increase in the somata of the neighbouring, SBFI-loaded cells (Fig. 2B). Please note that a1 was not loaded with SBFI and therefore sodium signals were not recorded from this cell. In addition to somatic sodium signals, we could now resolve sodium transients in all other cellular regions of the SBFI-stained astrocytes. Again signal amplitudes and slopes decreased, while the delay increased with distance (n = 4; Fig. 2B). Notably, sodium also invaded astrocyte endfeet on blood vessels (Fig. 2A, B). To estimate the propagation speed of sodium signals along astrocyte processes, we placed rectangular regions of interest along a straight line connecting the cell bodies of the SBFI-filled cells (Fig. 2C). We found

that the signal started within the first second after the electrical stimulation in the region closest to the stimulated cell. In the experiment shown in Fig. 2C, apparent propagation speed along the linearized track was about 14 µm/s for the distance between 54-65 µm. In the region farthest away, placed over the second cell at a distance of 145 µm, signal onset took more than 15 seconds and apparent propagation speed from the neighbouring region was reduced to about 2 µm/s (Fig. 2C).

Role of gliotransmitters and calcium signalling

An earlier work on astrocytes in culture has found evidence that direct electrical stimulation can cause the release of gliotransmitters from the stimulated astrocyte which activate neighbouring cells, resulting in the spread of sodium signals in a wave-like manner from cell to cell (Bernardinelli et al. 2004). In order to probe for the role of gliotransmitters in the propagation of sodium between astrocytes *in situ*, we analyzed the effect of blockers of purinergic transmission by applying PPADS (pyridoxalphosphate-6-azophenyl-2',4'-disulfonic acid tetrasodium salt; 20 µM; 6 experiments), a blocker of purinergic receptors, or MRS2179 (2'-deoxy-N^6-methyladenosine 3',5'-bisphosphate tetrasodium salt; 30 µM; 6 experiments), which preferentially blocks metabotropic P2Y receptors. None of these blockers significantly affected the amplitude or the slope of sodium signals in neighbouring cells in response to direct stimulation of an astrocyte (Fig. 3A). The correlation factors of the monoexponential fits were high (R^2>0.97), indicating that these blockers did not induce a higher variability to the progression of the wave (Fig. 3A). Thus, ATP release by stimulated astrocytes does not significantly contribute to the propagation of sodium signals.

A possible involvement of sodium-dependent glutamate uptake was tested by applying the non-transported, competitive glutamate-uptake blocker TFB-TBOA ((3*S*)-3-[[3-[[4-(Trifluoromethyl)benzoyl]amino]phenyl]methoxy]-L-aspartic acid; 5 µM; 7 experiments). TFB-TBOA slightly dampened the peak amplitudes in cells surrounding the stimulated astrocyte, while the slope of sodium signals was virtually unaltered (Fig. 3B). We next analysed the involvement of calcium signalling induced by release of glutamate and activation of metabotropic glutamate receptors on surrounding cells. Pharmacological inhibition of metabotropic glutamate receptors 1 and 5 (mGluR1, 5) by combined application of YM298198 (6-Amino-*N*-cyclohexyl-N,3-dimethylthiazolo[3,2-*a*]benzimidazole-2-carbox-amide hydrochloride, 1 µM) and MPEP (2-Methyl-6-

(phenylethynyl)pyridine hydro-chloride, 25 µM; 4 experiments) reduced both amplitude and slope of sodium signals (Fig. 3C).

In cultured astrocytes, a preceding calcium wave was reported to be critically required for the propagation of sodium waves between neighbouring cells (Bernardinelli et al. 2004). To study if glial calcium waves might underlie and drive the observed propagation of sodium in hippocampal astrocytes *in situ*, we performed calcium imaging experiments using Fura-2. A single electrical shock induced an immediate and long-lasting rise in the intracellular calcium concentration in the directly stimulated cell (7 experiments; Fig. 4). In contrast to the long-ranged expansion of sodium signals, however, no classical calcium wave was induced by our stimulation paradigm and only a minority of SR101-positive astrocytes in close proximity to the stimulated cell underwent delayed oscillations (7 experiments; Fig. 4).

In summary, these results suggest that glutamate-induced signalling contributes to the propagation of sodium between astrocytes following stimulation of a single cell. However, significant propagation persisted in the presence of mGluR- and glutamate uptake blockers. Moreover, the number of involved astrocytes (sodium signals were detected in virtually every SR101-positive cell within the propagation range) as well as the distance over which sodium signals were detected (~100 µm from the stimulated cell) by far exceeded that of astrocytes showing calcium signals. Thus, in contrast to results reported in cell culture, release of gliotransmitters and the generation of a calcium wave are supportive of, but are not prerequisites for, the propagation of sodium between astrocytes *in situ*.

Role of gap junctional coupling and connexins

In cultured astrocytes, it has been shown that sodium can easily travel through gap junctions (Rose and Ransom 1997). Therefore, we analysed the possible involvement of gap junctions in the propagation of sodium signals between cells. Gap junctional coupling between astrocytes develops during the first postnatal weeks and accompanies their maturation (Nagy et al. 1999; Ransom and Ye 2005; Yamamoto et al. 1992). To estimate the size of the astrocyte network in our preparation, we studied dye-coupling at P16-P20. To this end, a selected astrocyte was held in the voltage-clamp mode for 45 min, allowing the diffusion of neurobiotin that was included into the pipette solution to surrounding cells through gap junctions. After that, slices were immediately fixed and processed. On average, the dye spread to 49 ± 29 cells within this time window (14 slices; Fig. 5A P16).

In P3 animals, the same experimental protocol resulted in staining of only 27 ± 19 cells (4 slices; Fig. 5A), confirming less gap junctional coupling at this stage of development.

To study the influence of reduced gap junctional coupling on the propagation of sodium transients between astrocytes, we performed experiments in slices derived from P4 animals. At P4, baseline sodium concentration of hippocampal astrocytes was 8.3 ± 0.3 mM (n = 117). As described for older animals, direct stimulation of a single astrocyte induced a steep increase in intracellular sodium (7 experiments; Fig. 5B). Moreover, sodium elevations were observed in neighboring cells and the propagation pattern was approximately circular (7 experiments; Fig. 5C). Compared to older animals, however, sodium propagation at P4 abated much faster with increasing distance and included fewer cells (Fig. 5B-D). While signal amplitudes decreased by about 70% within a distance of 20 µm of the stimulated cell in P4 animals, they dropped by less than 40% within this distance in P16-21 animals (Fig. 5C, D). Normalized slopes, in contrast, were only slightly reduced in young as compared to older brains (Fig. 5DC). These results show that propagation of sodium between astrocytes is age-dependent and increases with maturation of the astrocytic network.

To further unravel a possible contribution of gap junctional coupling to propagation of sodium in P16-21 animals, we performed direct electrical stimulations in the presence of the gap junction blocker carbenoxolone (CBX, 200 µM). Application of CBX did not alter the slope of sodium signals in surrounding astrocytes (4 experiments; Fig. 5E). We, however, found that the distance-dependent decay of amplitudes could no longer be plotted satisfactorily by a monoexponential function ($R^2 = 0.893$; Fig. 5E). These data indicate that manipulation of gap junctional coupling by application of CBX may perturb the propagation of sodium signals between astrocytes.

While carbenoxolone was shown to efficiently inhibit dye diffusion between astrocytes through gap junctions (Blomstrand and Giaume 2006; Rouach et al. 2003), it also exerts unspecific effects (Rouach et al. 2003; Ye et al. 2009) and might not completely impede electrical coupling and ion diffusion (Meme et al. 2009). We, therefore, studied propagation of sodium in the astrocytic network in transgenic mice with genetically uncoupled astrocytes. Experiments were performed in DKO mice which display conditional astrocyte-directed deletion of connexin43, as well as additional, unrestricted deletion of connexin30 (Wallraff et al. 2006). Wild-type C56/BL6 mice (P 22-23) served as additional controls for these experiments.

Baseline intracellular sodium concentration was 9.8 ± 0.5 mM in astrocytes in wildtype C57/BL6 mice (n = 51) and 8.4 ± 0.5 mM in DKO mice (n = 50). The sodium increase upon an electrical shock in the directly stimulated cell as well as the amplitudes, slopes and expansion of sodium signals in surrounding astrocytes were similar in Balb/C and wild-type C57/BL6 mice (7 experiments; Fig. 6A-C). In DKO mice, direct electrical stimulation of an astrocyte induced a steep increase in intracellular sodium as described before (9 experiments; Fig. 6D). In striking contrast to wild-type animals, however, the propagation of sodium signals to neighboring astrocytes was virtually nonexistent (9 experiments; Fig. 6D-F). Only in directly adjacent cells, minor sodium elevations close to the detection threshold were observed (Fig. 6D-F).

These results demonstrate that propagation of sodium between SR101-positive hippocampal astrocytes *in situ* is dependent on the expression of connexins 30 and 43.

DISCUSSION

Our results show that sodium signals evoked by direct stimulation in single astrocytes in mouse hippocampal slices propagate in a radial manner to virtually all neighbouring astrocytes. Amplitude, slope and apparent velocity of propagation in downstream cells decay monotonically with increasing distance from the stimulated cell. Calcium signals induced by the same stimulation paradigm were largely restricted to the stimulated cell and only rarely included neighbouring astrocytes. Inhibition of mGluR, glutamate uptake and gap junctions reduced propagation, while purinergic receptor blockers had no effect. Propagation was greatly reduced in animals at postnatal day 4 and virtually omitted in genetically uncoupled DKO mice.

Inter- and intracellular propagation of sodium

Hippocampal astrocytes experience long-lasting sodium transients in response to activation of glutamatergic synapses or following exogenous application of glutamate or D-aspartate (Chatton et al. 2000; Langer and Rose 2009; Rose and Ransom 1996b). With both stimulation paradigms, sodium transients were never restricted to single cells, but generally included several astrocytes. While this might have been partly caused by propagation of sodium between astrocytes, simultaneous activation of several cells, either synaptically or by extracellular diffusion of the applied agonists, could not be ruled out. Thus, in the present study, direct electrical stimulation was performed to provide selective stimulation of single cells and to enable analysis of the mechanisms of intercellular propagation of sodium *in situ*.

Direct electrical stimulation of a single cell caused an immediate elevation in intracellular sodium that radially spread to all surrounding astrocytes. Amplitude, slope as well as propagation speed decreased monotonically with increasing distance from the centre cell. This indicated that the sodium signals did not undergo significant amplification by regenerative mechanisms during intercellular propagation as observed for some types of calcium waves (Scemes and Giaume 2006). The apparent *intra*cellular propagation speed along processes matched the values for *inter*cellular propagation determined from somatic recordings, indicating that cellular borders did not considerably retard propagation. Sodium is not substantially buffered by intracellular components nor the added indicator, and intracellular diffusion coefficients are in the range of 600-800 μm^2/sec (Albritton et al. 1992; Kushmerick and Podolsky 1969), which is more than an order of magnitude higher

than that of buffered diffusion of calcium or IP_3 (Yuste et al. 2000). If the observed propagation was appreciably based on intercellular diffusion of sodium, its velocity should thus be significantly faster than that reported for calcium waves (Scemes and Giaume 2006). Propagation speed from cell body to cell body ranged from ≥60 µm/s in the direct neighbourhood of the stimulated cell, to less than 10 µm/s at distances greater than 60 µm. Thus, the apparent initial velocity of sodium propagation between astrocytes by far exceeds that of classical astrocyte calcium waves, which move with a uniform speed of about 10-20 µm/s (Scemes and Giaume 2006). It also exceeds the speed of sodium waves driven by calcium waves observed in astrocyte culture (14 µm/s; (Bernardinelli et al. 2004). Certainly it has to be emphasized that the true propagation speeds for both ions will be considerably larger because of the elaborate morphology of astrocyte processes *in situ* (Bushong et al. 2002; Nedergaard et al. 2003).

Propagation of sodium elevations included all cellular compartments including astrocyte endfeet. Endfeet preferentially express the facilitative glucose transporter GLUT1, which is activated by simultaneous intracellular sodium and calcium signals in response to glutamate application (Porras et al. 2008). Thus, our results suggest that sodium transients induced by activation of sodium-dependent glutamate uptake in processes close to synapses (see (Langer and Rose 2009) can propagate throughout the entire cell to astrocyte endfeet on blood vessels and thereby support activation of glucose uptake through GLUT1.

Gliotransmitters are not required for propagation of sodium

In cultured cortical astrocytes, it was observed that the occurrence of a sodium wave in response to direct electrical stimulation required the existence of a calcium wave and the release of ATP and glutamate that preceded the sodium signal (Bernardinelli et al. 2004). While different mechanisms seem to govern calcium wave propagation in different brain regions (Scemes and Giaume 2006), calcium waves critically depended on the release of ATP and activation of purinergic receptors in the CA1 region of the hippocampus (Haas et al. 2006). We, however, found that blocking purinergic transmission did not alter the propagation of sodium between hippocampal astrocytes. Moreover, inhibition of metabotropic glutamate receptors 1 and 5, as well as of sodium-dependent glutamate transporters reduced, but did not inhibit the propagation of sodium. Furthermore, our single-pulse stimulation paradigm did not induce a classical long-range calcium wave described in other studies (Haas et al. 2006; Scemes and Giaume 2006). Instead, a

prominent calcium signal was only detected in the directly stimulated cell and a minority of surrounding astrocytes. Thus, the distance over which sodium signals were detected by far exceeded that of astrocytes showing calcium signals.

Our results indicate that release of glutamate by the directly stimulated cell as well as by some secondary cells augmented sodium signals and thereby increased the range of sodium propagation between cells. Apart from exocytotic vesicles, such glutamate release might have been mediated by lysosome exocytosis, anion channels, P2X7-receptors, reversal of glutamate transporters and/or connexin/pannexin hemichannels (Malarkey and Parpura 2008; Perea et al. 2009). Propagation of sodium signals was also reduced in the presence of TBOA, suggesting that sodium-dependent uptake of glutamate, which is largely responsible for the generation of synaptically induced sodium signals in astrocytes (Bennay et al. 2008; Kirischuk et al. 2007; Langer and Rose 2009; Voutsinos-Porche et al. 2003), plays a role. Moreover, generation of calcium signals upon activation of mGluR1 and 5, further release of glutamate and subsequent activation of glutamate uptake might contribute to this phenomenon.

Taken together our data is in agreement with a calcium- and gliotransmitter dependent component for the generation of sodium waves between astrocytes (Bernardinelli et al. 2004). They, however, clearly show that neither the release of the gliotransmitters ATP or glutamate, nor preceding or concomitant calcium waves are required *per se* for the propagation of sodium between astrocytes.

Propagation of sodium depends on Cx30/43

Astrocytes are extensively coupled through gap junctions, intercellular communication channels consisting of two opposing hemichannels composed of connexins (Cx) (Giaume and Theis 2010; Harris 2001; Nagy and Rash 2000). In the mouse hippocampus, astrocytes express both Cx43 as well as Cx30 (Dermietzel et al. 1989; Nagy et al. 1999) and animals that lack either of those show reduced dye coupling (Gosejacob et al. 2011; Theis et al. 2003), whereas animals lacking both show complete absence of dye-coupling (Kunze et al. 2009; Rouach et al. 2008; Wallraff et al. 2006). Cx43 and gap junctions are prerequisites for the propagation of calcium waves in the neocortex (Haas et al. 2006), while calcium waves in the hippocampus were still present in transgenic animals with conditional deletion of Cx43 expression in astrocytes (Haas et al. 2006).

In our study, animals at postnatal day 3 displayed a considerably smaller number of dye-coupled cells than at older age (P16-21), confirming earlier work reporting that an

increase in gap junctional coupling accompanies maturation of astrocytes (Nagy et al. 1999; Schools et al. 2006; Yamamoto et al. 1992). At the same time, the range of sodium propagation was greatly reduced in P4 animals, pointing towards a contribution of gap junction coupling to sodium propagation. In DKO mice which display astrocyte-directed, conditional deletion of connexin43, as well as additional, unrestricted deletion of connexin30 in astrocytes (Wallraff et al. 2006), the sodium elevation was virtually restricted to the stimulated cell. Thus, expression of Cx30 and Cx43 was a prerequisite for the propagation of sodium suggesting that it was mainly based on passage through gap junctions. Because our experiments also showed that propagation of sodium was supported by glutamate, the nearly complete block of sodium propagation in DKO mice indicates that the release of glutamate might have been mediated by Cx hemichannels (Spray et al. 2006; Ye et al. 2003).

Functional implications

It is well established that astrocytes can generate intercellular calcium waves, which may provide a basis for a long-range signaling pathway (Scemes and Giaume 2006). Our results now demonstrate that, in addition, sodium signals evoked in a single cell *in situ* will rapidly propagate to neighboring cells through gap junctions, and that this propagation is primarily independent from a concomitant calcium wave. Astrocytes in the *stratum radiatum* of the rat hippocampus are directly coupled to on average 11 other astrocytes with a mean interastrocytic distance of 45 µm (Xu et al. 2010). Speed of sodium propagation was >60µm/s to the nearest neighbours, indicating that somatic sodium signals generated in a single cell will reach about ten directly coupled astrocytes appreciably faster than calcium waves, which travel at 10-20 µm/s (Scemes and Giaume 2006).

Several studies have established that glutamatergic synaptic activity is accompanied by long-lasting intracellular sodium transients in astrocytes *in situ* that arise mainly through activation of glutamate uptake (Bennay et al. 2008; Kirischuk et al. 2007; Langer and Rose 2009). Depending on the stimulation parameters, either local or global sodium transients were elicited, indicating that their amplitude and spatial profile reflect the site and strength of synaptic activation (Bennay et al. 2008; Langer and Rose 2009). Astrocyte sodium loads result in increased Na^+/K^+-ATPase activity, and propagation of sodium signals through gap junctions will thus promote pump-mediated uptake of extracellular potassium (Kimelberg 2010; Kofuji and Newman 2009). In addition, increased ATP consumption by the Na^+/K^+-ATPase enhances glycolysis and production of

lactate which could then serve as metabolic fuel for activated neurons (Chatton et al. 2000; Magistretti 2009; Magistretti and Chatton 2005; Pellerin and Magistretti 1994). Close to activated synapses, where sodium transients are largest, stimulation of glycolysis and lactate production will be strongest. Because sodium propagates through gap junctions, metabolic activation will, however, not be restricted to directly activated astrocytes, but include neighbouring cells, albeit to a lower degree. At the same time, gap junctions also provide the pathway for activity-dependent passage of glucose which is directed to active sites, providing the fuel necessary for increased glycolysis (Rouach et al. 2008).

An evident consequence of sodium diffusion through gap junctions is the dissipation of local sodium elevations. Thus, propagation of sodium through the astrocyte network may also serve a "homeostatic" function by accelerating the re-establishment of low intracellular sodium concentrations. This will not only support the maintenance of sodium-dependent transport activity close to activated synapses, but also lower the metabolic burden opposed onto a stimulated cell.

ACKNOWLEDGEMENTS

We thank Dr. Karl W. Kafitz for help with the establishment of imaging experiments and Anja Matijevic for excellent technical assistance. This study was supported by grants from the Deutsche Forschungsgemeinschaft to CR (Ro 2327/4-3) and MT (SFB/TR3 C9, N01; SPP 1172 TH 1350/1-1) and from the EU to MT (FP7-202167 NeuroGLIA).

Author contributions

J. Langer and C. R. Rose contributed to the design, analysis and interpretation of experiments. J. Langer performed the imaging experiments; J. Stephan performed the dye-coupling studies. M. Theis provided theCx30/40 double knockout mice. J. Langer and C. R. Rose contributed to drafting and all authors contributed to critical revision of manuscript for intellectual content and final approval of version to be published.

REFERENCES

Albritton NA, Meyer T, Stryer L. 1992. Range of messenger action of calcium ion and inositol 1,4,5-trisphosphate. Science 258:1812-1815.

Bennay M, Langer J, Meier SD, Kafitz KW, Rose CR. 2008. Sodium signals in cerebellar Purkinje neurons and Bergmann glial cells evoked by glutamatergic synaptic transmission. Glia 28:28.

Bernardinelli Y, Magistretti PJ, Chatton JY. 2004. Astrocytes generate Na+-mediated metabolic waves. Proc Natl Acad Sci U S A 101(41):14937-42.

Blomstrand F, Giaume C. 2006. Kinetics of endothelin-induced inhibition and glucose permeability of astrocyte gap junctions. J Neurosci Res 83(6):996-1003.

Bushong EA, Martone ME, Jones YZ, Ellisman MH. 2002. Protoplasmic astrocytes in CA1 stratum radiatum occupy separate anatomical domains. J Neurosci 22(1):183-92.

Chatton JY, Marquet P, Magistretti PJ. 2000. A quantitative analysis of L-glutamate-regulated Na^+ dynamics in mouse cortical astrocytes: implications for cellular bioenergetics. Eur J Neurosci 12(11):3843-53.

Danbolt NC. 2001. Glutamate uptake. Prog Neurobiol 65(1):1-105.

Dermietzel R, Traub O, Hwang TK, Beyer E, Bennett MV, Spray DC, Willecke K. 1989. Differential expression of three gap junction proteins in developing and mature brain tissues. Proc Natl Acad Sci U S A 86(24):10148-52.

Giaume C, Koulakoff A, Roux L, Holcman D, Rouach N. 2010. Astroglial networks: a step further in neuroglial and gliovascular interactions. Nat Rev Neurosci 11(2):87-99.

Giaume C, Theis M. 2010. Pharmacological and genetic approaches to study connexin-mediated channels in glial cells of the central nervous system. Brain Res Rev 63(1-2):160-76.

Gosejacob D, Dublin P, Bedner P, Huttmann K, Zhang J, Tress O, Willecke K, Pfrieger F, Steinhauser C, Theis M. 2011. Role of astroglial connexin30 in hippocampal gap junction coupling. Glia 59(3):511-9.

Haas B, Schipke CG, Peters O, Sohl G, Willecke K, Kettenmann H. 2006. Activity-dependent ATP-waves in the mouse neocortex are independent from astrocytic calcium waves. Cereb Cortex 16(2):237-46.

Halassa MM, Haydon PG. 2010. Integrated brain circuits: astrocytic networks modulate neuronal activity and behavior. Annu Rev Physiol 72:335-55.

Harris AL. 2001. Emerging issues of connexin channels: biophysics fills the gap. Q Rev Biophys 34(3):325-472.

Kafitz KW, Meier SD, Stephan J, Rose CR. 2008. Developmental profile and properties of sulforhodamine 101--Labeled glial cells in acute brain slices of rat hippocampus. J Neurosci Methods 169(1):84-92.

Kelly T, Kafitz KW, Roderigo C, Rose CR. 2009. Ammonium-evoked alterations in intracellular sodium and pH reduce glial glutamate transport activity. Glia(9):921-934.

Kelly T, Rose CR. 2010. Ammonium influx pathways into astrocytes and neurones of hippocampal slices. J Neurochem 115(5):1123-36.

Kimelberg HK. 2010. Functions of mature mammalian astrocytes: a current view. Neuroscientist 16(1):79-106.

Kirischuk S, Kettenmann H, Verkhratsky A. 2007. Membrane currents and cytoplasmic sodium transients generated by glutamate transport in Bergmann glial cells. Pflugers Arch 454(2):245-52.

Kofuji P, Newman E. 2009. Regulation of potassium by glial cells in the central nervous system. New York: Springer. pp. 151-175 p.

Kunze A, Congreso MR, Hartmann C, Wallraff-Beck A, Huttmann K, Bedner P, Requardt R, Seifert G, Redecker C, Willecke K and others. 2009. Connexin expression by radial glia-like cells is required for neurogenesis in the adult dentate gyrus. Proc Natl Acad Sci U S A 106(27):11336-41.

Kushmerick MJ, Podolsky RJ. 1969. Ionic mobility in muscle cells. Science 166(910):1297-8.

Langer J, Rose CR. 2009. Synaptically induced sodium signals in hippocampal astrocytes in situ. J Physiol 587(Pt 24):5859-77.

Loaiza A, Porras OH, Barros LF. 2003. Glutamate triggers rapid glucose transport stimulation in astrocytes as evidenced by real-time confocal microscopy. J Neurosci 23(19):7337-42.

Magistretti PJ. 2009. Role of glutamate in neuron-glia metabolic coupling. Am J Clin Nutr 90(3):875S-880S.

Magistretti PJ, Chatton JY. 2005. Relationship between L-glutamate-regulated intracellular Na+ dynamics and ATP hydrolysis in astrocytes. J Neural Transm 112(1):77-85.

Malarkey EB, Parpura V. 2008. Mechanisms of glutamate release from astrocytes. Neurochem Int 52(1-2):142-54.

Marcaggi P, Attwell D. 2004. Role of glial amino acid transporters in synaptic transmission and brain energetics. Glia 47(3):217-25.

Meier SD, Kovalchuk Y, Rose CR. 2006. Properties of the new fluorescent Na+ indicator CoroNa Green: comparison with SBFI and confocal Na+ imaging. J Neurosci Methods 155(2):251-9.

Meme W, Vandecasteele M, Giaume C, Venance L. 2009. Electrical coupling between hippocampal astrocytes in rat brain slices. Neurosci Res 63(4):236-43.

Nagy JI, Patel D, Ochalski PA, Stelmack GL. 1999. Connexin30 in rodent, cat and human brain: selective expression in gray matter astrocytes, co-localization with connexin43 at gap junctions and late developmental appearance. Neuroscience 88(2):447-68.

Nagy JI, Rash JE. 2000. Connexins and gap junctions of astrocytes and oligodendrocytes in the CNS. Brain Res Brain Res Rev 32(1):29-44.

Nedergaard M, Ransom B, Goldman SA. 2003. New roles for astrocytes: redefining the functional architecture of the brain. Trends Neurosci 26(10):523-30.

Nevian T, Helmchen F. 2007. Calcium indicator loading of neurons using single-cell electroporation. Pflugers Arch 454(4):675-88.

Nimmerjahn A, Kirchhoff F, Kerr JN, Helmchen F. 2004. Sulforhodamine 101 as a specific marker of astroglia in the neocortex in vivo. Nat Methods 1(1):31-7.

Pellerin L, Magistretti PJ. 1994. Glutamate uptake into astrocytes stimulates aerobic glycolysis: a mechanism coupling neuronal activity to glucose utilization. Proc Natl Acad Sci U S A 91(22):10625-9.

Perea G, Navarrete M, Araque A. 2009. Tripartite synapses: astrocytes process and control synaptic information. Trends Neurosci 32(8):421-31.

Porras OH, Ruminot I, Loaiza A, Barros LF. 2008. Na(+)-Ca(2+) cosignaling in the stimulation of the glucose transporter GLUT1 in cultured astrocytes. Glia 56(1):59-68.

Ransom BR, Ye Z-C. 2005. Gap junctions and hemichannels. Oxford: Oxford University Press. 177-189 p.

Rose CR, Ransom BR. 1996a. Intracellular Na^+ homeostasis in cultured rat hippocampal astrocytes. J Physiol 491(2):291-305.

Rose CR, Ransom BR. 1996b. Mechanisms of H^+ and Na^+ changes induced by glutamate, kainate, and D-Aspartate in rat hippocampal astrocytes. J Neurosci 16:5393-5404.

Rose CR, Ransom BR. 1997. Gap junctions equalize intracellular Na^+ concentration in astrocytes. Glia 20:299-307.

Rossi DJ, Oshima T, Attwell D. 2000. Glutamate release in severe brain ischaemia is mainly by reversed uptake. Nature 403(6767):316-21.

Rouach N, Koulakoff A, Abudara V, Willecke K, Giaume C. 2008. Astroglial metabolic networks sustain hippocampal synaptic transmission. Science 322(5907):1551-5.

Rouach N, Segal M, Koulakoff A, Giaume C, Avignone E. 2003. Carbenoxolone blockade of neuronal network activity in culture is not mediated by an action on gap junctions. J Physiol 553(Pt 3):729-45.

Scemes E, Giaume C. 2006. Astrocyte calcium waves: what they are and what they do. Glia 54(7):716-25.

Schools GP, Zhou M, Kimelberg HK. 2006. Development of gap junctions in hippocampal astrocytes: evidence that whole cell electrophysiological phenotype is an intrinsic property of the individual cell. J Neurophysiol 96(3):1383-92.

Schousboe A, Sarup A, Bak LK, Waagepetersen HS, Larsson OM. 2004. Role of astrocytic transport processes in glutamatergic and GABAergic neurotransmission. Neurochem Int 45(4):521-7.

Spray DC, Ye ZC, Ransom BR. 2006. Functional connexin "hemichannels": a critical appraisal. Glia 54(7):758-73.

Theis M, Jauch R, Zhuo L, Speidel D, Wallraff A, Doring B, Frisch C, Sohl G, Teubner B, Euwens C and others. 2003. Accelerated hippocampal spreading depression and enhanced locomotory activity in mice with astrocyte-directed inactivation of connexin43. J Neurosci 23(3):766-76.

Verkhratsky A. 2010. Physiology of neuronal-glial networking. Neurochem Int 57(4):332-43.

Volterra A, Meldolesi J. 2005. Astrocytes, from brain glue to communication elements: the revolution continues. Nat Rev Neurosci 6(8):626-40.

Voutsinos-Porche B, Bonvento G, Tanaka K, Steiner P, Welker E, Chatton JY, Magistretti PJ, Pellerin L. 2003. Glial glutamate transporters mediate a functional metabolic crosstalk between neurons and astrocytes in the mouse developing cortex. Neuron 37(2):275-86.

Wallraff A, Kohling R, Heinemann U, Theis M, Willecke K, Steinhauser C. 2006. The impact of astrocytic gap junctional coupling on potassium buffering in the hippocampus. J Neurosci 26(20):5438-47.

Xu G, Wang W, Kimelberg HK, Zhou M. 2010. Electrical coupling of astrocytes in rat hippocampal slices under physiological and simulated ischemic conditions. Glia 58(4):481-93.

Yamamoto T, Vukelic J, Hertzberg EL, Nagy JI. 1992. Differential anatomical and cellular patterns of connexin43 expression during postnatal development of rat brain. Brain Res Dev Brain Res 66(2):165-80.

Ye ZC, Oberheim N, Kettenmann H, Ransom BR. 2009. Pharmacological "cross-inhibition" of connexin hemichannels and swelling activated anion channels. Glia 57(3):258-69.

Ye ZC, Wyeth MS, Baltan-Tekkok S, Ransom BR. 2003. Functional hemichannels in astrocytes: a novel mechanism of glutamate release. J Neurosci 23(9):3588-96.

Yuste R, Majewska A, Holthoff K. 2000. From form to function: calcium compartmentalization in dendritic spines. Nat Neurosci 3(7):653-9.

FIGURE LEGENDS

Figure 1. Sodium transients in astrocytes evoked by direct electrical stimulation. ***A,*** Top: Transmitted light image of the *stratum radiatum* (CA1 area). At the lower right, the stimulation pipette positioned on the cell body of an astrocyte (a1) can be seen. Cell bodies of SR101-positive astrocytes (a1-a5) analyzed in the experiment depicted below are highlighted in green. Bottom: Intracellular sodium elevations in the astrocytes a1-a5 in response to direct electrical stimulation of a1. Time point of stimulation at 1ms/40V is indicated by the arrowhead and the perpendicular line. ***B***, Cumulative 2D plot of peak amplitudes of sodium transients, normalized to the signal amplitude of the directly stimulated cell, projected over a transmitted light image of the CA1 region. Values were plotted at their correct coordinate pair for every astrocyte relative to the stimulated cell. ***C***, Mean values (± S.E.M.) of normalized amplitudes (top) and slopes (middle) of sodium elevations in surrounding astrocytes, plotted against their distance from the directly stimulated cell. Values were pooled for steps of 10 µm circles, centered at the directly stimulated cell, starting at a minimal distance of 20 µm. Grey lines represent monoexponential fits of the data, R^2 indicates the regression coefficient. Bottom: Bar graph illustrating dependence of mean values for propagation speed from the distance to the stimulated cell.

Figure 2. Propagation of sodium along processes. ***A***, Left: Fluorescence image of SR101-stained astrocytes (a1-a3). At the top, a stimulation pipette, positioned on the cell body of a1, is indicated schematically. Grey open arrowheads point to endfeet on blood vessels. The inset shows the endfoot of a3 at elevated contrast. Right: SBFI fluorescence; cells a2 and a3 were individually filled with SBFI through a path pipette. The position of a1 with the stimulation pipette attached is indicated schematically at the top left. ***B***, Top: Inverted image of SBFI fluorescence of cells a2 and a3, indicating the regions of interest analyzed in the experiment depicted below. Bottom: Sodium signals in the different cellular regions of a2 and a3 in response to direct stimulation of a1. Note that sodium elevations also comprise endfeet on blood vessels. ***C***, Top: Inverted image of SBFI fluorescence of cells a2 and a3. Coloured boxes represent the regions of interest from which sodium signals are given below. Bottom: Sodium signals detected in the rectangular regions of interest, illustrating the propagation of sodium along a virtual linear track away from the stimulated cell. Distances between the soma of a1 and regions of interest are given for each trace;

open arrowheads indicate the onset of the sodium signal in each region. Closed arrowheads and perpendicular lines in *B* and *C* represent the time point of direct electrical stimulation of cell a1.

Figure 3. Role of gliotransmitters in propagation of sodium between astroyctes. ***A-D***, Mean values (± S.E.M.) of normalized amplitudes (left) and slopes (right) of sodium elevations in surrounding astrocytes in the presence of the purinergic receptor blocker PPADS (20 μM; *A top*), the P2Y-receptor blocker MRS 2179 (30 μM; *A bottom*), the glutamate uptake blocker TFB-TBOA (5 μM, *B*), and YM (1 μM) together with MPEP (25 μM), which block mGluR1 and 5 (*C*). The black lines represent monoexponential fits of the data, R^2 indicate the regression coefficients. Grey lines represent the monoexponential fits of the control experiments (cf. Fig. 1C).

Figure 4. Calcium transients in astrocytes evoked by direct electrical stimulation.
Top left: Transmitted light image of the *stratum radiatum* (CA1 area). At the lower right, the stimulation pipette positioned on the cell body of an astrocyte (a1) can be seen. Somata of cells (a1-c4) analyzed in the experiment depicted below are highlighted in green. Top right: SR101-fluorescence of the same area. Bottom: Calcium transients in the cells a1-c4 in response to direct electrical stimulation of a1. Time point of stimulation at 1ms/40V is indicated by the arrowhead and the perpendicular line.

Figure 5. Role of gap junctional coupling. ***A,*** Dye-coupling between astrocytes at postnatal day 16 (left) and at postnatal day 3 (right) in the *stratum radiatum*. Shown are inverted images of the Alexa fluorescence. ***B,*** Top: Transmitted light image of the *stratum radiatum* (CA1 area) at postnatal day 4. At the lower right, the stimulation pipette positioned on the cell body of an astrocyte (a1) can be seen. Cell bodies of SR101-positive astrocytes (a1-a8) analyzed in the experiment depicted below are highlighted in green. Bottom: Intracellular sodium elevations in the astrocytes a1-a8 in response to direct electrical stimulation of a1. Time point of stimulation at 1ms/40V is indicated by the arrowhead and the perpendicular line. ***C***, Cumulative 2D plot for sodium signals at P4 presented as described for Fig. 1D. ***D, E***, Mean values (± S.E.M.) of normalized amplitudes (left) and slopes (right) of sodium elevations in surrounding astrocytes, plotted as described for Fig. 1C, in P4 animals (*D*) and during application of the gap junction blocker carbenoxolone (CBX, 200μM; *E*). The

black lines represent monoexponential fits of the data, R^2 indicate the regression coefficients. Grey lines represent the monoexponential fits of the control experiments (cf. Fig. 1C).

Figure 6. Sodium propagation in wildtype C57/BL6 mice and Cx30/43 deficient mice. ***A***, Top left: Transmitted light image of the *stratum radiatum* (CA1 area) of a C57/BL6 mouse at P22. In the center, the stimulation pipette positioned on the cell body of an astrocyte (a1) can be seen. Cell bodies of SR101-positive astrocytes (a1-a5) analyzed in the experiment depicted below are highlighted in green. Bottom: Intracellular sodium elevations in the astrocytes a1-a5 in response to direct electrical stimulation of a1. Time point of stimulation at 1ms/40V is indicated by the arrowhead and the perpendicular line. ***B***, Cumulative 2D plot for sodium signals in C57/BL6 mice presented as described for Fig. 1D. ***C***, Mean values (± S.E.M.) of normalized amplitudes (left) and slopes (right) of sodium elevations in surrounding astrocytes in C57/BL6 mice, plotted as described for Fig. 1C. ***D-F***, Data for Cx30/43 deficient mice at P22-23, presented in the same way as for C57/BL6 in *A-C*. The black lines represent monoexponential fits of the data, R^2 indicate the regression coefficients. Grey lines represent the monoexponential fits of the control experiments (cf. Fig. 1C).

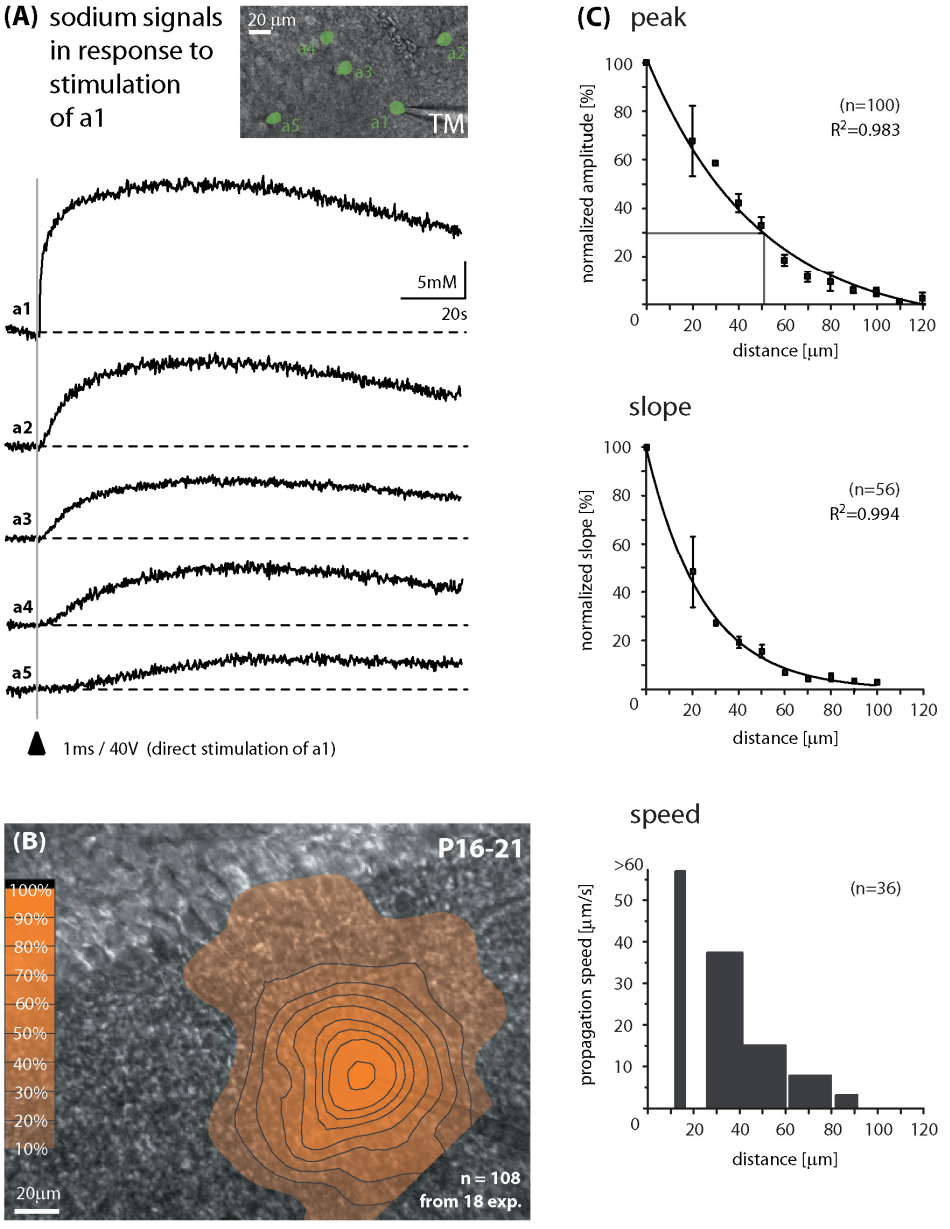

Langer et al.
Fig. 1

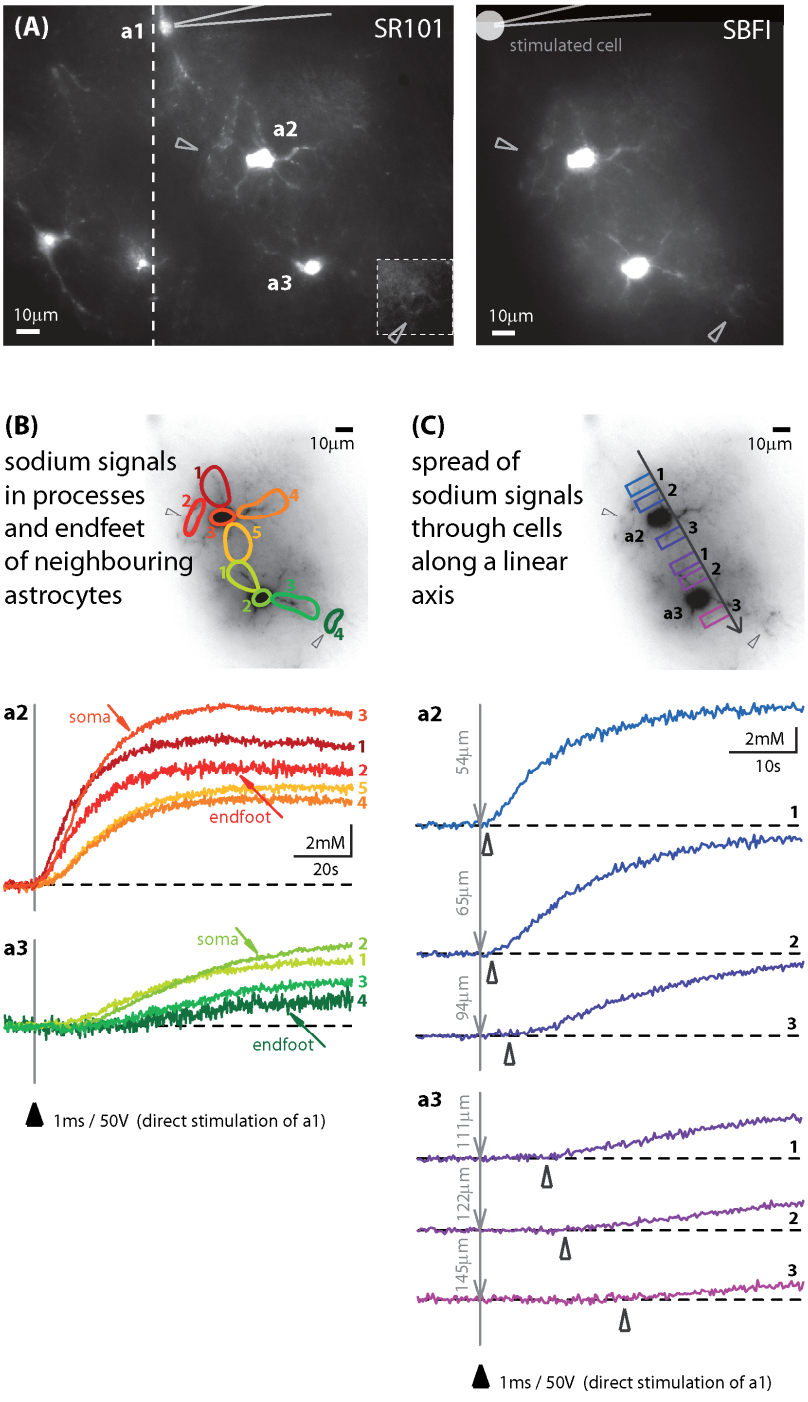

Langer et al.
Fig. 2

(A) inhibition of purinergic receptors

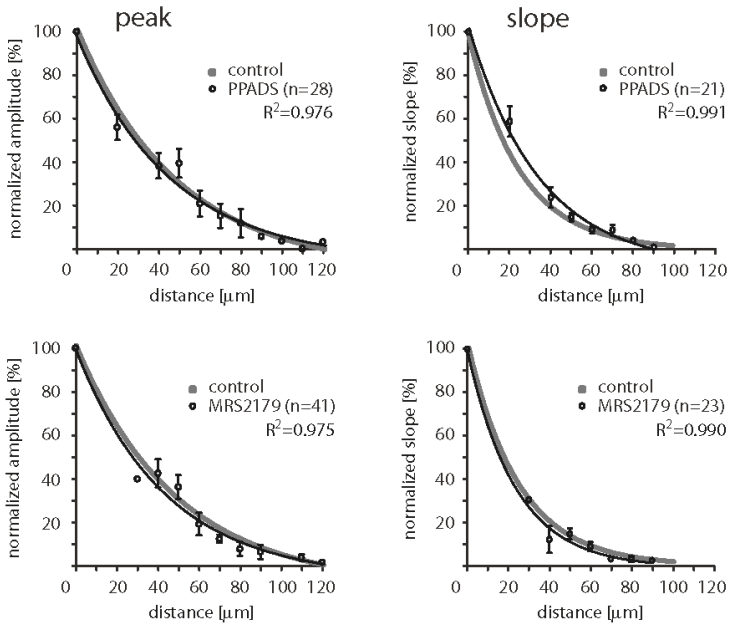

(B) inhibition of glutamate uptake

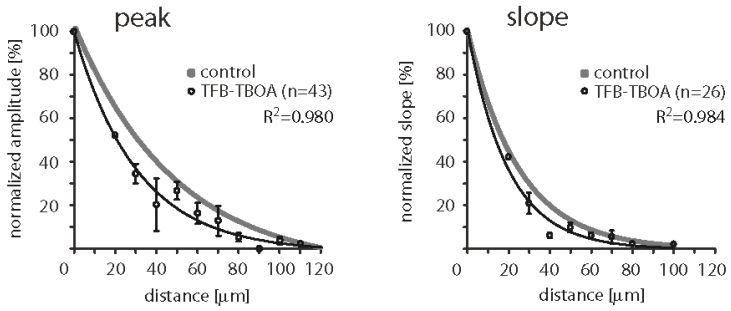

(C) inhibition of metabotropic glutamate receptors

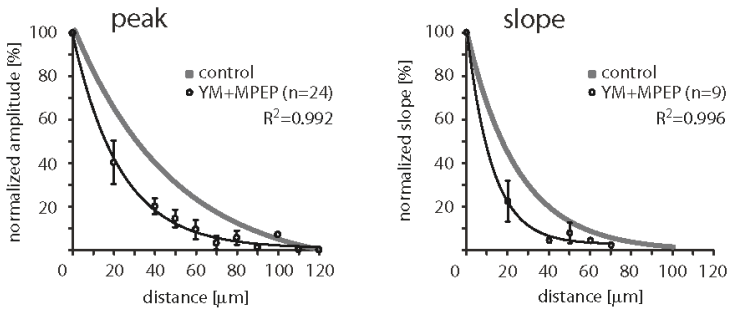

Langer et al.
Fig. 3

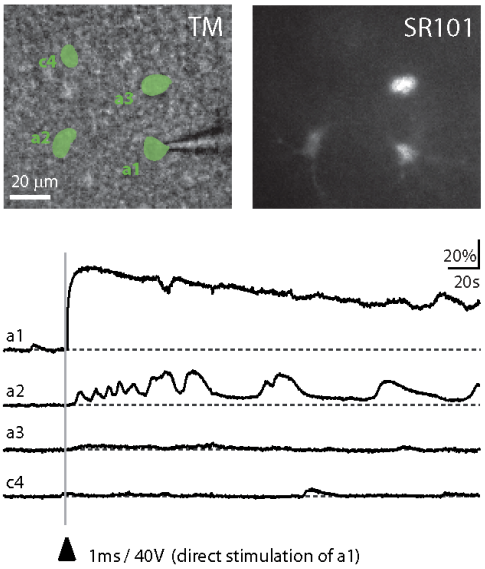

Langer et al.
Fig. 4

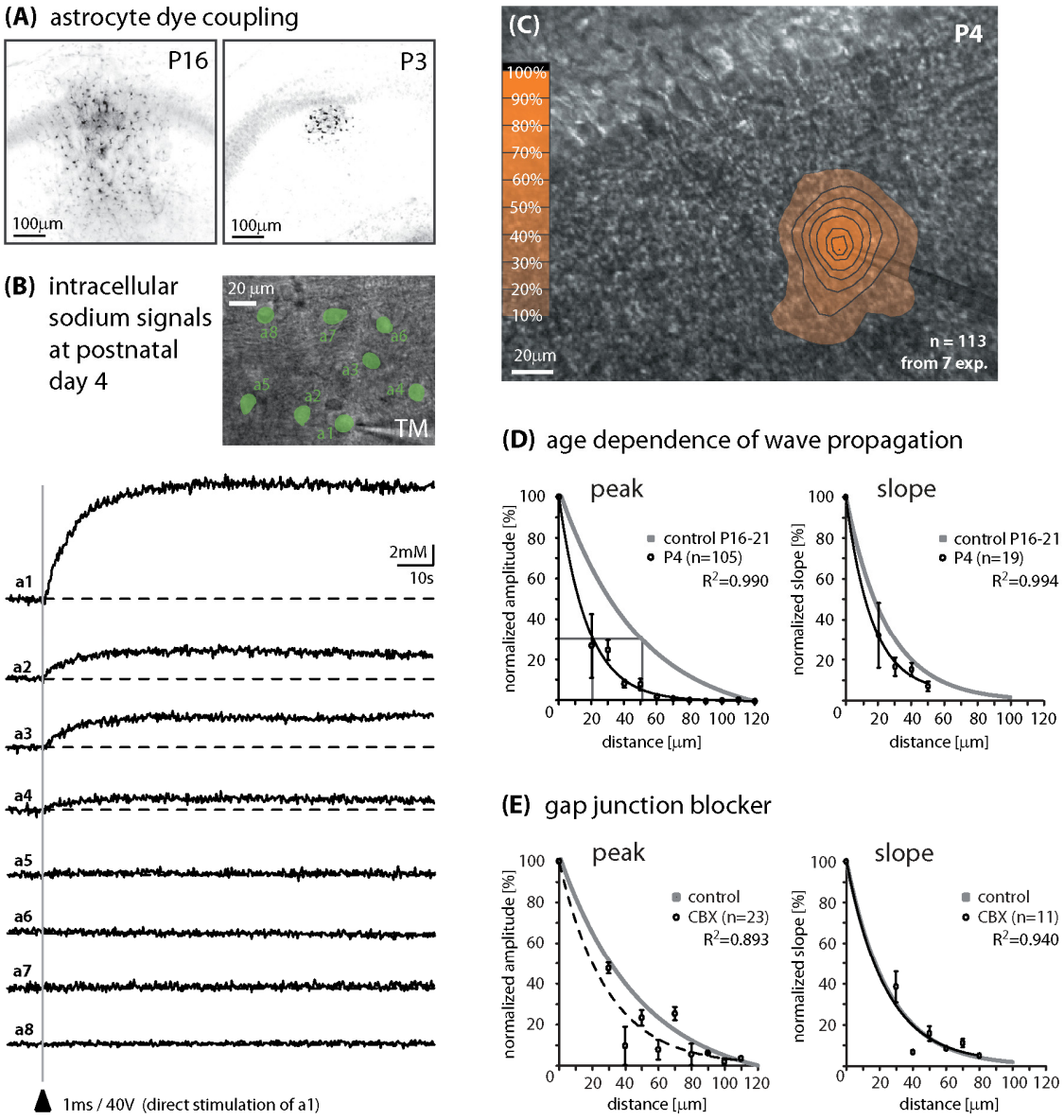

Langer et al.
Fig. 5

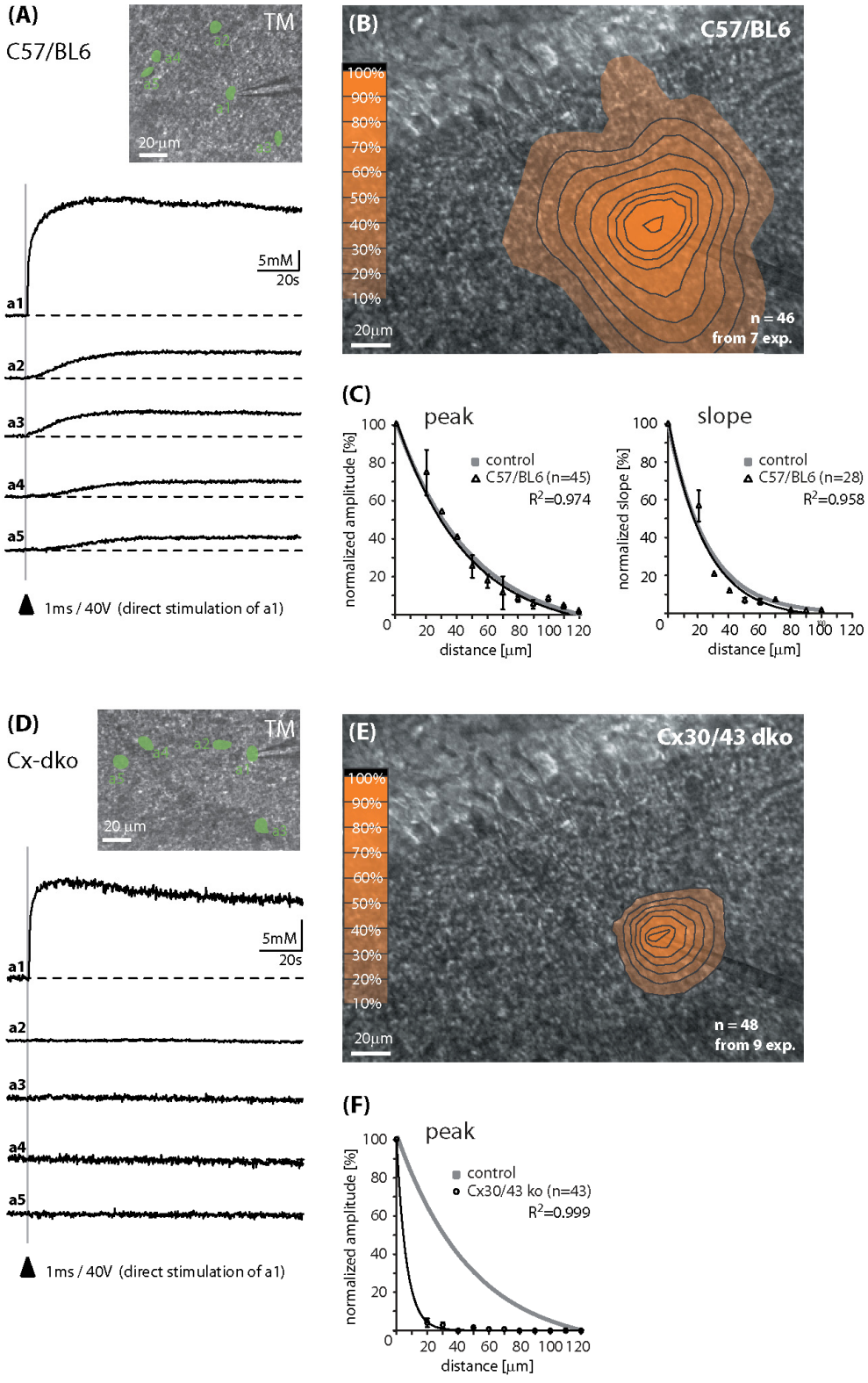

Langer et al.
Fig.6

C.3 Kafitz et al., Journal of Neuroscience Methods 169 (2008) 84-92

Developmental profile and Properties of Sulforhodamine 101-Labeled Glial Cells in Acute Brain Slices of Rat Hippocampus

Karl W. Kafitz*, Silke D. Meier*, Jonathan Stephan*, and Christine R. Rose
* These authors equally contributed to this work

My contributions:

- analysis of labeling pattern of SR101 in comparison to SBFI, together with S.D.M. (figures 1 and 2)
- majority of the whole-cell patch-clamp recordings of SR101-positive and SR101-negative cells (table 1 and figures 3 and 4)
- data analysis of all electrophysiological recordings and statistics
- immunohistochemical labeling of dye (Alexa 488) filled SR101-positive glial cells against GFAP (figure 5)
- discussion of the manuscript

ELSEVIER

Journal of Neuroscience Methods 169 (2008) 84–92

JOURNAL OF NEUROSCIENCE METHODS

www.elsevier.com/locate/jneumeth

Developmental profile and properties of sulforhodamine 101—Labeled glial cells in acute brain slices of rat hippocampus

Karl Wolfgang Kafitz [1,2], Silke Doris Meier [1,3], Jonathan Stephan [1,4], Christine Rosemarie Rose *

Institut für Neurobiologie, Heinrich-Heine-Universität Düsseldorf, Universitätsstrasse 1, D-40225 Düsseldorf, Germany

Received 30 August 2007; received in revised form 23 November 2007; accepted 26 November 2007

Abstract

The reliable identification of astrocytes for physiological measurements was always time-consuming and difficult. Recently, the fluorescent dye sulforhodamine 101 (SR101) was reported to label cortical glial cells *in vivo* [Nimmerjahn A, Kirchhoff F, Kerr JN, Helmchen F. Sulforhodamine 101 as a specific marker of astroglia in the neocortex in vivo. Nat Methods 2004;1:31–7]. We adapted this technique for use in acute rat hippocampal slices at early postnatal stages (P3, 7, 15) and in young adults (P24–27) and describe a procedure for double-labeling of SR101 and ion-selective dyes. Using whole-cell patch-clamp, imaging, and immunohistochemistry, we characterized the properties of SR101-positive versus SR101-negative cells in the *stratum radiatum*. Our data show that SR101, in contrast to Fura-2 or SBFI, only stains a subset of glial cells. Throughout development, SR101-positive and SR101-negative cells differ in their basic membrane properties. Furthermore, SR101-positive cells undergo a developmental switch from variably rectifying to passive between P3 and P15 and lack voltage-gated Na^+ currents. At P15, the majority of SR101-positive cells is positive for GFAP. Thus, our data demonstrate that SR101 selectively labels a subpopulation of glial cells in early juvenile hippocampi that shows the typical developmental changes and characteristics of classical astrocytes. Owing to its reliability and uncomplicated handling, we expect that this technique will be helpful in future investigations studying astrocytes in the developing brain.

Keywords: Astrocyte; Sulforhodamine 101; Hippocampus; Imaging; Electrophysiology; GFAP; SBFI; Fura-2

1. Introduction

During the last decade it has been firmly established that astrocytes are not purely supportive for neuronal function, but also modulate the synaptic communication between neurons (Araque et al., 1999; Fiacco et al., 2007; Haydon, 2001; Haydon and Carmignoto, 2006; Kang et al., 1998; Nedergaard, 1994; Newman and Volterra, 2004; Parri et al., 2001; Parri and Crunelli, 2007; Pascual et al., 2005; Schipke and Kettenmann, 2004; Serrano et al., 2006; Verkhratsky et al., 1998; Volterra and Meldolesi, 2005). Recent studies demonstrated that astroglia also plays a central role in the regulation of blood vessel diameter during neuronal activity (Metea and Newman, 2006; Mulligan and MacVicar, 2004; Takano et al., 2006; Zonta et al., 2003). The analysis of astrocytes in the intact tissue with electrophysiological and high-resolution imaging techniques, however, was always hampered by the problem of a reliable identification of this cell type. The identification of astrocytes based solely on morphological criteria, such as somatic size and cellular architecture, hosts the chance to mistakenly include small-sized neurons (Kimelberg, 2004). Immunohistochemical stainings of markers such as glial fibrillary acidic protein (GFAP) or the Ca^{2+}-binding protein S-100β can only be performed after the experiment, are time-consuming and often do not allow an undeniable identification of the cells analyzed in physiological experiments. To overcome this problem, transgenic mice, in which enhanced green fluorescent protein (EGFP) is expressed under the human GFAP promoter have been raised (Hirrlinger et al., 2006; Nolte et al., 2001; Zhuo et al., 1997). However, because astrocytes show very diverse levels of GFAP-expression

* Corresponding author. Tel.: +49 211 81 13416; fax: +49 211 81 13415.
E-mail addresses: kafitz@uni-duesseldorf.de (K.W. Kafitz), s.meier@uni-duesseldorf.de (S.D. Meier), jonathan.stephan@uni-duesseldorf.de (J. Stephan), rose@uni-duesseldorf.de (C.R. Rose).
[1] These authors equally contributed to this study.
[2] Tel.: +49 211 81 13486.
[3] Tel.: +49 211 81 10581.
[4] Tel.: +49 211 81 10582.

0165-0270/$ – see front matter © 2007 Elsevier B.V. All rights reserved.
doi:10.1016/j.jneumeth.2007.11.022

(Kimelberg, 2004), this approach enables the identification of only a subset of astrocytes.

Many studies reported that glial cells take up the membrane-permeable forms of Ca^{2+} indicator dyes such as Fura-2 or Fluo-4 much better than neurons (Dallwig and Deitmer, 2002; Wang et al., 2006), and astrocytes were thus often identified based on the emission patterns of the indicator dyes used. This approach was extended by Dallwig and Deitmer (2002), who have described that neurons and astrocytes in acute brain slices differ in their response to changes in the external potassium concentration. Still, this approach can only identify about 80% of astrocytes and necessitates performing additional Ca^{2+}-imaging experiments.

Recently, the fluorescent dye sulforhodamine 101 (SR101) was reported as a powerful tool for specific labeling of cortical glial cells in the intact brain of juvenile and adult rodents (Nimmerjahn et al., 2004; Wang et al., 2006). In the present study we adapted this technique for use in an acute tissue slice preparation of the rat hippocampus. Because in the CA1 region of the rodent hippocampus, astrocytes undergo considerable changes in channel complement and passive membrane properties during postnatal development (Bordey and Sontheimer, 1997; Kressin et al., 1995; Zhou et al., 2006), we performed the study at different developmental stages during the first 4 weeks after birth (postnatal days 3, 7, 15, and 24–27). Using whole-cell patch-clamp, imaging techniques, and immunohistochemistry, we show that the percentage of SR101-positive cells in the *stratum radiatum* increases during development. Furthermore, SR101-positive cells lack voltage-gated Na^+ currents and change from variably rectifying to passive cells between P3 and P15. At P15, the majority of SR101-labeled cells is positive for the astrocytic marker GFAP. Thus, our data demonstrate that SR101 selectively labels a subset of glial cells in the hippocampus that shows typical characteristics of classical astrocytes.

2. Methods

2.1. Tissue preparation and labeling with SR101

Experiments were carried out on acute tissue slices (250 μm) of rat hippocampi harvested at postnatal days 3, 7, 15, and 24–27 as described earlier (Meier et al., 2006). In brief, animals were decapitated and the hippocampi were rapidly removed. Slices of P3 and P7 animals were sectioned in ice-cold normal artificial cerebrospinal fluid (ACSF; in mM: 125 NaCl, 2.5 KCl, 2 $CaCl_2$, 1 $MgCl_2$, 1.25 NaH_2PO_4, 26 $NaHCO_3$ and 20 glucose, bubbled with 95% O_2 and 5% CO_2; pH 7.4). Following sectioning, slices were kept at 34 °C for 20 min in ACSF that contained 0.5–1 μM sulforhodamine 101 (SR101), followed by a 10 min incubation in normal ACSF at 34 °C. Preparation of slices from animals older than 15 days as well as their incubation with SR101 at high temperature was performed in ACSF with a reduced Ca^{2+} concentration (in mM: 125 NaCl, 2.5 KCl, 0.5 $CaCl_2$, 6 $MgCl_2$, 1.25 NaH_2PO_4, 26 $NaHCO_3$ and 20 glucose, bubbled with 95% O_2 and 5% CO_2; pH 7.4). Afterwards, all slices were kept at room temperature until they were used for experiments, which were also performed at room temperature. Unless stated otherwise, all chemicals were purchased from Sigma–Aldrich Co. (Taufkirchen, Germany).

2.2. Determination of the density of SR101-labeled cells

For determination of the amount of SR101-positive cells on the total number of cells exhibiting glial morphology, slices were double-labeled with SR101 and the ester form of sodium-binding benzofuran isophthalate (SBFI), a conventional Na^+-selective fluorescent dye that exhibits similar properties as Fura-2 (Meier et al., 2006). To this end, SBFI-AM (800 μM) was repeatedly (1–5 s duration each) pressure-injected through a fine-tipped glass microelectrode into the *stratum radiatum* (Stosiek et al., 2003). Injection was followed by a 45–60 min wash in normal ACSF at room temperature to allow for diffusion and de-esterification of the dye. Stacks of images (31 optical sections at 1 or 1.5 μm thickness) were then taken at a custom build two-photon laser scanning microscope (excitation wavelength at 850 nm) based on an Olympus FV300 system (Olympus Europe, Hamburg, Germany), coupled to a Mai-Tai Broadband laser (Spectra Physics, Darmstadt, Germany) and equipped with two fluorescence detection channels. Fluorescence emission of SBFI was collected between 400 and 590 nm, emission of SR101 was detected between 610 and 630 nm. Maximum intensity projections and analyses of the staining patterns were performed at montages of image stacks using "ImageJ"-software.

2.3. Electrophysiology and immunohistochemistry

Somatic whole-cell recordings were obtained at an upright microscope (Nikon Eclipse E600FN, 60× water immersion objective, N.A. 1.00, Nikon Europe, Düsseldorf, Germany) using an EPC10 amplifier (HEKA Elektronik, Lambrecht, Germany). "PatchMaster"-software (HEKA Elektronik) was used for data acquisition. Some recordings were carried out at a Zeiss Axioscope (Zeiss, Jena Germany, 40× water immersion objective, N.A. 0.80, Olympus Europe, Hamburg, Germany) using an Axopatch 200A and "PClamp 8.2"-software for data acquisition (Molecular Devices, Sunnyvale, CA). The pipette solution contained (in mM): 120 K-$MeSO_3$ or K-gluconate, 32 KCl, 10 HEPES (*N*-(2-hydroxyethyl)piperazine-*N*′-(2-ethanesulfonic acid), 4 NaCl, 4 Mg-ATP and 0.4 Na_3-GTP, 0.1 Alexafluor 488 (Molecular Probes/Invitrogen, Karlsruhe, Germany), pH 7.30. Cells were generally held at membrane potentials of −85 mV. To separate passive conductances from voltage-gated currents, online leak subtraction (P/4) was performed. Data were processed and analyzed by employing "IGOR Pro"-Software (WaveMetrics, Inc., Lake Oswego, OR).

Following electrophysiological recordings, images of fluorescence emission of SR101-labeled (excitation wavelength: 587 nm, emission detected above 602 nm) and Alexa-filled (excitation wavelength: 488 nm, emission detected between 495 and 575 nm) cells were captured by a CCD camera (Spot RT KE, Diagnostic Instruments, Inc., Sterling Hights, MI) and "Spot"-software attached to the microscope. Slices were immediately fixed over night at 4 °C in paraformaldehyde and immuno-

histochemically processed for GFAP (dilution 1:100; DAKO Z0334, Hamburg, Germany) as reported earlier (Kafitz and Greer, 1998; Kafitz et al., 1999). Labeled slices were coverslipped and documented as described above. Images of the immunohistochemistry were corrected for shrinkage caused by fixation by a factor of 1.467 and overlaid employing "Adobe Photoshop"-software.

2.4. Ca^{2+} imaging

Conventional, wide-field fluorescence imaging was performed using a variable scan digital imaging system (TILL Photonics, Martinsried, Germany) attached to an upright microscope (Axioskop, Zeiss, Jena, Germany; 40× water immersion objective, N.A. 0.80, Olympus Europe, Hamburg, Germany) and a CCD camera as a sensor (TILL Imago SVGA, TILL Photonics, Martinsried, Germany). To this end, after confirmation of successful SR101-staining (excitation wavelength: 575 nm; detection of emission: >590 nm), cells were additionally dye-loaded with the Ca^{2+}-selective dye Fura-2 (Fura-2-AM, 500 μM); employing the protocol described above for SBFI.

For wide-field imaging of Fura-2, background-corrected fluorescence signals (>410 nm) were collected from defined regions of interest after alternate excitation at 356 and 380 nm; images were acquired at 2 Hz. After background subtraction, the ratio of the fluorescence emission (F_{356}/F_{380}) was calculated using TillVision software (TILL Photonics, Martinsried, Germany) and data were analyzed off-line using "IGOR Pro"-Software (WaveMetrics, Inc., Lake Oswego, OR). Changes in calcium concentration were estimated based on an *in vitro* calibration of the Fura-2 fluorescence. ATP was applied by a Picospritzer II (General Valve/Parker Hanifin, Flein/Heilbronn, Germany) coupled to standard micropipettes (Hilgenberg, Waldkappel, Germany) placed at a distance of approximately 10–20 μm to a given cell.

2.5. Statistics

Unless otherwise specified, data are expressed as means ± S.E.M. Data were statistically analyzed by a standard *t*-test.

3. Results

3.1. Labeling pattern of acute hippocampal slices with SR101 and SR101/SBFI-AM

Incubation of cells in solutions containing 10–20 μM of the membrane-permeable acetoxymethyl ester (AM) forms of ion-selective fluorescent dyes such as the Ca^{2+}-sensitive dye Fura-2 or the Na^+-sensitive dye SBFI enables the loading and analysis of many cells at a time (e.g. Rose and Ransom, 1996, 1997). In acute brain slices, it was observed consistently that this staining protocol results in a fairly selective staining of astrocytes, and consequently, their primary identification in the intact tissue was often based on this specific staining pattern (Dallwig and Deitmer, 2002; Wang et al., 2006). Using bolus loading (injection of the AM-form of fluorescent dyes into the extracellular space) instead of bath incubation, in contrast, results in a good quality staining of neurons as well as astroglia (Meier et al., 2006; Stosiek et al., 2003). Injection of dyes thus enables the study of both astrocytes and neurons at the same time. However, dye-loaded neurons, such as interneurons with small somata in the *stratum radiatum* of the hippocampus, might be falsely identified as astrocytes based on this staining technique.

To overcome this problem, we adapted a protocol for application of the red fluorescent dye SR101, which was reported to stain astrocytes in the intact cortex of rodents (Nimmerjahn et al., 2004), for use in acute slices of the rat hippocampus. SR101 is excited around 575 nm and its emission can be collected above 590 nm, making it suitable for use in combination with many available ion-selective dyes. Initial experiments were carried out employing a post-incubation with SR101-containing ACSF at room temperature for 20 min. Independent from the SR101 concentration used (from 100 μM – as suggested by Nimmerjahn et al. (2004) for *in vivo* experiments – down to 0.5 μM), this protocol resulted in an unspecific surface label of SR101. The vast majority of the unspecific SR101 staining most likely represented a nuclear label of superficial neurons whereas cells with typical astrocytic morphology were not stained (not shown). In stark contrast to this, we found that incubation of the slices right after their preparation in ACSF containing 500 nM–1 μM SR101 for 20 min at high temperature (34 °C), resulted in a highly specific staining of cells with astrocytic morphology that was maintained for more than 8 h. The staining pattern of SR101 in slices obtained from animals at postnatal day 3 (P3, Fig. 1A), P7 (not shown), P15 (Fig. 1B), as well as P24–27 (not shown) excluded virtually all cells of the *stratum pyramidale*, clearly indicating that SR101 exclusively labeled glial cells throughout development in this preparation.

To portray cells additional to SR101-positive ones in these preparations, we performed a second labeling with the Na^+-selective fluorescent dye SBFI-AM, which (like Fura-2) is excited in the UV range. SBFI-AM was directly injected into the *stratum radiatum*, followed by a period of 45–60 min incubation in ACSF to allow for diffusion of the dye into the cells and sufficient de-esterification. At all developmental stages investigated (P3, P7, and P15), and in contrast to SR101, SBFI-AM labeled cells in the *stratum pyramidale* (presumably CA1 pyramidal neurons) as well as SR101-negative cells in the *stratum radiatum* with large somata that presumably represented interneurons or ectopic pyramidal neurons (Fig. 1A and B). SBFI-AM labeling in the *stratum radiatum* also included small-sized SR101-negative cells that morphologically resembled astrocytes as judged by the size and shape of their somata and primary processes (Fig. 1A and B). Interestingly, the percentage of SR101-positive cells on the total number of small-sized SBFI-loaded cells with glial morphology changed during postnatal development. At P15 ($n = 757$ cells in 11 slices), roughly 90% of these SBFI-stained cells were also SR101-positive, whereas at P3 ($n = 2185$ cells in 22 slices) only about 50% of them were labeled with SR101 (Fig. 2). As judged by optical inspection of SR101-incubated slices at P24–27 the vast majority of small-sized cells with glial morphology were also SR101-positive.

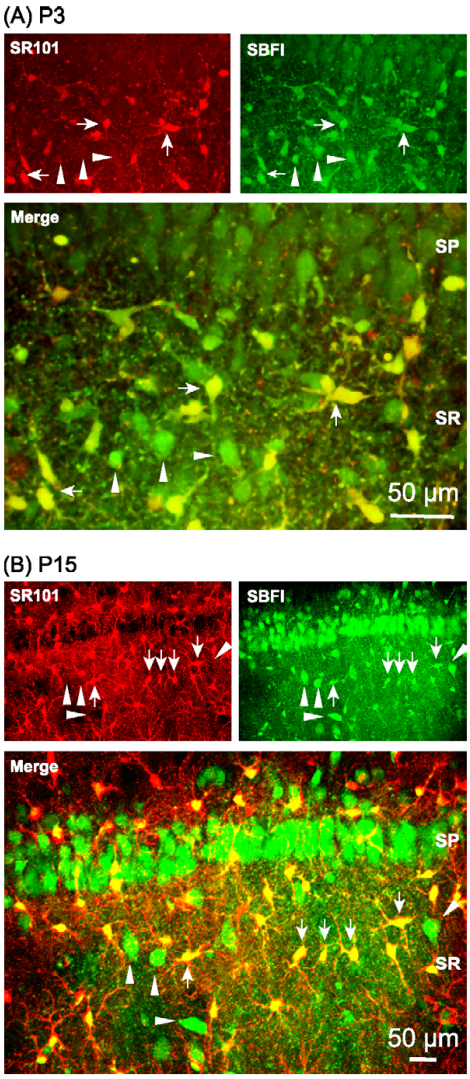

Fig. 1. Labeling pattern of SR101 vs. SBFI-AM in the hippocampal CA1 region. Fluorescence images, taken at a two-photon laser-scanning microscope, of acute slices from postnatal day P3 (A) and P15 (B) rats, double-stained with SR101 (upper left panels) and SBFI-AM (upper right panels). The lower, enlarged panels show the merged fluorescence images. SP: *stratum pyramidale*; SR: *stratum radiatum*. Arrows mark double-labeled cells located in the *stratum radiatum*; arrowheads point out cells which are exclusively stained by SBFI. Note that putative pyramidal neurons in the *stratum pyramidale* are also stained with SBFI, but not with SR101.

Taken together, these results demonstrate that SR101 stains cells with glial morphology in acute tissue slices of the rat hippocampus. Presumptive neurons are completely spared. In addition, we found a clear developmental profile of the staining pattern for SR101. Whereas the SR101-labeling comprised the vast majority of cells with glial morphology in P15 and adult

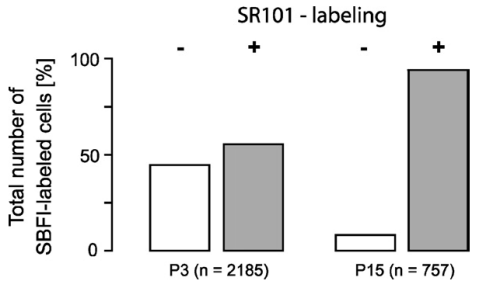

Fig. 2. Quantification of the percentage of SR101-negative (white bars) and SR101-postive (grey bars) cells on the total number of small-sized SBFI-labeled cells located in the *stratum radiatum* in P3 ($n = 22$ slices; 2185 cells) and P15 rats ($n = 11$ slices; 757 cells).

animals, only about half of such cells were stained by SR101 at P3.

3.2. *Electrophysiological characterization of SR101-positive and SR101-negative cells*

In the CA1 region of the rodent hippocampus, several types of astrocytes were described based on their electrophysiological properties (Bordey and Sontheimer, 2000; D'Ambrosio et al., 1998; Kressin et al., 1995; Steinhauser et al., 1994b; Zhou and Kimelberg, 2001). Moreover, astrocytes undergo considerable changes in channel complement and passive membrane properties during early postnatal development (Bordey and Sontheimer, 1997; Kressin et al., 1995; Zhou et al., 2006). Therefore, we characterized the electrophysiological properties of SR101-positive and SR101-negative cells with glial morphology in the *stratum radiatum* by performing patch-clamp experiments in the whole-cell configuration. Current injection in the current-clamp mode failed to elicit action potentials in any of the cells investigated ($n = 126$; not shown) indicating that they were indeed glia or glial precursor cells, respectively.

Throughout development, SR101-positive and SR101-negative cells differed significantly in their membrane properties. At early stages, SR101-negative cells ($n = 13$ at P3, $n = 5$ at P15) generally had more depolarized membrane potentials, their membrane resistance was higher and their membrane capacity was lower than that of SR101-positive cells (Table 1). We found no differences in these properties between P3 and P15 animals in SR101-negative cells. At P24–27, SR101-negative cells showed a tendency to be more hyperpolarized and had a higher membrane resistance and capacity compared to younger stages (Table 1). SR101-positive cells also showed developmental changes in their electrophysiological properties. Whereas the membrane potential of SR101-positive cells was highly negative at all four stages investigated (−80 to −87 mV; Table 1), their membrane resistance decreased from 94 MΩ at P3 ($n = 42$), to 68 MΩ at P7 ($n = 6$), and to 6 and 11 MΩ (P15, $n = 37$; P24–27, $n = 13$). At the same time, membrane capacity increased (from 69 to 880 pF; Table 1).

To reveal the functional expression of voltage-gated ion channels, cells were held in the voltage-clamp mode at −85 mV

Table 1
Membrane properties of SR101-positive and SR101-negative cells at P3, P7, P15 and in young adults (P24–27)

SR101 labeling	Age [pnd]	Membrane potential [mV]	Membrane resistance [MΩ]	Membrane capacity [pF]	n
SR-	P3	-67 ± 17	353 ± 325	30 ± 30	13
	P15	-77 ± 14	302 ± 202	27 ± 18	5
	P24-27	-81 ± 5	168 ± 153	95 ± 89	6
**					
SR+	P3	-83 ± 6	94 ± 52	69 ± 48	42
	P7	-80 ± 4	68 ± 32	120 ± 72	6
	P15	-87 ± 3	6 ± 5	139 ± 91	37
	P24-27	-85 ± 4	11 ± 10	880 ± 1274	13

Significance level: $^{**}\alpha = 0.01$.

and then subjected to a rectangular voltage step protocol (from −150 to +50 mV, 10 mV increments). The voltage-step protocol induced large capacitive as well as passive currents (Fig. 3A–C; insets). Leak subtraction (P/4) was performed to reveal voltage-gated currents activated by membrane depolarization (Fig. 3A–C; insets; see also Fig. 4). The amplitudes of the currents were measured at 8–10 ms after the start of the voltage step, and current was plotted versus voltage (*I/V*-relationship, Fig. 3A–C). Data were fit by a linear regression curve; the threshold for linearity of the *I/V* relation was set at a regression coefficient of $r^2 = 0.9983$.

At P3, both SR101-positive ($n = 42$) and SR101-negative ($n = 13$) cells exhibited voltage-activated outward currents and only non-linear *I/V* relationships with a variable degree of outward rectification were found ("non-passive cells", nPC; Figs. 3A, D and 4A, B). In SR101-positive cells, outward-currents were non-inactivating (Fig. 3A), while in SR101-negative cells, the amplitude of outward currents decreased over time (Fig. 4A). At P7, SR101-positive cells exhibited non-linear *I/V* relationships with non-inactivating outward currents as well ($n = 6$; Fig. 3B and D), whereas the majority (78%) of SR101-positive cells at P15 ($n = 38$) and all SR101-positive cells at P24–27 ($n = 13$) lacked voltage-gated currents and thus showed a linear *I/V* relationship ("passive cells", PC; Figs. 3C, D and 4D). SR101-negative cells at P15 ($n = 5$) as well as at P24–27 ($n = 6$), in contrast, exclusively showed non-linear properties (Fig. 4C).

To further characterize SR101-positive and negative cells, we examined which phenotype functionally expressed voltage-gated fast inward currents. To relieve inactivation of voltage-gated Na^+ channels, the voltage step protocol was extended by a hyperpolarizing preconditioning pulse to −120 mV. SR101-positive cells completely lacked fast inward currents at P3 ($n = 42$; Fig. 4B), at P15 ($n = 37$; Fig. 4D) as well as at P24–27 ($n = 13$). In contrast, 4 out of 13 SR101-negative cells at P3 (Fig. 4A) and all SR101-negative cells at P15 ($n = 5$) and at P24–27 ($n = 6$) expressed voltage-gated fast inward currents.

Taken together, these results demonstrate that small-sized, SBFI-stained cells in the *stratum radiatum* represent glial cells that can be divided into two subtypes differing in their staining pattern with SR101 as well as in their passive and active membrane properties. At P15 and in young adults, the vast majority of SR101-positive cells show the typical electrophysiological properties of classical passive astrocytes (Bordey and Sontheimer, 2000; D'Ambrosio et al., 1998; Steinhauser et al., 1992; Zhou et al., 2006).

3.3. Immunohistochemical characterization of SR101-positive cells

To further establish the astrocytic identity of SR101-positive glial cells at P15, we immunohistochemically stained for GFAP. To this end, SR101-positive cells were first characterized electrophysiologically and in parallel filled with the fluorescent dye Alexa 488 via the patch pipette to enable their identification in the slices processed for immunohistochemistry. As described above, we found that all SR101-positive cells at P15 exhibited electrophysiological properties of classical astrocytes ($n = 26$). The majority of these cells ($n = 23/26$ cells) were also GFAP-positive, confirming their astrocytic identity (Fig. 5A). Three of 26 investigated SR101-positive cells were GFAP-negative (Fig. 5B), indicating that GFAP only labels a subset of astroglial cells as reported earlier (Lee et al., 2006; Raponi et al., 2007).

3.4. ATP-induced Ca^{2+} transients in SR101-stained slices

To validate the described double-staining protocol of SR101 and ion-selective dyes for physiological measurements, we performed dynamic fluorescence imaging in acute hippocampal slices at P15, employing the Ca^{2+}-sensitive dye Fura-2-AM (Fig. 6). We tested the responses of the cells to a focal pressure application of ATP (10 μM for 100 ms) through a fine micropipette, which has been shown to induce intracellular Ca^{2+} transients in glial cells (Verkhratsky et al., 1998). Focal applica-

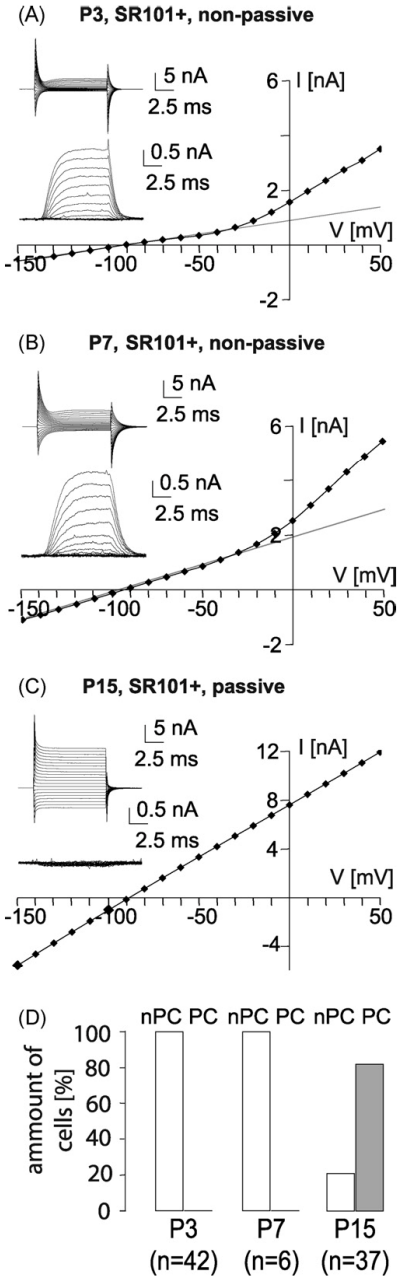

Fig. 3. *I/V* relationship of SR101-positive cells of P3 (A), P7 (B) and P15 (C) rats. Cells were held at −85 mV and subjected to 10 ms voltage steps ranging from −150 to +50 mV at 10 mV increments. The insets on the left side show the resulting membrane currents before (top) and after leak subtraction (bottom). The *I/V* plots depict the amplitudes of the resulting currents at 8–10 ms after the start of the voltage step of the same cells, the grey lines show the linear regression curves. Animals at P3 (A) and P7 (B) exclusively showed non-linear *I/V* relationships, in P15 animals (C), mostly linear *I/V* curves were found. (D) Quantification of the amount of cells with non-linear (non-passive cells, nPCs, white bars) or linear (passive cells, PCs, grey bars) *I/V* curves on the total number of SR101-positive cells at P3, P7 and P15.

tion of ATP resulted in a transient elevation of the intracellular Ca^{2+} concentration in 15 out of 18 SR101-positive (83%), as well as in 5 out of 7 SR101-negative cells (71%) within the field of view ($n = 6$ experiments in 6 slices; Fig. 6). The amplitude of ATP-induced calcium transients was dependent on the distance of the cells from the tip of the application pipette, the orientation of perfusion flow, and the depth of the cell in the slice. When analyzing cells located within a circular area with a radius of 50 μm from the tip of the application pipette, the amplitude of the calcium transients was not significantly different between SR101-positive and SR101-negative cells and averaged about 20 nM. In summary, these measurements confirm that SR101 labeling of acute slices does not interfere with intracellular ion measurements using ion-selective fluorescent dyes (Jourdain et al., 2007; Nimmerjahn et al., 2004).

4. Discussion

In the present study, we describe a procedure for double-labeling of acute slice preparations of the rat hippocampus with the fluorescent dye SR101 and AM-esters of ion-selective fluorescent dyes. SR101 was introduced recently to selectively identify astrocytes in the neocortex of 2–4-week-old rats (Nimmerjahn et al., 2004). It is a red fluorescent dye that can be combined with fluorescent dyes excited in the UV range such as Fura-2 or SBFI (this study) or excited at 400–500 nm such as Oregon Green (Nimmerjahn et al., 2004) and Alexa 488 (this study, Nimmerjahn et al., 2004). In accordance with the latter study, we did not find any evidence for a distortion of induced intracellular Ca^{2+} transients in cells that were stained with both, SR101 and the ion-selective fluorescent dye.

Astrocytes *in situ* are heterogeneous with respect to their physiological properties (D'Ambrosio et al., 1998; Grass et al., 2004; Matthias et al., 2003; Steinhauser et al., 1992, 1994b; Zhou and Kimelberg, 2000, 2001) and undergo considerable changes in channel complement and passive membrane properties during early postnatal development (Bordey and Sontheimer, 1997; Kressin et al., 1995; Zhou et al., 2006). Thus, using whole-cell patch-clamp, imaging techniques and immunohistochemistry, we characterized the properties of SR101-positive versus SR101-negative cells in the *stratum radiatum* at postnatal days 3, 7, 15 and 24–27.

Based on their electrophysiological properties, two basic types of astrocytes have been described in the hippocampus (Bordey and Sontheimer, 2000; D'Ambrosio et al., 1998; Kressin et al., 1995; Steinhauser et al., 1994b; Zhou and Kimelberg, 2001). One cell type, termed "outwardly rectifying" (Zhou and Kimelberg, 2000, 2001) or "complex" (Kressin et al., 1995; Steinhauser et al., 1994b) is mainly characterized by a membrane potential which is significantly more positive than the equilibrium potential for K^+, by a high input resistance, and by a low membrane capacity. Moreover, this cell type functionally

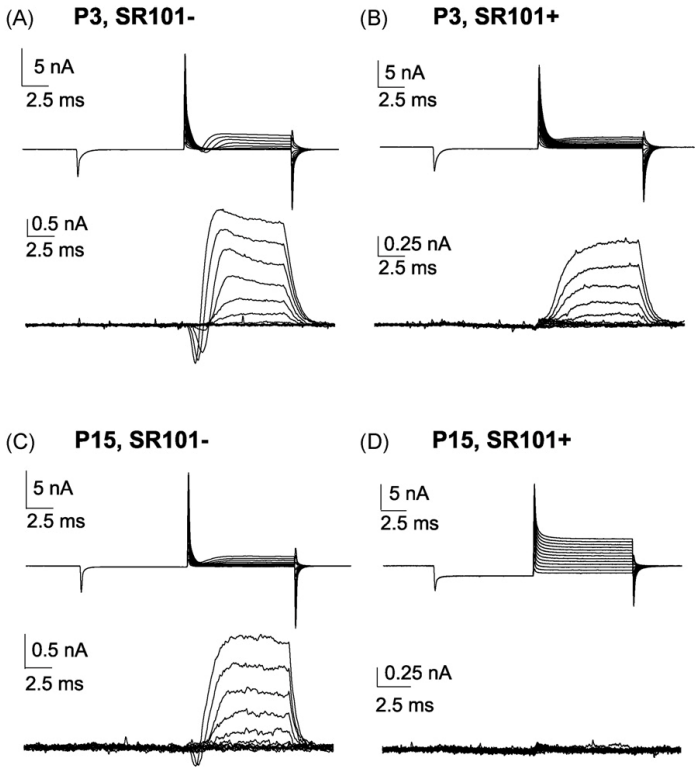

Fig. 4. Expression pattern of voltage-gated fast inward currents at P3 (A, B) and P15 (C, D). To relieve inactivation of voltage-gated Na^+ channels, cells were held at −85 mV and subjected to a prepulse to −120 mV for 10 ms before stepping from −110 to +10 mV in increments of 10 mV. Shown are the resulting currents before (upper traces) and after (lower traces) leak subtraction. At both ages, fast voltage-gated inward currents were only observed in SR101-negative (A, C), but not in SR101-positive (B, D) cells.

expresses two types of K^+-outward currents, a delayed rectifier and a transient A-type current, as well as TTX-sensitive Na^+ channels. The hallmarks of the second type of astrocytes are a highly negative membrane potential, a low input resistance, and a high membrane capacity. Furthermore, these cells lack voltage-gated Na^+ currents and show a largely symmetrical expression of inward and outward K^+ currents that consist predominantly of ohmic currents with small contributions of delayed rectifier K^+ currents. Accordingly, this cell type was called "passive" (Kressin et al., 1995; Steinhauser et al., 1994a) or "variably rectifying" (Zhou and Kimelberg, 2000, 2001) astrocyte. In addition, both astrocyte types differ in their expression profile for ionotropic glutamate receptors and glutamate transporters. Whereas the first type expresses ionotropic glutamate receptors and lacks glutamate transporter currents (Matthias et al., 2003; Zhou and Kimelberg, 2001), the second type lacks ionotropic glutamate receptors, but shows significant glutamate uptake currents (Matthias et al., 2003; Zhou and Kimelberg, 2001). Based on these differences, the second type ("passive" or "variably rectifying" astrocyte) is often regarded as the "classical" astrocyte, as it is capable to perform classical functions of astrocytes, such as the uptake of glutamate and potassium from the extracellular space (Matthias et al., 2003; Zhou and Kimelberg, 2001).

Our results show that SR101-positive cells during the first 4 weeks of postnatal development display the electrophysiological properties typical for immature and mature classical astrocytes described above. The developmental profile of current expression of SR101-positive cells is in good agreement with earlier studies showing that the amount of outward rectification in such cells decreases with age (Steinhauser et al., 1992; Wallraff et al., 2004; Zhou et al., 2006). The electrophysiological properties of SR101-negative cells, in contrast, are reminiscent of the first type of astrocytes described above, but may also include a population of glial cells positive for the chondroitin sulfate proteoglycan NG2 and thus, may partly represent glial progenitor cells (Matthias et al., 2003; Zhou et al., 2006).

Taken together, our data demonstrate for the first time that SR101, in contrast to conventional fluorescent ion-selective dyes such as Fura-2 or SBFI, selectively labels a subpopulation of glial cells in the early postnatal hippocampus that shows the typical developmental changes and characteristics of classical astrocytes. Staining with SR101 enables a direct and reliable identification of virtually all such astrocytes in acute brain slices

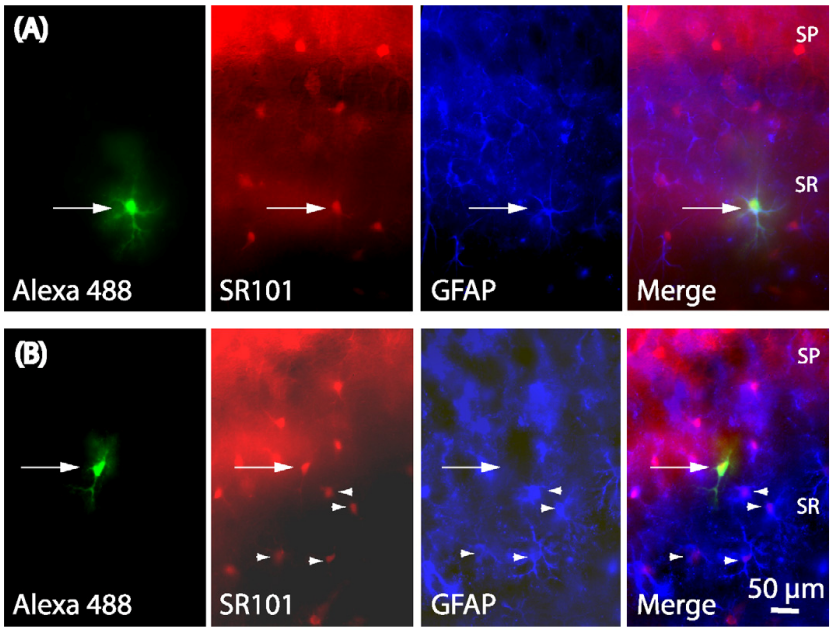

Fig. 5. Immunohistochemical characterization of SR101-positive cells at P15. (A) From left to right: image of the staining pattern of SR101 in the *stratum radiatum*. Based on this staining, a SR101-positive cell was chosen (arrow) and characterized electrophysiologically while filling the cell with Alexa 488. In the subsequent immunohistochemical analysis, the same cell also showed immunoreactivity for GFAP. The merged picture of all three fluorescence images confirms the identity of the triple-labeled cell. (B) The same experimental design also identified a cell which was SR101-positive, electrophysiologically characterized as glial cell, but showed no immunoreactivity for GFAP (arrow). The arrowheads point to cells, which were double-labeled for SR101 and GFAP. SP: *stratum pyramidale*; SR: *stratum radiatum*.

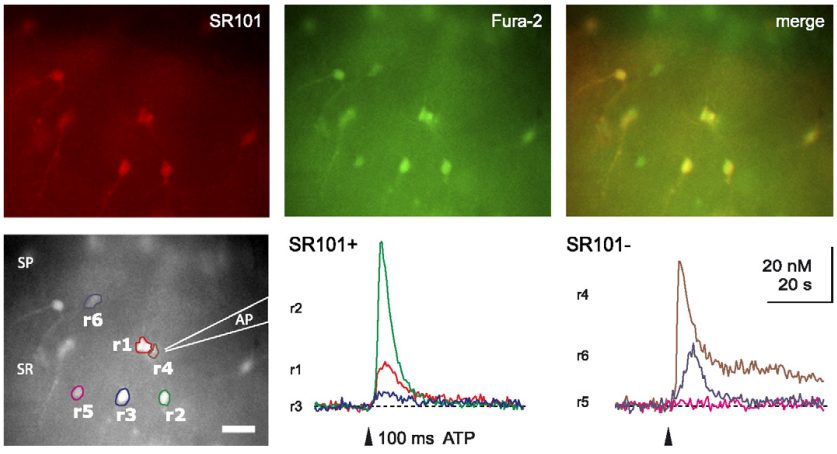

Fig. 6. ATP-induced Ca^{2+} transients in SR101-positive and SR101-negative cells at P15. Top, left: image of the staining pattern of SR101 in the *stratum radiatum*. Top, center and right: staining pattern of the Ca^{2+}-sensitive dye Fura-2 and merged image. Bottom, left: image of the Fura-2 fluorescence. The colored lines indicate the regions of interest (r1–r6) in which the Ca^{2+}-measurements were performed. The position of the application pipette (AP) is indicated schematically on the right. Bottom, right: focal pressure application of 10 µM ATP for 100 ms induced Ca^{2+} transients in both SR101-positive (left) and SR101-negative (right) cells. The experiment was performed using a widefield imaging system.

for physiological measurements as well as immunohistochemical studies. Owing to its reliability and uncomplicated handling, we expect that this technique will be helpful in future investigations studying the functions of astrocytes and neuron-glia interaction in the developing brain.

Acknowledgements

We thank Simone Durry and Claudia Roderigo for expert technical assistance. This study was supported by the DFG.

References

Araque A, Parpura V, Sanzgiri RP, Haydon PG. Tripartite synapses: glia, the unacknowledged partner. Trends Neurosci 1999;22:208–15.

Bordey A, Sontheimer H. Postnatal development of ionic currents in rat hippocampal astrocytes in situ. J Neurophysiol 1997;78:461–77.

Bordey A, Sontheimer H. Ion channel expression by astrocytes in situ: comparison of different CNS regions. Glia 2000;30:27–38.

Dallwig R, Deitmer JW. Cell-type specific calcium responses in acute rat hippocampal slices. J Neurosci Methods 2002;116:77–87.

D'Ambrosio R, Wenzel J, Schwartzkroin PA, McKhann II GM, Janigro D. Functional specialization and topographic segregation of hippocampal astrocytes. J Neurosci 1998;18:4425–38.

Fiacco TA, Agulhon C, Taves SR, Petravicz J, Casper KB, Dong X, et al. Selective stimulation of astrocyte calcium in situ does not affect neuronal excitatory synaptic activity. Neuron 2007;54:611–26.

Grass D, Pawlowski PG, Hirrlinger J, Papadopoulos N, Richter DW, Kirchhoff F, et al. Diversity of functional astroglial properties in the respiratory network. J Neurosci 2004;24:1358–65.

Haydon P. Glia: listening and talking to the synapse. Nat Neurosci Rev 2001;2:185–93.

Haydon PG, Carmignoto G. Astrocyte control of synaptic transmission and neurovascular coupling. Physiol Rev 2006;86:1009–31.

Hirrlinger PG, Scheller A, Braun C, Hirrlinger J, Kirchhoff F. Temporal control of gene recombination in astrocytes by transgenic expression of the tamoxifen-inducible DNA recombinase variant CreERT2. Glia 2006;54:11–20.

Jourdain P, Bergersen LH, Bhaukaurally K, Bezzi P, Santello M, Domercq M, et al. Glutamate exocytosis from astrocytes controls synaptic strength. Nat Neurosci 2007;10:331–9.

Kafitz KW, Greer CA. Differential expression of extracellular matrix and cell adhesion molecules in the olfactory nerve and glomerular layers of adult rats. J Neurobiol 1998;34:271–82 [published erratum appears in J Neurobiol 1998 Apr;35(1):118].

Kafitz KW, Guttinger HR, Muller CM. Seasonal changes in astrocytes parallel neuronal plasticity in the song control area HVc of the canary. Glia 1999;27:88–100.

Kang J, Jiang L, Goldman S, Nedergaard M. Astrocyte-mediated potentiation of inhibitory synaptic transmission. Nat Neurosci 1998;1:683–92.

Kimelberg HK. The problem of astrocyte identity. Neurochem Int 2004;45:191–202.

Kressin K, Kuprijanova E, Jabs R, Seifert G, Steinhauser C. Developmental regulation of Na+ and K+ conductances in glial cells of mouse hippocampal brain slices. Glia 1995;15:173–87.

Lee Y, Su M, Messing A, Brenner M. Astrocyte heterogeneity revealed by expression of a GFAP-LacZ transgene. Glia 2006;53:677–87.

Matthias K, Kirchhoff F, Seifert G, Huttmann K, Matyash M, Kettenmann H, et al. Segregated expression of AMPA-type glutamate receptors and glutamate transporters defines distinct astrocyte populations in the mouse hippocampus. J Neurosci 2003;23:1750–8.

Meier SD, Kovalchuk Y, Rose CR. Properties of the new fluorescent Na+ indicator CoroNa Green: comparison with SBFI and confocal Na+ imaging. J Neurosci Methods 2006;155:251–9.

Metea MR, Newman EA. Glial cells dilate and constrict blood vessels: a mechanism of neurovascular coupling. J Neurosci 2006;26:2862–70.

Mulligan SJ, MacVicar BA. Calcium transients in astrocyte endfeet cause cerebrovascular constrictions. Nature 2004;431:195–9.

Nedergaard M. Direct signaling from astrocytes to neurons in cultures of mammalian brain cells. Science 1994;263:1768–71.

Newman EA, Volterra A. Glial control of synaptic function. Glia 2004;47:207–8.

Nimmerjahn A, Kirchhoff F, Kerr JN, Helmchen F. Sulforhodamine 101 as a specific marker of astroglia in the neocortex in vivo. Nat Methods 2004;1:31–7.

Nolte C, Matyash M, Pivneva T, Schipke CG, Ohlemeyer C, Hanisch UK, et al. GFAP promoter-controlled EGFP-expressing transgenic mice: a tool to visualize astrocytes and astrogliosis in living brain tissue. Glia 2001;33:72–86.

Parri HR, Gould TM, Crunelli V. Spontaneous astrocytic Ca2+ oscillations in situ drive NMDAR-mediated neuronal excitation. Nat Neurosci 2001;4:803–12.

Parri R, Crunelli V. Astrocytes target presynaptic NMDA receptors to give synapses a boost. Nat Neurosci 2007;10:271–3.

Pascual O, Casper KB, Kubera C, Zhang J, Revilla-Sanchez R, Sul JY, et al. Astrocytic purinergic signaling coordinates synaptic networks. Science 2005;310:113–6.

Raponi E, Agenes F, Delphin C, Assard N, Baudier J, Legraverend C, et al. S100B expression defines a state in which GFAP-expressing cells lose their neural stem cell potential and acquire a more mature developmental stage. Glia 2007;55:165–77.

Rose CR, Ransom BR. Intracellular Na^+ homeostasis in cultured rat hippocampal astrocytes. J Physiol 1996;491:291–305.

Rose CR, Ransom BR. Gap junctions equalize intracellular Na^+ concentration in astrocytes. Glia 1997;20:299–307.

Schipke CG, Kettenmann H. Astrocyte responses to neuronal activity. Glia 2004;47:226–32.

Serrano A, Haddjeri N, Lacaille JC, Robitaille R. GABAergic network activation of glial cells underlies hippocampal heterosynaptic depression. J Neurosci 2006;26:5370–82.

Steinhauser C, Berger T, Frotscher M, Kettenmann H. Heterogeneity in the membrane current pattern of identified glial cells in the hippocampal slice. Eur J Neurosci 1992;4:472–84.

Steinhauser C, Jabs R, Kettenmann H. Properties of GABA and glutamate responses in identified glial cells of the mouse hippocampal slice. Hippocampus 1994a;4:19–35.

Steinhauser C, Kressin K, Kuprijanova E, Weber M, Seifert G. Properties of voltage-activated Na+ and K+ currents in mouse hippocampal glial cells in situ and after acute isolation from tissue slices. Pflugers Arch 1994b;428:610–20.

Stosiek C, Garaschuk O, Holthoff K, Konnerth A. In vivo two-photon calcium imaging of neuronal networks. Proc Natl Acad Sci USA 2003;100:7319–24.

Takano T, Tian GF, Peng W, Lou N, Libionka W, Han X, et al. Astrocyte-mediated control of cerebral blood flow. Nat Neurosci 2006;9:260–7.

Verkhratsky A, Orkand RK, Kettenmann H. Glial calcium: homeostasis and signaling function. Physiol Rev 1998;78:99–141.

Volterra A, Meldolesi J. Astrocytes, from brain glue to communication elements: the revolution continues. Nat Rev Neurosci 2005;6:626–40.

Wallraff A, Odermatt B, Willecke K, Steinhauser C. Distinct types of astroglial cells in the hippocampus differ in gap junction coupling. Glia 2004;48:36–43.

Wang X, Lou N, Xu Q, Tian GF, Peng WG, Han X, et al. Astrocytic Ca(2+) signaling evoked by sensory stimulation in vivo. Nat Neurosci 2006;9:816–23.

Zhou M, Kimelberg HK. Freshly isolated astrocytes from rat hippocampus show two distinct current patterns and different [K(+)](o) uptake capabilities. J Neurophysiol 2000;84:2746–57.

Zhou M, Kimelberg HK. Freshly isolated hippocampal CA1 astrocytes comprise two populations differing in glutamate transporter and AMPA receptor expression. J Neurosci 2001;21:7901–8.

Zhou M, Schools GP, Kimelberg HK. Development of GLAST(+) astrocytes and NG2(+) glia in rat hippocampus CA1: mature astrocytes are electrophysiologically passive. J Neurophysiol 2006;95:134–43.

Zhuo L, Sun B, Zhang CL, Fine A, Chiu SY, Messing A. Live astrocytes visualized by green fluorescent protein in transgenic mice. Dev Biol 1997;187:36–42.

Zonta M, Angulo MC, Gobbo S, Rosengarten B, Hossmann KA, Pozzan T, et al. Neuron-to-astrocyte signaling is central to the dynamic control of brain microcirculation. Nat Neurosci 2003;6:43–50.

D Acknowledgement

In the daily turn one easily forgets to say “thank you” for all the small and big things. This I want to catch up now.

First of all I want to thank Prof. Dr. Christine R. Rose for the possibility to write my doctoral thesis in her lab and for her endurance and support during all the different and sometimes difficult stages of my thesis. Next I want to thank Prof. Dr. Dieter Willbold for the examination of this work and that in a very short time so that I can quickly proceed with the defense of my thesis. And of course I have to thank the DFG for funding the project.

I also want to thank PD Dr. Gerald Seifert and Prof. Dr. Christian Steinhäuser for the delivery of KO mice and Dr. Daniel Eberhard and Prof. Dr. Eckhart Lammert for the possibility to temporarily the mice in the animal room of their institute.

I have to thank the HE club, especially Nicolle and Daniel, whose data from their diploma theses contributed to my work. And I want to thank Simone for her practical support, doing the immunohistochemistry, and Karl and Alexandra for the help with the confocal documentation.

And I want to thank Karl and Peter for their critical comments and advise on my thesis.

I thank the whole institute for neurobiology for being such a kind and helpful group. I have to address special thanks to Christian for all the stuff beside daily work and of course Julia for all the discussions around our theses.

Finally I want to thank my family for their unconditioned support, especially Jessica for her endurance during the very last stage of writing when I was physically at home, but mental still at work.

E Declaration

Die hier vorgelegte Dissertation habe ich eigenständig und ohne unerlaubte Hilfe angefertigt. Die Dissertation wurde in der vorgelegten oder in ähnlicher Form noch bei keiner anderen Institution eingereicht. Ich habe keine erfolglosen Promotionsversuche unternommen.

Düsseldorf, den 14.03.2011

(Jonathan Stephan)